La Rivista del Nuovo Cimento
https://doi.org/10.1007/s40766-024-00054-z

Advances in cavity-enhanced methods for high precision molecular spectroscopy and test of fundamental physics

L. Gianfrani[1] · **S.-M. Hu**[2] · **W. Ubachs**[3]

Abstract

Cavity-enhanced spectroscopic techniques are highly sensitive laser-based methods for interrogating the atomic and molecular constituents of any gaseous medium that is confined into an optical resonator. A first advantage over conventional absorption spectroscopy comes from the extremely long path length of the laser radiation inside the stable, high-finesse, optical cavity, which allows the sample to be probed over several tens of kilometers. After more than 30 years of research and development, techniques like cavity ring-down spectroscopy, cavity-enhanced absorption spectroscopy, and noise-immune cavity-enhanced optical-heterodyne molecular spectroscopy, have reached extraordinary levels of detection sensitivity, such that it is possible to measure light absorption from molecules in trace amounts or extremely weak spectral lines of more abundant species. A second advantage of the use of high-finesse cavities lies in the power amplification achieved inside the optical resonator, making it possible to saturate even weak transitions, thus reducing the width of spectral lines by some three orders of magnitude. Combining these methods with frequency comb technologies has further enhanced their capabilities, adding metrology-grade qualities to spectroscopic determinations such as transition frequencies of molecular resonances, which can be measured with sub-kHz accuracy. In this review article, we discuss the current status of highly precise and highly sensitive laser spectroscopy for fundamental tests and measurements. We describe state-of-the-art molecular spectroscopy methods and their

---

✉ L. Gianfrani
livio.gianfrani@unicampania.it

S.-M. Hu
smhu@ustc.edu.cn

W. Ubachs
w.m.g.ubachs@vu.nl

[1] Department of Mathematics and Physics, Università degli studi della Campania “Luigi Vanvitelli”, Viale A. Lincoln 5, 81100 Caserta, Italy

[2] State Key Laboratory of Molecular Reaction Dynamics, Department of Chemical Physics, University of Science and Technology of China, Hefei 230026, China

[3] Department of Physics and Astronomy, LaserLaB, Vrije Universiteit, De Boelelaan 1081, 1081 HV Amsterdam, The Netherlands

application to a few selected molecules of fundamental importance in understanding quantum chemistry theories or testing quantum electrodynamics.

Keywords Cavity ring-down spectroscopy · Cavity-enhanced spectroscopy · Molecular spectra · Frequency metrology · Fundamental physics · Precision measurements

Contents

1 Introduction
2 Continuous-wave cavity ring-down spectroscopy
  2.1 Swept-cavity methods
  2.2 Cavity-locked methods
  2.3 Figures of merit
  2.4 Frequency-stabilized CRDS
3 Comb-assisted cavity ring-down spectroscopy
  3.1 Comb-locked frequency-stabilized CRDS
  3.2 Comb-locked frequency-agile rapid-scanning CRDS
  3.3 Comb coherence-transfer in CRDS
  3.4 Cavity-enhanced double-resonance spectroscopy
4 NICE-OHMS
  4.1 Characteristics of signal generation
  4.2 Modulation schemes in NICE-OHMS
  4.3 Contributions to the NICE-OHMS signal
  4.4 Lamb-dip reversals
  4.5 Application of $3f$ demodulation
  4.6 Experimental setup and locking schemes
  4.7 Examples of NICE-OHMS experiments
  4.8 NICE-OHMS operated as an optical clock
5 Examples of cavity enhanced spectroscopic studies of molecules
  5.1 Water
  5.2 Acetylene
  5.3 Carbon dioxide
6 Testing QED with CEAS of molecular hydrogen
  6.1 Rovibrational spectroscopy
  6.2 Doppler-free spectroscopy
  6.3 Comparing theoretical and experimental results
7 Conclusion and perspectives
Acknowledgements
References

1 Introduction

Absorption spectroscopy has been used for over 100 years to study atomic and molecular structure. The basic principle is very simple: illuminate a sample in the gas phase with a light beam of known intensity, I, and measure the amount of light, I_{tr}, that is transmitted through the sample by using a proper detector. Light attenuation at specific wavelengths follows the Beer–Lambert law, so that the intensity decays exponentially as a function of the absorption path length through the sample, L, according to the equation:

$$I_{\mathrm{tr}}(\lambda) = I \exp[-\alpha(\lambda)L]. \tag{1}$$

The absorption coefficient, $\alpha(\lambda)$, usually expressed in cm^{-1}, is proportional to the number density of the absorbing atomic or molecular species, n_x, the proportionality factor being the so-called cross section, $\sigma_x(\lambda)$, with x denoting the particular species in question.

The sensitivity of direct absorption techniques is limited by intensity fluctuations of the light source, so that the minimum detectable intensity change amounts to about 0.001 of the incident intensity, a circumstance that restricts the usage scope of the technique. Many schemes have been developed to increase the detection sensitivity and lower the minimum detectable absorption coefficient as much as possible, especially after the invention of continuous wave (cw) semiconductor diode lasers [1]. This is the case of frequency modulation techniques that minimize the effects of noise in the measurement system [2]. Another strategy is to increase the absorption path-length using multi-pass geometries, to reach a travel distance of up to hundreds of meters, thus lowering the minimum detectable absorption coefficient to $\sim 10^{-7}\ \mathrm{cm}^{-1}$. Commonly used multi-pass cells are White cells [3], Herriot cells [4], and astigmatic mirror cells [5]. The main problem of these systems is the attenuation of the power throughput arising from the reflectivity of the mirrors, the output power being reduced to 1–2% of the input, in the best cases. In addition, the partial overlapping of the reflected beams on the mirror surfaces produces spurious interference fringes that modulate the background signal, thus limiting the achievable signal-to-noise ratio.

Increasing the optical path length can be done more effectively through the use of a high-finesse resonant optical cavity, in techniques like cavity ring-down spectroscopy (CRDS) and cavity-enhanced absorption spectroscopy (CEAS). Compared to the multi-pass cells, optical cavities offer the advantage of a 100–1000 times greater absorption path length, typically obtained in a much smaller volume. The first use of an absorbing medium inside an optical resonator was reported by Jackson [6] as early as in 1961. He resolved the structure of the barium resonance line with an absorbing atomic beam traversing the interior of the interferometer. Soon after that, Alfred Kastler studied absorption of atoms inside a Fabry–Perot interferometer and calculated that this device is equivalent to a long absorption path in an ordinary light beam. He also demonstrated that “the local light intensity in the stationary waves inside can be much higher than the intensity of the incident light beam” [7]. In 1974, Kastler investigated how a pulse of square form is transmitted through a Fabry–Perot interferometer, thus demonstrating the exponential decay of laser light intensity transmitted through an optical cavity, namely, the well-known equation reported hereafter [8]:

$$I_{\mathrm{tr}}(t, \lambda) = I_0 \exp[-t/\tau(\lambda)], \tag{2}$$

where the time constant, τ, is known as the ring-down time, which depends on the cavity optical loss at the wavelength λ, including scattering and mirror losses. In this equation, I_0 represents the intensity of the incident beam.

Since then, there have been many methodological developments mostly motivated by the need to characterize high reflectivity mirrors [9, 10]. Only in 1988, there was the transition from cavity ring-down reflectometry to cavity ring-down spectroscopy. The first measurement of the rate of loss of light intensity from an optical cavity due to an intracavity absorbing medium is attributed to O'Keefe and Deacon, who implemented the pulsed CRDS technique to measure the weak absorption spectrum of molecular oxygen at 630 and 690 nm, achieving a minimum detectable absorption coefficient of 10^{-8} cm^{-1} [11]. This seminal work was responsible for the explosion in terms of popularity of the CRDS method. While the pulsed CRDS technique was mainly used for gas-phase molecular spectroscopy and the detection of gas-phase molecular species in different environments, also applications outside this domain were explored. The CRD-background signals from measurements of pressure ramps were analyzed and converted into a direct determination of Rayleigh-scattering cross sections [12]. The pressure-ramp method was also employed to probe the structure of collision-induced absorption resonances where both colliding molecules become electronically excited [13]. CRDS was extended to the liquid phase in a demonstration experiment measuring an overtone resonance in liquid benzene [14], where reduction of Fresnel losses was achieved by placing a Brewster-angled cell inside a cavity. This technique was developed to detect small liquid samples in liquid chromatography [15]. Further miniaturization could be achieved by omitting cells inside the cavity and using the mirror surfaces as cell walls. Combined with the use of picosecond lasers, very small sample volumes and nanomolar detection limits could be achieved [16], ultimately leading to highly sensitive detectors for high-performance liquid chromatography [17].

The technique of generic pulsed cavity ring-down was then extended to single-mode continuous-wave (cw) dye lasers and extended-cavity diode lasers (ECDL), with the obvious advantage of increasing the spectral resolution and the possibility of increasing the repetition rate at which ring-down transients can be stored, thus leading to an improved sensitivity [18–20]. For a complete and useful reconstruction of the CRDS history, only briefly outlined here, the reader is referred to the review article of Paldus and Kachanov [21].

Parallel to the development of cw-CRDS, single frequency cw lasers offered other interesting possibilities. In 1994, Nakagawa et al. proposed to monitor the cavity transmitted power while the laser was tuned through the cavity modes in the proximity of a given absorption line by any gas sample inside the cavity [22]. The method was tested on a C_2H_2 vibration-rotation transition at 1064 nm to demonstrate the achievement of an effective absorption length of 5.3 km with a 46-cm-long Fabry–Perot cavity. This pioneering work triggered the development of CEAS techniques. The limitation of a few points acquired over a Doppler-broadened profile was overcome in 1999 by the group of Leo Hollberg at the National Institute of Standards and Technology, in Boulder, Colorado. Using an ECDL frequency locked to a tunable cavity, the transmitted power could be recorded while scanning continuously the frequency of a given cavity mode over the absorption line of interest [23]. The fundamental difficulty with this approach is that the cavity transmission mode is generally much narrower than the laser linewidth, so that a fast and tight lock between the laser and the cavity is required. Furthermore, any residual fluctuation of the laser frequency with respect to the cavity resonance is converted into amplitude noise in detection, which makes it difficult to achieve a good sensitivity. A significant improvement in the detection sensitivity can be obtained by using a radio-frequency heterodyne technique in the measurement of the transmitted power. Invented in 1996 by John Lewis Hall, noise-immune cavity-enhanced optical heterodyne molecular spectroscopy (NICE-OHMS) combines the advantages of frequency modulation techniques with cavity-enhanced absorption spectroscopy, with a modulation frequency actively matching the cavity free-spectral-range [24, 25]. Using this method in conjunction with a well-stabilized fixed-frequency laser, Ye et al. demonstrated the detection of a weak sub-Doppler saturated-absorption signal inside an optical cavity, in coincidence with a C_2HD overtone transition, thus reaching the nearly shot-noise-limited sensitivity of $\sim 10^{-14}$ cm^{-1} (with 1 s averaging time) [25]. The technique was then extended to the Doppler-limited regime with frequency spans up to 8 GHz to investigate the weak magnetic-dipole transitions of molecular oxygen at 762 nm [23].

Cavity-enhanced absorption spectroscopy is also feasible without any locking loop [26, 27]. In fact, laser light can be coupled into an optical cavity through accidental coincidences by rapidly modulating the cavity length, while simultaneously modulating the input laser frequency. In this case, the time-integrated intensity of the transmitted light is measured. The method is known as integrated cavity output spectroscopy (ICOS) [27]. Other closely related variants of the CEAS technique include off-axis integrated cavity output spectroscopy (OA-ICOS) [28] and optical-feedback cavity-enhanced absorption spectroscopy (OF-CEAS) [29]. Similarly, there are several variants of the cw-CRDS technique, such as phase-shifted CRDS [30], polarization-dependent CRDS [31], heterodyne CRDS [32], rapidly-swept CRDS [33, 34], broadband CRDS [35], and saturated-absorption CRDS [36]. In addition, complementary cavity-based techniques have been developed, such as cavity mode-width spectroscopy [37] and frequency-based dispersion spectroscopy in an optical cavity [38, 39]. The former method involves determining the absorption coefficient from direct measurements of the spectral width of the cavity modes, once the cavity itself is filled with a gaseous absorbing medium. The latter method uses only the measured frequencies of the cavity modes to provide complete information about the dispersive properties of the intracavity sample near the molecular resonances.

It is not hard to imagine how much these methods have revolutionized the field of trace gas detection and gas metrology, finding widespread applications in environmental and atmospheric monitoring, biomedical analysis with a strong focus on breath analysis [40], and reaction chemistry, due to their ultrasensitive nature. Moreover, they have been widely recognized as a valid alternative to isotope ratio mass spectrometry for the accurate analysis of the isotopic composition of gaseous samples, with a number of relevant applications in hydrology, climatology and paleoclimatology, geochemical research [41], as well as radio-carbon dating [42].

There are already several reviews of the extensive literature regarding these techniques and their applications, describing the experimental developments and realizations, as well as the underlying theory [21, 34, 43–46]. Therefore, the present review is not aimed to provide a complete description of the works published in the field of cavity-enhanced and cavity ring-down spectroscopies. Instead, this paper focuses on the recent implementations that combine the extremely high sensitivity in detecting a weak absorption spectrum with the amazing precision of optical frequency measurements that is achievable by exploiting the technology of optical frequency comb synthesizers. We intend to give an overview of the state-of-the-art cavity-based molecular spectroscopy methods that are currently used to provide highly accurate data and, in some cases, to test quantum electrodynamics (QED) calculations.

The structure of the review is as follows. In Sect. 2 we resume basic concepts and main features of cw-CRDS, also describing selected implementations. Section 3 is devoted to a review of the recent literature regarding comb-calibrated CRDS, while Sect. 4 deals with NICE-OHMS and its comb-assisted variant. Section 5 concentrates on recent applications to precision spectroscopy of a few selected molecules, such as water, acetylene, and carbon dioxide. In Sect. 6 we focus on precision measurements of molecular hydrogen spectra to test the QED theory. Conclusions and future perspectives are given in the last section.

2 Continuous-wave cavity ring-down spectroscopy

Cavity ring-down spectroscopy consists in measuring the rate of decay of light intensity inside a stable optical resonator, once the incident laser radiation is instantaneously switched off. The optical cavity is typically formed by a pair of concave spherical mirrors with radii of curvature r_1 and r_2, mounted to share the optical axis and separated by a distance L. The geometrical features satisfy the stability condition, as reported here below:

$$0 < g_1 g_2 < 1, \tag{3}$$

with g_1 and g_2 given by $1 - L/r_1$ and $1 - L/r_2$, respectively. The Gaussian beam solution of the paraxial wave equation leads to the well-known mode structure that includes longitudinal and transverse modes, as defined by a set of three integers: q, m and n, with q being associated to the longitudinal modes, while m and n identify the transverse distribution of the wave energy. For an empty cavity, the frequency difference between two adjacent longitudinal modes, q and $q + 1$, with the same values of m and n, is the cavity free spectral range (FSR), given by FSR = $c/2L$, c being the vacuum speed of light. A cw single-mode tunable laser is used to excite a single cavity mode. If I_0 is the transmitted light intensity at the time the incident light beam is switched off, the transmitted intensity decays exponentially according to Eq. (2), with a decay rate $D(\lambda)$ given by $1/\tau(\lambda)$. It is possible to show that the decay rate of an empty cavity consisting of high reflectivity mirrors ($R \rightarrow 1$) is given by:

$$D(\lambda) = c\frac{T + S}{L}, \tag{4}$$

where T is the mirror transmittivity and S is the scattering loss, with $T + S + R = 1$. If an absorbing medium in the gas phase is placed between the cavity mirrors, thus filling the entire intracavity volume, Eq. (4) is modified in the following way:

$$D(\lambda) = c\left[\frac{T + S}{L} + \alpha(\lambda)\right]. \tag{5}$$

Therefore, by measuring the change in the cavity decay rate, an absolute determination of the absorption coefficient of the intracavity sample can be performed, according to the following equation:

$$\alpha(\lambda) = \frac{1}{c}\left[\frac{1}{\tau(\lambda)} - \frac{1}{\tau_0}\right], \tag{6}$$

τ_0 being the decay time measured under vacuum conditions, a fundamental characteristic of any CRDS spectrometer. Note that Eq. (6) shows that CRDS measurements are not dependent on either the incident radiation intensity or the absorption path length, circumstance that makes the CRDS technique very attractive for fundamental studies and applications. Resorting to the quantum nature of light, τ_0 represents the photon lifetime inside the cavity in the absence of any intracavity absorption. Today's mirror manufacturing technology easily allows one to obtain a pair of mirrors with a reflectivity as high as 0.99995 in the near-infrared spectral region. For $L = 0.5$ m, assuming a negligible scattering loss, τ_0 amounts to about 33 μs, which translates into an effective photon path length, $L_{\text{eff}} = c\tau_0$, of about 10 km. The thousands-fold increase in effective path length ensures the enhanced sensitivity of the CRDS technique over traditional direct absorption spectroscopy. The most significant advantage of the cw variant of CRDS, compared to earlier implementations based on pulsed laser sources, is that the intensity decay from the cavity is a true single exponential process since the excitation of a single cavity mode at a time takes place. Multiple longitudinal and transverse mode excitation, as observed by using pulsed lasers, results in multi-exponential decays that compromise the accurate retrieval of the ring-down time, although a condition can be achieved of a white-light cavity for which an exponential decay can be attained [47].

The highest sensitivity for a CRDS experiment can be reached only using cw lasers emitting on a relatively narrow single mode. For the visible and near-infrared spectral regions, convenient laser sources are ECDLs or distributed-feedback (DFB) diode lasers, with typical emission bandwidths of 100–200 kHz and 1–2 MHz, respectively. Relatively high powers are strongly desired because of the inefficient coupling between the laser and the cavity modes, whose width can be of the order of a few kHz. In any case, strategies are required for a controlled and highly reproducible cavity excitation, aimed to reduce as much as possible the shot-to-shot variations in repeated ring-down events.

2.1 Swept-cavity methods

The most practical option, known as swept-cavity method, is described in Fig. 1. The cavity length is scanned over a distance larger than $\lambda/2$ using a piezoelectric transducer, to bring a cavity mode into resonance with the laser mode, at any frequency of the incident radiation. When a sufficient amount of light builds up inside the optical cavity, a simple electronic circuit based upon a threshold detector produces a TTL pulse that is used to shut the laser off with an acousto-optic modulator. By properly setting the threshold signal, it is possible to detect only the occurrence of the fundamental transverse mode (TEM_{00}) excitation of the cavity.

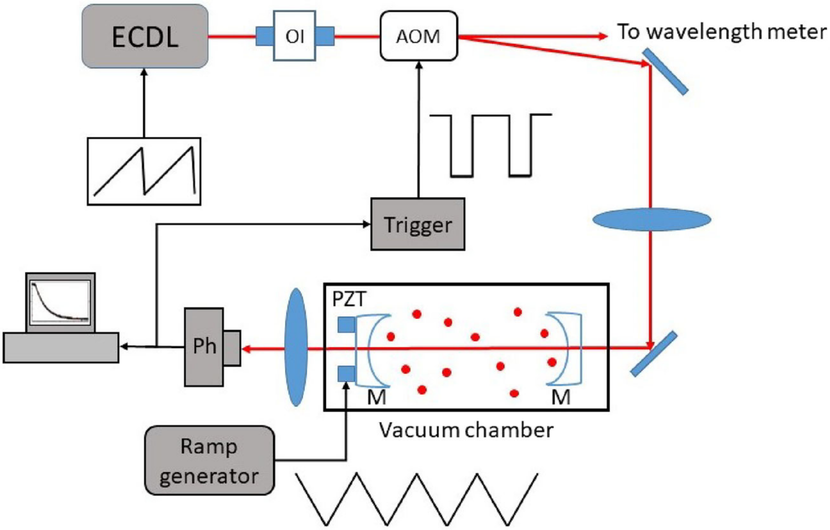

Fig. 1 Schematic diagram of a cw-CRDS spectrometer with a swept-cavity approach. ECDL stands for extended-cavity diode laser; OI for optical isolator; AOM for acousto-optic modulator; PZT for piezoelectric actuator; Ph for photodiode; M for high reflectivity mirror. The 1st-order diffracted beam is injected into a high finesse optical resonator that is housed inside a vacuum chamber

Over the years, several variants of the swept-cavity method have been developed [33, 34, 48]. A complete coverage of the field is doomed to fail, considering the large amount of work that has appeared after the pioneering articles of Romanini and co-workers [18, 19]. Within the focus of this review article, we merely point out that the minimum detectable absorption coefficient of swept-cavity methods ranges from 10^{-8} to 10^{-10} cm^{-1}, limited by the repeatability in the amount of injected power into the cavity from shot to shot. Higher sensitivities are achieved by locking together the laser frequency and a cavity resonance so that more reproducible intracavity intensities and transmitted signals can be obtained. Additionally, a high repetition rate can be achieved in the detection of repeated exponential decays so that averaging over several decay events can be performed to obtain a more precise value of the decay time, thus increasing the sensitivity.

2.2 Cavity-locked methods

Typically, two different approaches are implemented for locking: Active opto-electronic locking by means of the Pound–Drever–Hall technique [49]; and passive locking by exploiting optical feedback from the cavity [50].

A cavity-locked cw ring-down scheme was implemented for the first time by Paldus et al. [20]. This scheme employed the Pound–Drever–Hall (PDH) technique to achieve a tight frequency lock of the laser to the cavity. The underlying idea is very simple: Locking the laser frequency to the center of the TEM_{00} mode of an optical resonator through a feedback system, laser light is permanently injected into the cavity. Two laser polarizations are initially created and separated for different uses. The p-polarization is used to lock the laser to the cavity, while the s-polarization is sent through an AOM prior to injection into the cavity. This AOM is then used to generate exponential decay events by switching off the s-polarized beam. In this way, it is possible to generate and register repeated decay events at repetition rates of tens of kilohertz, thus detecting only one polarization while the other is used to keep the laser and cavity tightly locked at all times. Measuring weak absorption lines of CO_2 at 1064 nm, a minimum detectable absorption coefficient of 8.8×10^{-12} cm^{-1} for 1 s averaging time was demonstrated using the dual-polarization approach [51].

A valid alternative to this dual-polarization method is known as periodically locked CRDS. An ECDL is tightly locked to a high-finesse cavity and the light entering the high-finesse cavity is periodically switched off and on by using an AOM. In coincidence with each ring-down event, the PDH lock is interrupted. Once the light to the cavity is switched on again, the cavity lock is rapidly reacquired [52, 53]. In Ref. [52], it was shown that as many as 16,000 ring-down events per second could be acquired, while scanning the cavity mode frequency of about 4 GHz in approximately 20 s. The method was applied to the sensitive detection of very weak overtone transitions of acetylene at 788 nm. Much broader scans were obtained in the same spectral region by using a cw, single mode, Ti:sapphire ring laser [53]. In this case, 500 steps were used to cover a scan range of 1 cm^{-1}, accumulating 10,000 exponential decays for each point. This translated into a total duration of the scan of about 9 min. Faster scanning speeds were tried by keeping constant the number of frequency steps and accumulating a smaller number of exponential decays at each point. It was found that the system was perfectly usable and the lock was stable up to speeds of $\sim$3 GHz/s, which implied spectral acquisition over 1 cm^{-1} in only ten seconds by accumulating 200 exponential decays per point. The price to pay is, of course, a reduced sensitivity. In summary, there are important trade-offs to be found in any cavity-locked CRDS system with regard to optimizing the sensitivity, frequency resolution, scan width, and duration.

To mitigate this issue, Hodges and co-workers at the National Institute of Standards and Technology invented a new approach known as frequency-agile rapid scanning cavity ring-down spectroscopy (FARS-CRDS) [54, 55], in which the laser frequency is rapidly stepped to successive resonances through the use of high bandwidth electro-optic modulator in conjunction to a microwave driver. This technique allows for ultrasensitive measurements with an acquisition rate that is limited only by the cavity response in ring-down events. In fact FARS-CRDS eliminates any dead time due to scanning of the cavity mode frequency and the laser frequency. Another important feature consists in the use of the cavity as a spectral filter such that only a single, selected sideband is resonant. Ring-down events are then initiated by simply switching off the microwave frequency, thus removing the need for an acousto-optic modulator.

Early demonstrations of this technique were based upon DFB diode lasers and ultra-narrow linewidth fiber lasers [54]. Subsequently, FARS-CRDS was implemented with a widely tunable external-cavity diode laser, with an emission wavelength between 1570 and 1630 nm [55]. This latter configuration is depicted in Fig. 2. Two orthogonal, linear polarizations of the ECDL are produced, the former providing a continuous high-bandwidth lock to the ring-down cavity, the latter being stepped mode-by-mode

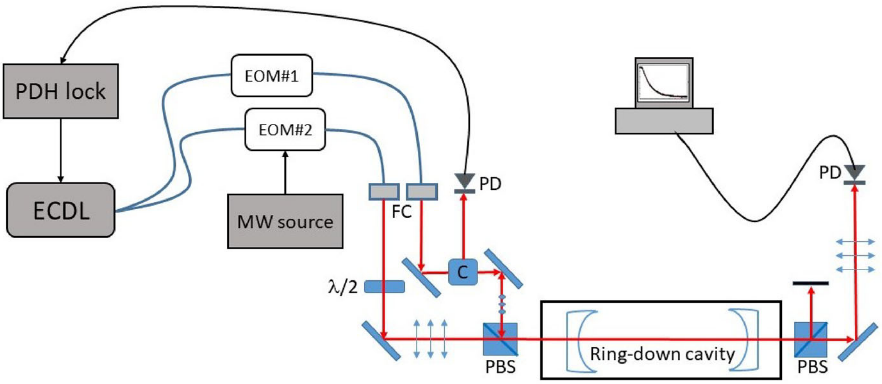

Fig. 2 Schematic diagram of a FARS-CRDS spectrometer. ECDL stands for external-cavity diode laser; EOM for electro-optic modulator; PBS for polarising beam splitter; PD for photodiode; λ/2 for half-wave plate; FC is a free-space fiber coupler, while C is a circulator

of the cavity. To this purpose, a pair of waveguide electro-optic modulators are used. In both cases, the carrier frequency is not resonant. In fact, unlike conventional PDH locking, Long and co-workers locked one of the sidebands to the optical cavity. The probe beam is phase-modulated at a microwave (MW) frequency such that only a selected sideband is resonant with the cavity. Its frequency can be rapidly changed by the MW source in increments of the cavity free-spectral-range, thus covering the lineshape of a given molecular resonance of interest. This approach ensured spectral acquisitions with a scan rate as high as 1000 GHz/s, while the minimum detectable absorption coefficient was measured to be 1.7×10^{-11} cm^{-1} after only 20 ms of averaging [55]. It is worth noting that the PDH lock is not interrupted during a ring-down event. Moreover, the high-bandwidth lock provides common mode rejection of amplitude noise in the transmitted signal, caused by the frequency jitter between the probe laser and the selected cavity mode.

The idea of using the sideband of a frequency-stabilized laser as the tunable probe beam of a cavity ring-down spectrometer was first proposed and implemented by the Hefei group in 2011 [56]. A schematic diagram of the laser-locked sideband cavity ring-down spectrometer is shown in Fig. 3.

In this experiment, the cw laser source, a tunable Ti:Sapphire laser pumped by a 532-nm solid-state laser, is tightly stabilized against a longitudinal mode of an isothermal ultra-stable optical cavity built with an ultra-low-expansion (ULE) glass. The selection of the sideband to be injected into the ring-down cavity is accomplished by means of a second cavity with a low finesse (referred to as etalon in the figure), whose length is actively controlled so that only one sideband is resonant with the cavity. As with swept-cavity methods, the length of the ring-down cavity is scanned to bring a cavity mode into resonance with the sideband, so that a ring-down event can be triggered [56]. Obviously, the use of an optical cavity for spectral filtering of phase-modulated radiation adds some complexity to the apparatus. A very elegant alternative, as proposed in Refs. [57, 58], is based upon an integrated lithium-niobate electro-optic modulator with a nested Mach–Zehnder interferometer waveguide structure. Applying

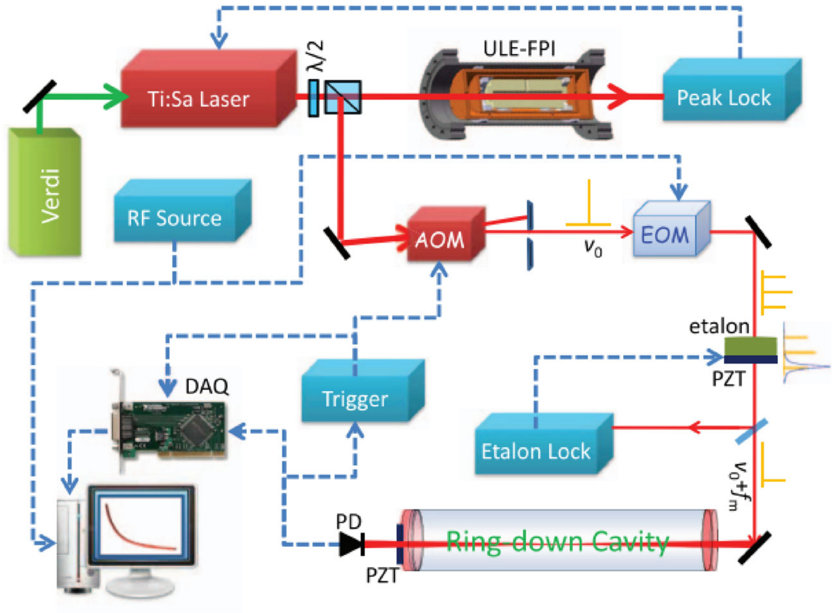

Fig. 3 Schematic diagram of the laser-locked sideband cavity ring-down spectrometer. *AOM* acousto-optic modulator, *DAQ* data acquisition card, *EOM* electro-optic modulator, *PD* photodiode, *PZT* piezoelectric actuator, *ULE-FPI* Fabry–Perot interferometer made of ultra-low-expansion glass. Reprinted from [56], with the permission of AIP Publishing

a pair of orthogonal radio frequency signals in the GHz range to the modulator, multiple voltage-controlled interferences in the Mach–Zehnder waveguide can be generated, thus leading to a single-sideband modulation signal with suppressed carrier [57]. The single sideband is then injected into the ring-down cavity [58].

A further element of novelty of the CRDS implementation reported in [58] is given by the cw laser source, namely, a distributed feedback diode laser that is locked to a highly stable V-shaped reference cavity by optical feedback. The stability of this narrow laser is transferred to the ring-down cavity employing a PDH locking scheme. A near-shot-noise-limited regime was achieved, with the remarkable result of an absorption detection sensitivity equal to $5\ \times 10^{-13}$ cm^{-1} over 1 s [58]. The latter implementation can be considered an evolution of an earlier apparatus in which optical feedback was used for passive self-locking of an ECDL to the ring-down cavity [59]. This approach is known as optical-feedback cavity ring-down spectroscopy (OF-CRDS). In this respect, it is relevant to mention that optical feedback produces a strong effect, which narrows the laser emission spectrum below the cavity-mode width, provided that the amount and phase of feedback radiation are properly adjusted [29].

2.3 Figures of merit

So far in this section, we have repeatedly mentioned the sensitivity in terms of minimum detectable absorption coefficient, $\alpha_{\min}$. This is commonly expressed as:

$$\alpha_{\min} = \frac{1}{c\tau_0}\left(\frac{\Delta\tau_{\min}}{\tau_0}\right), \tag{7}$$

where $\Delta\tau_{\min}$ is the minimum measurable change of the ring-down time, given by the standard deviation of repeated measurements of the empty-cavity decay time. Equation (7) tells us that the higher is the decay time the lower is $\alpha_{\min}$ and, hence, the higher is the sensitivity. $\Delta\tau_{\min}$ is influenced by mechanical, thermal, and electronic noises, which affect the detector signal as a function of time as it follows:

$$V_{\mathrm{tr}}(t) = V_0 \exp[-t/\tau_0] + B + \epsilon(t), \tag{8}$$

$\epsilon(t)$ being the noise, V_0 the ring-down amplitude signal, and B the detector offset or the possible baseline due to finite light extinction. The two intrinsic electronic noise sources in CRDS are shot noise and detector noise, the latter being expressed by the noise equivalent power (NEP), measured in Watt/$\sqrt{\mathrm{Hz}}$. For the detector-noise-limited (DNL) case, $\Delta\tau_{\min}$ takes the meaning of statistical uncertainty (σ_τ) on the decay time that results from the nonlinear least-squares fit of a single exponential decay, given by [60]:

$$\sigma_\tau^{(\mathrm{DNL})} = \frac{2 \times \mathrm{NEP}}{P_0}\sqrt{\tau_0}, \tag{9}$$

where P_0 is the peak power of the ring-down event. Similarly, in the shot-noise-limited (SNL) case, the following equation holds [60]:

$$\sigma_\tau^{(\mathrm{SNL})} = \sqrt{\frac{e\tau_0}{P_0 S}}, \tag{10}$$

where S is the photodetector responsivity (in A/W) and e is the electron charge. These two quantities are relevant to understanding how far a given CRDS apparatus is from optimal implementation.

An alternative tool to express the detection sensitivity is the noise-equivalent absorption coefficient (NEA), which takes into account also the ring-down acquisition rate (f_{rep}), according to the following formula:

$$\mathrm{NEA} = \alpha_{\min}\sqrt{\frac{2}{f_{\mathrm{rep}}}}. \tag{11}$$

2.4 Frequency-stabilized CRDS

We conclude this section by discussing a refinement of cw-CRDS, known as frequency-stabilized cavity ring-down spectroscopy (FS-CRDS), which allows one to combine high sensitivity with high resolution, frequency accuracy, stability, and reproducibility [61, 62]. Here, the influence of residual frequency jitter between the probe laser and a given cavity mode is mitigated by stabilizing the optical cavity to an absolute frequency reference. To this purpose, the cavity is built with a pair of dichroic mirrors that are designed to have relatively high losses and low losses at the respective wavelengths of the reference and probe lasers. In the first implementation, the reference laser was a frequency-stabilized He–Ne laser and the cavity length was locked to the reference laser using a servo scheme that stabilized the transmission of the reference laser light [61]. Subsequently, the PDH locking technique was effectively employed to further enhance the achievable signal-to-noise ratio [63, 64]. Therefore, the main feature of FS-CRDS is the stable, accurate, and linear frequency axis that is produced by the actively-stabilized comb of cavity resonances. Furthermore, self-calibrated spectra are obtained, the frequency separation between two adjacent points of each spectrum being exactly equal to the cavity FSR splitting frequency [65]. If the coarse scanning is set by the cavity FSR, fine scanning around each cavity mode is possible by shifting the reference He–Ne laser frequency with a double-passed AOM [66].

FS-CRDS was revealed to be particularly suitable for high-precision studies of line shapes aimed to test semi-classical theories, as well as measurements of spectroscopic parameters of molecular near-infrared transitions. In this respect, the past literature is rich in beautiful examples for O_2, CO_2, and H_2O [64, 67, 68]. A disadvantage of this method is that customized two-color mirrors are needed. In addition, the stability of the cavity length, therefore the frequency accuracy of each cavity mode, is limited by the frequency stability of the He-Ne laser, which is usually at the level of 1 MHz. Different and more powerful FS-CRDS approaches are possible by exploiting the technology of optical frequency-comb synthesizers (OFCS), as it will be shown in the next section.

3 Comb-assisted cavity ring-down spectroscopy

The advent of optical frequency comb lasers, invented by Hänsch [69] and by Hall [70], has given new capabilities to high resolution and high sensitivity molecular spectroscopy, providing a very effective tool for absolute frequency calibration in the optical domain with direct traceability to the primary standard of time and frequency. The secret of the happy combination of resonant cavities and frequency combs lies in the regularly spaced, highly stable, comb teeth over an octave-spanning spectrum, each of them being characterized by an absolute frequency. This feature ensures a highly accurate and repeatable frequency axis underneath a CRDS spectrum. In the earliest configurations, the tunable near-IR probe laser of a frequency-stabilized CRDS spectrometer is linked to the comb, meaning that the offset frequency between the probe laser and the nearest tooth of the comb is measured by beat-note detection, each time the laser is resonant with the cavity [71, 72]. This method is usually referred to as comb-linked, frequency-stabilized cavity ring-down spectroscopy [72]. If cavity stabilization is waived, a simplification of the optical setup can be achieved, as proposed by Gatti et al. [73]. In this latter scheme, known as comb-locked cavity ring-down spectroscopy (CL-CRDS), the probe laser is tightly locked to a frequency comb, while the CRDS apparatus operates in a cavity-swept mode. Tuning of the comb repetition rate

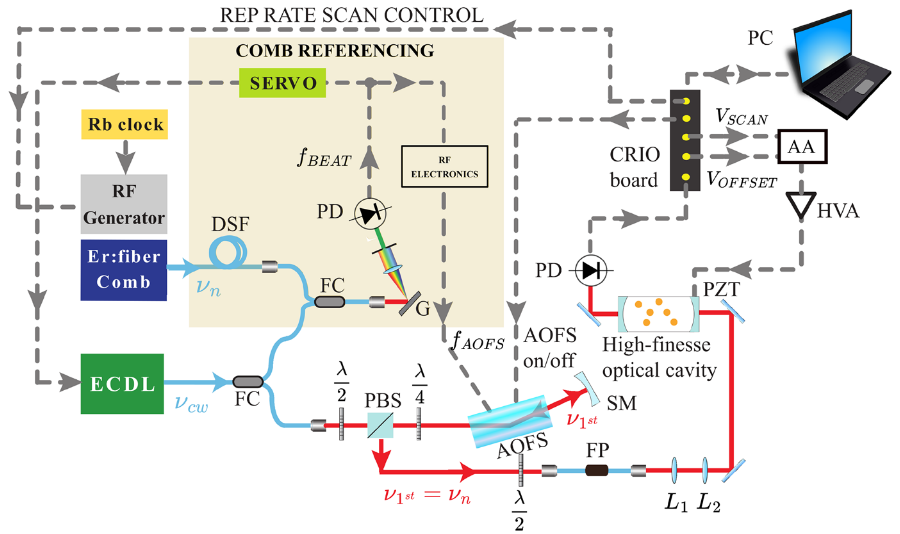

Fig. 4 Experimental scheme of a comb-locked CRDS apparatus. *AOFS* acousto-optic frequency shifter, *PZT* piezoelectric transducer, *FC* fiber coupler, *DSF* dispersion-shifted fiber, *PD* photodetector, *G* diffraction grating, *PBS* polarizing beam splitter, *FP* in-line fiber polarizer, *SM* spherical mirror, *HVA* high-voltage amplifier, L_1 and L_2 lenses, *AA* analog adder, *CRIO* compact reconfigurable input/output board. The scheme is inspired from Ref. [73]

results in precisely controlled frequency scans. The cavity is simply made to slowly follow the comb-referenced scan of the probe laser by using proper tracking electronics. The layout of the CL-CRDS spectrometer, as proposed in Ref. [73], is sketched in Fig. 4.

The main advantage of this approach is that laser frequency steps can be made arbitrarily small without the need to match them with the cavity free spectral range. Therefore, the acquisition of highly dense spectra is possible, suitable for the precise investigation of line-shape models or the acquisition of ultra-narrow spectral features, such as those observed in the saturated-absorption regime.

3.1 Comb-locked frequency-stabilized CRDS

The natural evolution of the works discussed above led to the so-called comb-locked frequency-stabilized cavity ring-down spectroscopy (CL-FS-CRDS), a rather sophisticated technique that enables Lamb-dip observations in coincidence with weak molecular transitions. It is useful to remind us that saturated absorption spectroscopy is a powerful method to overcome the limitations imposed by Doppler broadening. In fact, saturated transitions exhibit a Lamb dip at their line center whose width is 2–3 orders of magnitude narrower than the Doppler-limited spectrum. A beautiful example is reported in Fig. 5, which shows the Lamb dip of an $H_2{}^{18}O$ rovibrational line at 1.39 μm as recorded in a low-pressure air sample using a CL-FS-CRDS apparatus developed in Caserta. The latter will be described later on in this section.

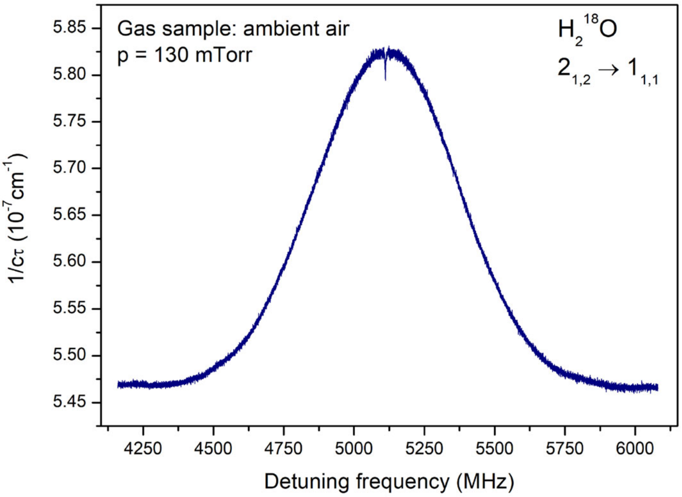

Fig. 5 Example of a Lamb-dip CRDS spectrum in coincidence with the $2_{1,2} \rightarrow 1_{1,1}$ component of the $H_2{}^{18}O$ $\nu_1+\nu_3$ band

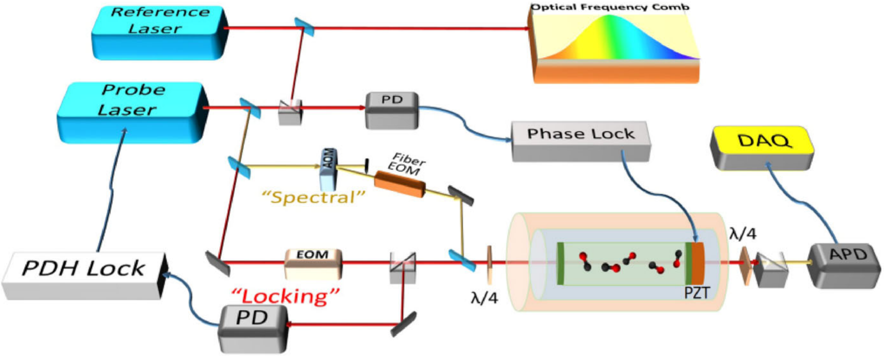

Fig. 6 Example of CL-FS-CRDS setup. The reference laser is locked to a self-referenced optical frequency comb. The probe laser frequency is locked to the ring-down cavity (by using the "locking" beam). Another beam from the probe laser ("spectral" beam) is frequency-shifted and used for the CRDS measurements. The ring-down cavity length is stabilized according to the beat signal between the probe and reference lasers. *AOM* acousto-optic modulator, *APD* avalanche photodiode, *DAQ* data acquisition system, *EOM* electro-optic modulator, *PD* photodiode, *PZT* piezo actuator. Reprinted from [74], with the permission of AIP Publishing

In 2017, the Hefei group performed absolute frequency measurements for a pair of CO lines, belonging to the second overtone vibrational band at the wavelength of 1.54 μm, with a frequency accuracy of 500 Hz (corresponding to a relative uncertainty of 2.6×10^{-12}) [74]. At the same time, the remarkable sensitivity of 3.5×10^{-12} cm^{-1} was achieved at an averaging time of about 70 s. The apparatus is depicted in Fig. 6, while a few examples of cavity ring-down Lamb-dip spectra for the R(10) line, in the CO pressure range between 0.2 and 1.5 Pa, are shown in Fig. 7. Using a similar setup, operating at the wavelength of 787 nm, the same Chinese team built a primary gas

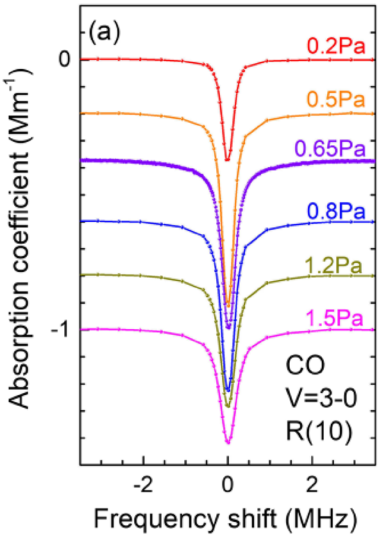

Fig. 7 Lamb dip spectra of the R(10) component in the 3-0 band of the CO molecule. Despite the high saturation power, which is estimated to be 1500 W/cm^2, nonlinear spectroscopy is possible since the resonance effect considerably enhances the intracavity laser power. Adapted from [74], with the permission of AIP Publishing

thermometer based on Doppler-broadened spectrometry in a C_2H_2 sample [75]. As it is well known, Doppler-broadening thermometry (DBT) consists in retrieving the Doppler width ($\Delta\nu_D$) from the highly accurate observation of the shape of a given atomic or molecular line, in a gas at thermodynamic equilibrium [76]. Once $\Delta\nu_D$ and the central frequency, ν_0, are measured, if the atomic or molecular mass (M) is known, the inversion of the well-known equation

$$\Delta\nu_D = \frac{\nu_0}{c}\sqrt{8\ln 2\frac{k_B T}{M}}, \tag{12}$$

allows one to determine the thermal energy and, consequently, either the gas temperature (T) or the Boltzmann constant (k_B). The Hefei group demonstrated a relative statistical uncertainty of 6 ppm (part per million) in the determined linewidth values by repeated measurements over several hours, at a sample pressure of only 1.5 Pa [75]. As for the retrieved temperature, a systematic deviation of about 800 ppm limited the applicability of the method. Such a shift was attributed to hidden weak lines overlapped with the selected C_2H_2 transition that perturbed the observed lineshape. A better performance in terms of accuracy was demonstrated for DBT by developing CL-FS-CRDS at 1.578 μm to probe the $P_e(12)$ line of the (30012) ← (00001) band of carbon dioxide [77]. CO_2 was revealed to be an excellent choice for the aims of DBT since it is a centrosymmetric linear molecule with only three fundamental vibrations, thus showing a simplified infrared spectrum as compared to many other polyatomic molecules. It is no coincidence that this species was chosen for the spectroscopic determination of the Boltzmann constant in one of the pioneering DBT experiments [78]. Moreover, CO_2 spectral lines do not exhibit hyperfine structure, while the lack of a permanent dipole moment reduces significantly the interactions with the cell walls.

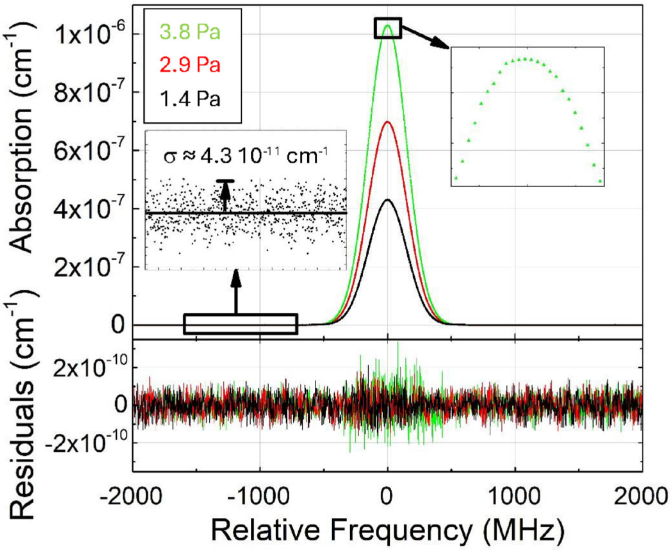

Fig. 8 Example of CL-FS-CRDS spectra in coincidence with a weak overtone transition of CO_2 at 1.578 μm. As a result of the application of a sophisticated line fitting procedure, the Doppler width and the center frequency can be simultaneously retrieved, thus leading to an accurate gas temperature determination. The OFCS is stabilized against a GPS-disciplined Rb clock, circumstance that ensures the traceability to the SI standard of time and frequency. Reprinted (Fig. 2) with permission from [77], Copyright (2018) by the American Physical Society

Therefore, exploiting a very favorable combination of high sensitivity, accurate frequency calibration, and dense frequency grid, together with a powerful multispectrum fitting procedure applied to a large set of spectra at different pressures, it was possible to measure thermodynamic gas temperatures with statistical and systematic uncertainties of 8 ppm and 11 ppm, respectively. Figure 8 shows a few examples of CO_2 spectra, along with the results of nonlinear least-squares fits of the observed profiles.

Another interesting development was reported in 2018 by Kassi et al., who implemented the link to a self-referenced optical frequency comb synthesizer for an optical-feedback frequency-stabilized CRDS apparatus [79]. Three main features make this setup quite interesting. First, the V-cavity-based optical feedback leads to a sub-kHz laser emission, thus ensuring a very efficient and stable coupling of the probe laser into the ring-down cavity. Second, the ring-down cavity is robustly dither-locked to the stabilized laser rather than being tightly locked by means of the Pound–Drever–Hall technique, with the advantage of making the system prone to frequent unlocking and re-locking. Finally, high resolution is combined to high frequency accuracy by referencing the laser source to the OFCS. Lamb-dip spectrometry was performed for H_2O rovibrational lines near 1.39 μm, resolving K-type doublets and measuring absolute frequencies at the kHz uncertainty level. The experiment was aimed to perform an accurate test of quantum chemical calculations [80]. It is worth noting that molecular transition frequencies, when measured at the kHz uncertainty level, can act as

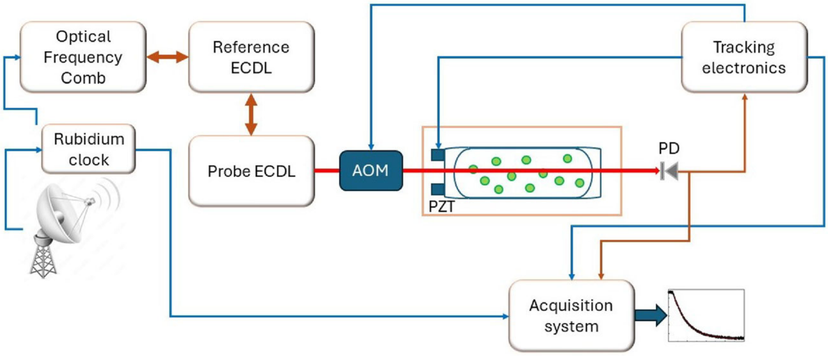

Fig. 9 Schematic diagram of the CL-FS-CRDS spectrometer developed in Caserta. Operating at the wavelength of 1.39 μm, the system was used for precise measurements of water densities and mole fractions in ultra-high purity gases [82, 83]. It was also used for measuring the absolute line center frequency of the R(1) 2-0 rovibrational transition of the HD molecule [84]

secondary frequency standards useful for length metrology and telecommunications applications [81].

Almost at the same time, the Caserta group managed to obtain exactly the same features by implementing a different strategy, which is schematically shown in Fig. 9 [82]. The apparatus is based on the use of a pair of phase-locked extended cavity diode lasers, emitting at 1.39 μm, one of them (namely, the reference laser) being tightly locked to an optical resonator by using the Pound–Drever–Hall method so as to narrow its emission linewidth down to ~ 7 kHz for an observation time of 1 ms. In turn, the resonator is locked to a self-referenced OFCS in a bandwidth of only few tens of Hz. Therefore, the OFCS has a twofold task: to provide an absolute calibration for the reference laser; to compensate for slow drifts of the resonator due to temperature variations or electronic instabilities. Coherence is effectively transferred from the reference laser to the probe laser using the optical phase-locking loop that is described in Ref. [85]. An intrinsically stable high finesse optical cavity, built on a Zerodur spacer with a cylindrical hole along its axis, was used as ring-down cavity. By scanning the offset frequency between reference and probe lasers, it was possible to perform highly reproducible and accurate frequency scans of the probe laser around an arbitrary center frequency [86]. A proper tracking servo-loop electronics was implemented so that the cavity could follow the probe laser frequency variations. Its operation (as described in Fig. 10) deserves a brief description, even as an example of a typical tracking circuit [87].

The tracking electronics essentially consists of (i) a ramp generator, (ii) a threshold detector, and (iii) a microcontroller unit (MCU). The output signal of the photodiode (PD) is used as input to the threshold detector, to monitor whether a resonance condition takes place. By properly setting the threshold signal, it is possible to detect only the occurrence of a TEM00 excitation. In this case, a TTL pulse is produced and sent, as a trigger signal, to the acquisition system, to the MCU, and to the AOM driver to switch off the laser. The ramp generator gives a voltage ramp to the cavity PZT. The MCU actively controls the ramp generator while looking for the TTL pulse. For a given laser frequency, the cavity is scanned until a first resonance is detected. At this point,

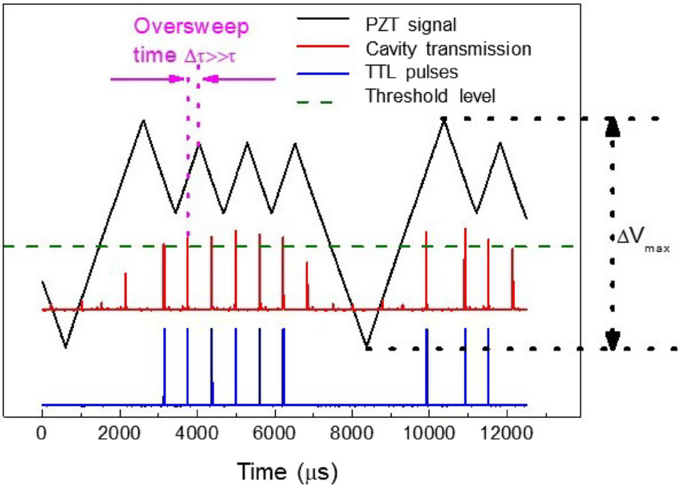

Fig. 10 Operation of the tracking electronics developed in Ref. [82]. ΔV_{max} leads to a change of the cavity mode frequency of about one FSR

the AOM is turned off and the acquisition of the ring-down event starts. Meanwhile, the PZT is still swept in the same direction for an oversweep delay time, Δt. After this time interval, the slope of the PZT ramp is changed in sign (through the action of the MCU), thus forcing the cavity to go back towards the resonance. As a result, the cavity moves back and forth in a narrow frequency range around the resonance. This is done to enable repeated acquisitions of ring-down events, in coincidence with the same cavity mode. When the laser frequency is changed, the tracking circuit restarts this procedure.

3.2 Comb-locked frequency-agile rapid-scanning CRDS

In Sect. 2, the advantages of the FARS-CRDS technique have been discussed, with special emphasis on the outstanding scan speed, limited only by the cavity response time in ring-down events. The comb-locked variant of this method was found to be very powerful for the aims of precision measurements of molecular transition frequencies. In fact, frequency metrology at the 10^{-12} relative uncertainty level was demonstrated for a few CO_2 lines at 1.57 μm, without resorting to the saturated absorption regime [88]. The key attributes of comb-locked FARS-CRDS are the ability to rapidly scan the probe laser while maintaining the phase lock to the OFCS and the high stability of the frequency axis. In their experiment, Reed et al. achieved a relative stability for the frequency axis of 2×10^{-13} for an observation time of 60 s, which corresponded to the time span of a single spectrum acquisition [88]. The high signal-to-noise ratio ($\sim$ 30,000) in conjunction with the long-term averaging of the retrieved line center frequencies led to a statistical uncertainty of the order of 200 Hz, a quite remarkable result for a Doppler-limited experiment.

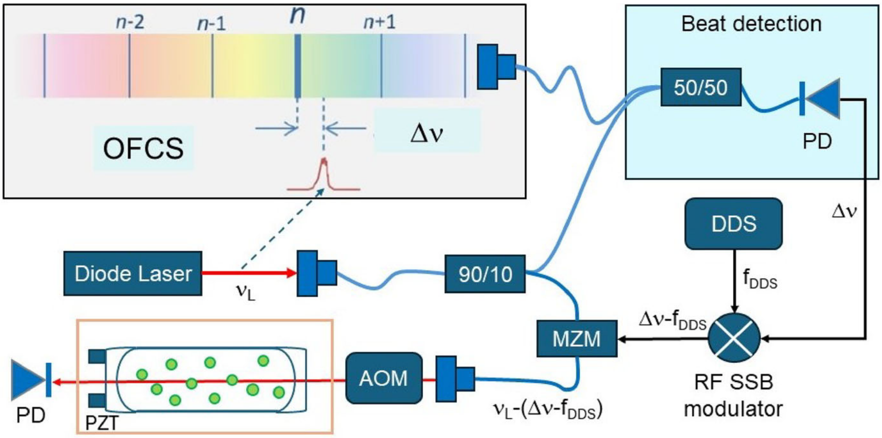

Fig. 11 Simplified scheme of a CL-CRDS spectrometer based upon the CCT technique. Figure adapted from [90]

3.3 Comb coherence-transfer in CRDS

As the latest example of an advanced comb-locked CRDS spectrometer, we mention the one based upon the comb coherence-transfer (CCT) technique, introduced for the first time by Gotti et al. [89]. The CCT approach consists of a direct coherence transfer from a selected OFCS tooth to an ECDL or a DFB diode laser. The novelty is that CCT does not use a phase look loop, which is difficult to implement especially when using lasers with a line emission width larger than 1 MHz. The CCT technique employs a high-bandwidth feed-forward control acting on an optical single-sideband modulator, rather than correcting the injection current of the diode laser. The principle of operation is described in Fig. 11. The beat note signal (provided by the fast photodiode, PD, of Fig. 11), which carries information on the frequency difference ($\Delta\nu$) between the diode laser and the nearest OFCS tooth, is injected into an RF single-sideband (SSB) modulator that adds a tunable RF offset frequency (f_{DDS}) provided by a direct digital synthesizer (DDS). This signal drives an optical SSB generator (a telecom Mach–Zender modulator, MZM). The selected sideband at the MZM optical output is the one with a subtracted RF-shifted beat note, thus leading to a nearly perfect clone of the comb mode, shifted by the tunable RF offset. Therefore, regardless of the width of the laser, it is possible to produce a narrow, SI-traceable, probe laser radiation that can be effectively injected into a high-finesse ring-down cavity. The performance of the system can be eventually improved with an additional locking of the comb to an ultra-stable optical frequency reference, as demonstrated in Ref. [90]. This spectrometer was employed for extensive Lamb-dip investigations of the $2\nu_3$ band of $^{12}CH_4$ at 1.65 μm, as well as the 20012-00001 and 20013-00001 combination bands of $^{12}CO_2$ in the 1.99–2.09 μm region, thus measuring transition frequencies with kHz-accuracy [90, 91].

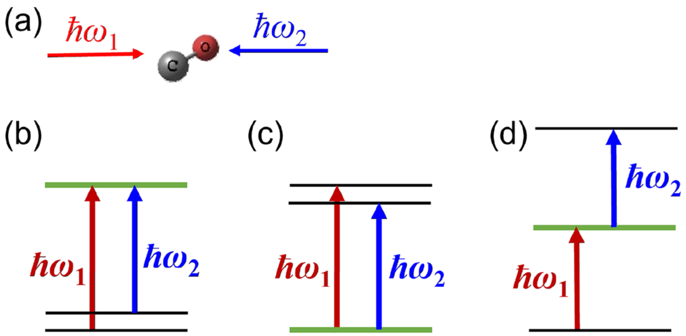

Fig. 12 (**a**) A molecule interacting with two counter-propagating lasers. (**b**) The "Λ" type double resonance. (**c**) The "V" type double resonance. (**d**) The "Ξ" (ladder) type double resonance

3.4 Cavity-enhanced double-resonance spectroscopy

Atoms interacting with two lasers have been widely studied in experiments of coherent population trapping (CPT) [92], electromagnetically induced transparency (EIT) [93], and precision spectroscopy [94]. Molecules have additional internal degrees of freedom of rotations and vibrations, differently from atoms, circumstance that adds complexity, but also allows for more opportunities for interesting investigation. Double-resonance (DR) spectroscopy of molecules has been applied to label transitions [95], simplify congested spectra [96], and probe energy levels that are hardly accessible by single-photon transitions [97].

Usually, a fraction of molecules with a particular velocity can interact simultaneously with two lasers. We first consider a molecular transition between two levels. Taking into account the relativistic energy conservation and the momentum conservation [98], we have:

$$\omega - \omega_0 = \pm\omega\frac{v_{zi}}{c} - \omega_0\frac{v_i^2}{2c^2} + \omega_0\frac{\hbar\omega_0}{2Mc^2} + \cdots \tag{13}$$

where c is the speed of light, M is the rest mass of the molecule, $\omega/2\pi$ is the frequency of the laser, and the laser propagates along the z direction. On the right side of the equation, the first term is the first-order Doppler shift, whose sign indicates the orientation of the molecular speed along the laser propagating direction, the second term corresponds to the second-order Doppler shift, and the third term is the recoil shift. Note that the molecule changes its speed from v_{zi} to v_{zf} after absorbing a photon, and we have $v_{zf} = v_{zi} + \hbar\omega/Mc$.

There are three types of double resonances, each with two lasers either co-propagating or counter-propagating. Figure 12 shows configurations of the "Λ", "V", and "Ξ" (ladder) types of double resonances, where the requirements for double resonance can be specified [99]. For the "Λ" type DR, two transitions share the same upper state, yielding:

$$\frac{\omega_{10}}{\omega_1} - \frac{\omega_{20}}{\omega_2} - \frac{\hbar(\omega_1 - \omega_2)}{2Mc^2} = 0, \quad \text{co-propagating;} \tag{14}$$

$$\left(1 - \frac{\omega_{10}}{\omega_1}\right) + \left(1 - \frac{\omega_{20}}{\omega_2}\right) + \frac{v_i^2}{c^2} + \frac{\hbar(\omega_1 + \omega_2)}{2Mc^2} = 0, \quad \text{counter-propagating;} \tag{15}$$

where $\omega_{10}/2\pi$ and $\omega_{20}/2\pi$ are centers of the two transitions, while $\omega_1/2\pi$ and $\omega_2/2\pi$ are the two laser frequencies.

For the "V" type DR, two transitions share the same lower state, yielding:

$$\frac{\omega_{10}}{\omega_1} - \frac{\omega_{20}}{\omega_2} + \frac{\hbar(\omega_1 - \omega_2)}{2Mc^2} = 0, \quad \text{co-propagating;} \tag{16}$$

$$\left(1 - \frac{\omega_{10}}{\omega_1}\right) + \left(1 - \frac{\omega_{20}}{\omega_2}\right) + \frac{v_i^2}{c^2} - \frac{\hbar(\omega_1 + \omega_2)}{2Mc^2} = 0, \quad \text{counter-propagating.} \tag{17}$$

For the "Ξ" (ladder) type DR, the upper state of the first transition is the lower state of the second transition, yielding:

$$\frac{\omega_{10}}{\omega_1} - \frac{\omega_{20}}{\omega_2} - \frac{\hbar(\omega_1 + \omega_2)}{2Mc^2} = 0, \quad \text{co-propagating;} \tag{18}$$

$$\left(1 - \frac{\omega_{10}}{\omega_1}\right) + \left(1 - \frac{\omega_{20}}{\omega_2}\right) + \frac{v_i^2}{c^2} + \frac{\hbar(\omega_1 - \omega_2)}{2Mc^2} = 0, \quad \text{counter-propagating.} \tag{19}$$

Equations (14)–(19) apply for atomic or molecular transitions among three levels, and they could be further simplified if the second-order Doppler shift and the recoil shift could be neglected.

Since rovibrational transitions are usually weaker than electronic transitions, it is more challenging to pump enough molecules to selected vibrationally excited states and probe them with sufficient sensitivity. Multi-pass cells and optical resonant cavities have been used to increase the effective optical path length and improve the sensitivity to probe weak transitions. Recently, Karhu et al. [100, 101] employed a 3 µm cw laser to pump acetylene molecules and measured symmetric vibrational states with near-infrared cavity ring-down spectroscopy. Foltynowicz et al. [102] utilized a 3.3 µm cw pump laser and a 1.67 µm optical frequency comb to detect sub-Doppler transitions of methane. Tan et al. [103] reported a mid-infrared-near-infrared DR spectroscopy method with kHz accuracy and demonstrated by pumping $^{13}CO_2$ molecules with a 4.4 µm laser and probing the CRDS spectrum at 1.5 µm.

Two-photon precision spectroscopy based on narrow-linewidth continuous-wave lasers has been limited to strong transitions of molecules, mostly fundamental bands in the mid-infrared region. A resonant cavity can also enhance the laser power inside the cavity and allow for pumping molecules to highly excited states. Hu et al. developed comb-locked cavity-assisted double-resonance (coca-DR) spectroscopy [99, 104], where both pump and probe lasers are locked to the same high-finesse optical cavity. When the cavity length is adjusted, both frequencies tightly locked with the cavity will be tuned simultaneously. Eventually, at a particular cavity length, Eqs. (14)–(19) can be fulfilled and a DR signal is detected. All three types of DR spectra shown in Fig. 12 were demonstrated by pumping CO molecules to intermediate states in the $v = 3$ vibrational state [99]. Tens of rotational levels in a very highly vibrational state of CO_2, with 8 quanta in the CO stretching mode, were measured through a "Ξ" type DR measurement, and the upper-level energies were determined with kHz accuracy [104].

By changing the off-resonance frequency shifts of the pump and probe lasers, molecules with a specific velocity along the laser beams could be selectively excited, which could be applied to prepare velocity- and state-selected molecules in studies of molecular interactions [105]. Owing to the Doppler-free nature of DR spectroscopy, the narrow linewidth observed in this method allows for high-selectivity detection of weak transitions or trace molecular samples [106, 107], and could also be applied in testing fundamental physics/symmetry in molecules with unprecedented precision [108, 109].

This scheme of cavity-enhanced double-resonance spectroscopy, a complex two-color scheme, is different from a method of direct two-photon spectroscopy. Such a single-color approach was accomplished in a measurement of a two-photon transition in N_2O at a wavelength of 4.53 μm [110]. The sensitivity of this scheme hinges on the two-photon signal enhancement of an accidental intermediate quantum level with small detuning at the one-photon excitation energy in the molecule. Also this intermediate level should have the appropriate quantum numbers for providing enhancement. A major advantage of this approach is that it yields essentially Doppler-free spectrum, as is usual in two-photon excitation with counterpropagating beams.

4 NICE-OHMS

4.1 Characteristics of signal generation

The sensitive absorption measurement technique commonly referred to as Noise-Immune Cavity-Enhanced Optical-Heterodyne Molecular Spectroscopy (NICE-OHMS) is in fact a cavity-enhanced frequency modulation method. This technique, which reaches the highest sensitivity among the various absorbance measurement methods, was invented by Hall and coworkers in the late 90s [24, 25]. It is based on the frequency modulation absorption method, initially applied without a cavity [2], which allows for rapid comparison of on-resonant and off-resonant absorption effects. This can be achieved by modulating the laser beam and its carrier frequency to generate sidebands by an electro-optic modulator (EOM) so that either the carrier or the sidebands are resonant with the optical cavity. In frequency modulation, the phase of the laser is modulated at high frequency f_m at an amplitude represented by a modulation index β. If the carrier frequency is scanned over an absorption resonance, and the sidebands remain off-resonance, the differential absorbance (or phase shift) can be demodulated via lock-in detection. This in itself yields a strong noise-reduction effect, since the low-frequency contributions to $1/f$ white noise are strongly suppressed, and lifted to the much higher modulation frequency.

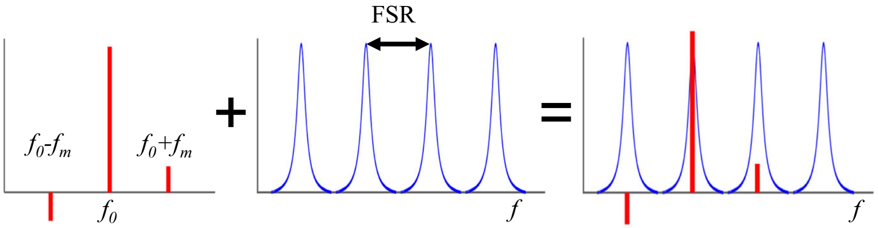

Fig. 13 Illustration of the in-coupling of a laser beam at carrier frequency f_0 and sidebands at frequencies $f_{\mathrm{SB}} = f_0 \pm f_m$ into an optical cavity. Here the sidebands generated, represented by the red vertical bars, match perfectly the FSR of the cavity, while their vertical extension indicates typical intensities, where the negative sign is indicative of the out-of-phase character of both sidebands

The NICE-OHMS technique is one of steady-state signal acquisition, while following spectral scanning. This is in contrast to CRDS where the signal excitation beam is switched on and off, and where the intensity during the transients changes. It also means that for NICE-OHMS signal integration times are fully exploited and that power-dependent effects, such as AC-Stark effects, are constant during the measurement, which allows for controlled assessment of systematic effects. Detailed analyses of NICE-OHMS signal generation were presented by the groups of Hall [111] and by the group at Umea University, which made many decisive contributions to the field [112–116].

As for equations the complex electric field combining the carrier frequency and the modulation can be written as:

$$\vec{E}^{FM}(f_c, t) = \frac{\vec{E}_0}{2} e^{i[2\pi f_c t + \beta \sin(2\pi f_m t)]}, \tag{20}$$

where $\vec{E}_0$ represents the vectorial propagation of the electric field and f_c the frequency of the carrier. This field can be expressed in terms of a series of Bessel functions $J_j(\beta)$, approximated for a low modulation index (i.e. $\beta \leq 1$):

$$\vec{E}^{\mathrm{FM}}(f_c, t) = \frac{\vec{E}_0}{2} e^{i2\pi f_c t}[J_0(\beta) + J_1(\beta)e^{i2\pi f_m t} - J_{-1}(\beta)e^{-i2\pi f_m t}], \tag{21}$$

where $J_{-1}(\beta) = -J_1(\beta)$. The propagating electric field will consist of a carrier and two sideband frequencies generated at $f_{\mathrm{sb}} = f_c \pm f_m$. All three frequencies propagate (and counter-propagate) in the cavity matched to longitudinal cavity modes (see Fig. 13).

Of importance for the signal analysis is that the sidebands are out of phase. If an optical beam at the three combined frequencies passes through a gaseous absorbing medium each component will be affected in a different manner. In particular, each component experiences a complex transmission function, where amplitude attenuation and optical phase shift will affect each of the three propagating frequencies [116]. This will ultimately lead to a complex susceptibility with dispersion and absorption terms. The absorbance signal can be extracted, via demodulation of the transmitted FM signal and detected at the frequency f_m. The FM signal when scanned over a frequency range Δf can be expressed:

$$S^{\mathrm{FM}}(\Delta f, \theta_{\mathrm{FM}}) \propto \left\{ \left[\chi^{\mathrm{disp}}(\Delta f - f_m) - 2\chi^{\mathrm{disp}}(\Delta f) + \chi^{\mathrm{disp}}(\Delta f + f_m) \right] \cos\theta_{fm} \right. \\ \left. + \chi^{\mathrm{abs}}(\Delta f - f_m) - \chi^{\mathrm{abs}}(\Delta f + f_m)] \sin\theta_{\mathrm{fm}} \right\}, \tag{22}$$

where θ_{fm} is the demodulation phase. These expressions demonstrate that the FM signal is composed of two distinct signals in quadrature, which implies that the dispersion component and absorption component have a phase shift of 90 degrees relative to each other. The dispersion phase consists of three functional terms, while the absorption phase consists of two functional terms. By phase demodulation, typically with a phase-sensitive or lock-in amplifier, either signal phase component can be individually obtained [116, 117]. High detection sensitivity is mostly due to the noise-immune principle: Residual fluctuations of the laser power and frequency will affect the transmitted carrier and sidebands exactly in the same way. As a consequence, since the sidebands are out of phase, the signal derived from the synchronous detection of the transmitted power at the FSR splitting frequency is relatively immune to these fluctuations.

4.2 Modulation schemes in NICE-OHMS

In NICE-OHMS, FM is combined with cavity enhancement, making use of the sensitivity enhancement of intracavity absorption by the factor $\pi/2F$, with F the finesse of the cavity, connected to the properties of an optical cavity via:

$$F = \frac{\mathrm{FSR}}{\Delta\nu} = \frac{c}{2L\Delta\nu} = \frac{\pi\sqrt{R}}{1-R} \tag{23}$$

where $\Delta\nu$ is the width of the cavity mode in frequency space. Here the sensitivity enhancement derives straightforwardly from the longer absorption path length inside the cavity. The frequency modulation could in principle be established by a low-frequency modulation, but in high finesse cavities, the mode bandwidth $\Delta\nu$ is extremely small (kHz range) so that the modulation scheme would not gain substantial signal-to-noise improvement. NICE-OHMS applies the solution of coupling the modulated sideband frequencies into the adjacent longitudinal modes of the cavity. Since the FSR typically measures 300–500 MHz, such high modulation frequencies lead to significant noise reduction. This marks the generic advantage of NICE-OHMS.

The concept of FM spectroscopy is based on rapid comparisons between off-resonance and on-resonant interaction with the absorbing medium, so a straightforward signal analysis relies on the assumption that the carrier frequency f_c interacts with the medium, while the sidebands at $f_{\mathrm{SB}} = f_0 \pm f_m$ do not. So for spectroscopy examples where the Doppler broadening exceeds the FSR of the cavity this becomes a limitation, even for measurement of singly isolated lines. In case of congested spectra with many overlapping lines within a frequency band corresponding to the FSR, the spectral analysis is hindered. Also, it is assumed that the single pass absorbance is

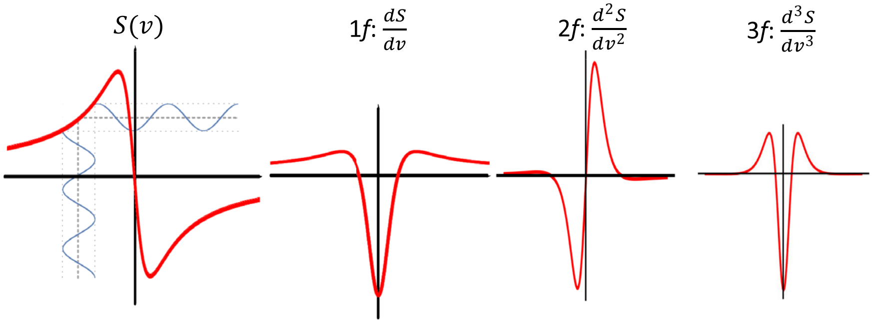

Fig. 14 Signals resulting from various demodulation schemes in wavelength-modulated NICE-OHMS. From left to right are displayed the generic NICE-OHMS signal yielding a dispersive line shape, the $1f$ demodulated signal producing a symmetric line shape, the second order derivative signal, and finally the third order derivative signal

small and limited by:

$$\alpha L << \frac{\pi}{2F}, \tag{24}$$

otherwise the shift of the cavity mode frequencies due to dispersion cannot be neglected, leading to the need for advanced analysis methods [116]. These considerations make NICE-OHMS in particular suited for the measurement of very weak transitions and for measuring narrow Lamb dips. Nevertheless, there are ample examples where NICE-OHMS has been applied to the recording of Doppler-broadened spectra.

The technique of wavelength modulation (WM) is typically added to further enhance the sensitivity of NICE-OHMS and reduce its background noise [118, 119]. By the simultaneous application of FM and WM the main noise-reducing advantages of FM are exploited in combination with enhanced absorbance over the effective length inside a cavity. The wavelength modulation, typically applied in the audio domain (with $f_{\mathrm{WM}} \approx 100$ Hz) can be implemented by dithering one of the cavity mirrors via a piezo-electric mount. This causes the capture of the carrier wave on a longitudinal mode of the cavity to be modulated. The resulting composite signal is subsequently demodulated at the WM-frequency f_{WM} on a lock-in detector, optimizing a phase. The resulting signal then yields a derivative signal of the typical NICE-OHMS, or frequency-modulated signal, which takes on a dispersive line shape. Besides improving signal-to-noise ratio this double WM-FM modulation technique bears the advantage that the $1f$-demodulated signal takes on a symmetric line shape, favorable for analyzing molecular absorption spectra. Higher orders of demodulation can be applied, leading to higher-order derivatives, and corresponding line shapes, as is shown in Fig. 14.

The function that describes the first order of demodulation of the absorbance signal will be referred to as f_{1f} and can be written as:

$$F_{1f}^{\mathrm{abs}}(f) = \frac{8\,A\,\Gamma^2(f-f_0)^2}{\left[\Gamma^2+4(f-f_0)^2\right]^2}, \tag{25}$$

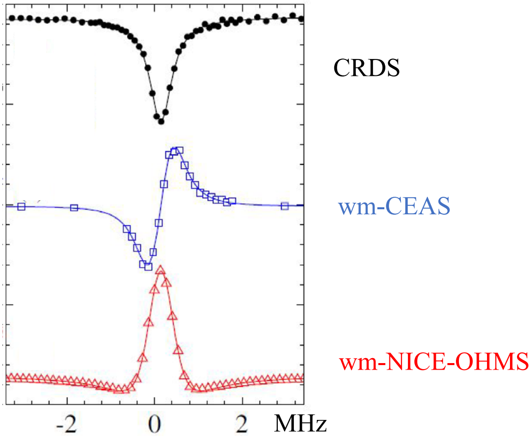

Fig. 15 Comparison of recorded spectra (in saturation) using three different techniques discussed in the present review for the R(4) line in the $\nu_1 + \nu_3$ vibrational band of C_2H_2 molecule are displayed. The wm spectra are demodulated at $1f$, both for CEAS and NICE-OHMS. The zero position along the frequency axis corresponds to the measured transition frequency, which is at 217 043 458 MHz. Results reproduced from Ref. [123]

where the adjustable parameters are the line position f_0, the line intensity A, and width Γ. This is the line shape most often recorded in NICE-OHMS spectroscopy. It is to be noted that this line shape is not Lorentzian-like but exhibits some overshoot wings above the background level. Line shapes as recorded with cavity ring-down spectroscopy (CRDS), wavelength-modulated cavity-enhanced spectroscopy (wm-CEAS) and wavelength-modulated NICE-OHMS for a single line are compared in Fig. 15.

The multiple levels of modulation and demodulation, as discussed above, make the NICE-OHMS technique the most sensitive for measuring direct absorption in the gas phase. Since the signal recovery depends on the balance between light propagation of the sidebands through the sample, where both should be off-resonance. Hence the sensitivity of the technique can be disturbed if by some means the intensity level of the sidebands is affected in a different way. This is known as residual amplitude modulation (RAM) and sets a noise floor to the limit of detection. Spurious effects of temperature and pressure fluctuations, cross-coupling between polarization axes in fibers [120], or even weak atmospheric absorptions, may cause unbalanced sideband intensities leading to an elevated noise floor. Similarly, etalon effects in the optics acting on the laser beams entering the cavity may be similarly harmful [121]. To avoid RAM effects the entire entry optics setup was mounted in a pressure and temperature-regulated box (at mK) with steady dry nitrogen flow in a recent extremely sensitive NICE-OHMS experiment where a Lamb dip of a quadrupole line of H_2 at a strength of 4.4×10^{-28} cm/molecule was detected [122].

In one of the first studies by the inventors of NICE-OHMS detection at 1.5 times the shot-noise limit was reported for detection of a Lamb dip in C_2HD [25]. Later a similar achievement of near shot-noise limited detection was reported probing a Doppler-broadened line in C_2H_2 [124]. Such shot-noise limitation expresses a figure of merit that is related to the statistics of light measured on a photodetector, where the Poissonian fluctuations also depend on the finesse of the cavity and the amount of light coupled into the cavity (the optical impedance). The latter factors also determine the detection efficiency of a NICE-OHMS setup.

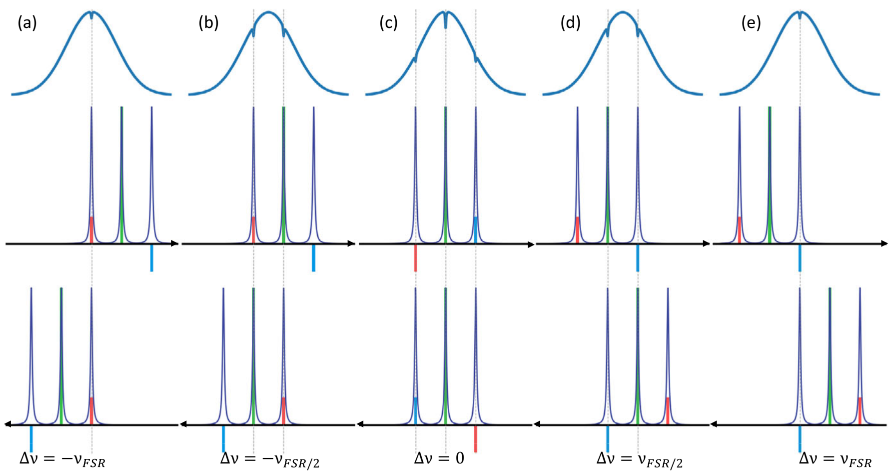

Fig. 16 Illustration of the five possible occurrences of velocity-selective saturation in a Gaussian velocity distribution by the three counter-propagating waves present in NICE-OHMS. The five panels correspond to the five possible detunings of the carrier from the resonance where a saturated Lamb-dip profile can be recorded. In the top layer, the position of the generated Lamb dips is included on the Doppler-broadened absorption profile. In the second and third layers the frequency overlaps of carrier and sidebands are indicated for producing the Lamb dips in the top layer. The second layer represents a triplet of laser beams traveling toward the right direction, whereas the third layer represents the triplet moving toward the left, hence counter-propagating. This figure is inspired by a figure in Ref. [125]. For a detailed explanation see text

4.3 Contributions to the NICE-OHMS signal

Since an optical cavity is employed in NICE-OHMS the intracavity circulating power may be very high, depending on the finesse F of the cavity. Since highly-reflective mirrors have become available in a wide wavelength range typical finesses of over 100,000 are well within reach, making intracavity excitation with kW powers possible. Under such conditions, even very weak transitions may be saturated and Lamb-dip spectroscopy can be operated. The generic form of a Lamb dip can be generated by the counter-propagating beams at the carrier frequency inside the cavity, probing molecules with longitudinal velocities of $v_z = 0$. However, in NICE-OHMS three beams at differing frequencies propagate in the cavity, and all three in both directions. This opens the possibility that different frequencies mix into a Lamb-dip scheme connecting different velocity classes of molecules involving sets with $v_z \neq 0$. Such mechanisms were described by Axner et al. [116] and they are displayed in Fig. 16. Under the presence of three counter-propagating waves, there are nine occasions at which two fields can interact with certain velocity classes and fulfill the condition of saturated resonance.

The configuration in panel (c) of Fig. 16 represents the generic production of a Lamb dip with counter-propagating beams at the carrier frequency. Two additional Lamb dips may be generated by a red sideband and a counter-propagating blue sideband from a saturation process for molecules with an effective Doppler shift of $\vec{k} \cdot \vec{v} = f_{\mathrm{FSR}}$, leading to a velocity-selective saturation dip. As follows from the figure these features

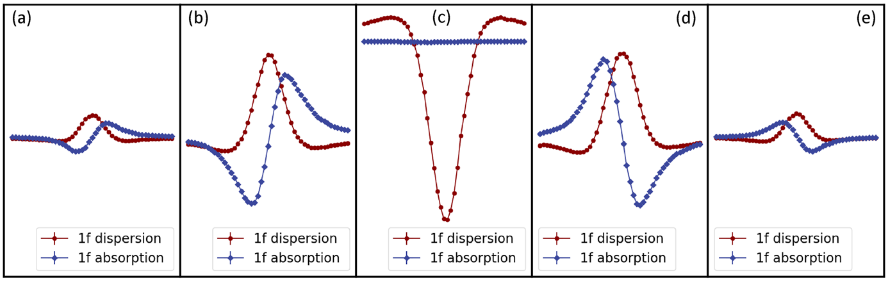

Fig. 17 Line profiles of the various NICE-OHMS signals to be obtained under saturation conditions. Displayed are the nine possible Lamb-dip features as measured for the water ($H_2{}^{16}O$) line with quantum assignment: $(200)6_{24} \leftarrow (000)5_{33}$ at a transition frequency of 218 250 754 918.9 (1.5) kHz. Indeed five different signals are recorded in the dispersive channel, and four in the absorption channel, as discussed in the main text. Figure reproduced from Ref. [117]

will only be observed under the condition that the sideband resonances are covered within the Doppler profile. These sideband-sideband dips of panel (c) are produced for laser settings where the carrier frequency matches the resonance frequency (f_0), even though the side dips are produced by molecules at $\vec{k} \cdot \vec{v} = f_{\mathrm{FSR}}$. In panels (a) and (e) resonances are shown where blue-blue and red-red sidebands from counter-propagating beams match to produce a Lamb dip at a frequency shifted by $\pm f_{\mathrm{FSR}}$ from the carrier resonance, but the signal is produced from a velocity class for which $\vec{k}\cdot\vec{v} = 0$. Finally, there are two more processes, depicted in panels (b) and (d), where the carrier wave is detuned by $\pm f_{\mathrm{FSR}}/2$ from the transition center. In this carrier-sideband scheme molecules are probed that have an effective Doppler shift of $\vec{k} \cdot \vec{v} = f_{\mathrm{FSR}}/2$.

The different signal schemes to be extracted from NICE-OHMS under saturation conditions were first uncovered in a measurement of a $P_e(11)$ transition in C_2H_2 at a wavelength of 1531.588 nm, superimposed on a Doppler-broadened profile [126]. As discussed by Axner et al. indeed only nine signals are observed in the saturated scheme, five in the dispersion phase, and four in the absorption phase. In the absorption phase, one possible signal is missing for reasons that the frequency-modulation signal is insensitive to the attenuation of the carrier, and the fact that the sidebands exhibit a phase of opposite sign, thus canceling their contribution on resonance [116].

These features of saturation signals were systematically investigated, both for the dispersion as for absorption channels on a specific spectral line in water. Results are displayed in Fig. 17. This shows again that, in the center panel (c), only the dispersion Lamb dip is detected, while the absorption feature is not present. It is interesting to note the phase differences between the left, center and right panels.

4.4 Lamb-dip reversals

The signal pertaining to panels (c) in Figs. 16 and 17 exhibit a Lamb dip reversal explored recently in the spectrum of water lines [127]. There the central Lamb dip, produced by molecules at $\vec{k} \cdot \vec{v} = 0$ derives from two contributions. Firstly, this central Lamb dip at the resonance frequency f_0, is produced by the counter-propagating carrier

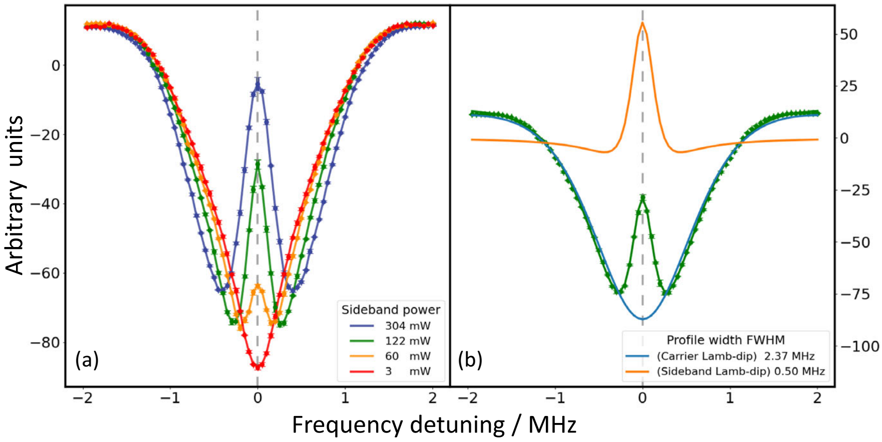

Fig. 18 Spectral recordings of NICE-OHMS signals for the $(2\,0\,0)0_{0,0} \leftarrow (0\,0\,0)1_{1,1}$ line of $H_2{}^{16}O$. Panel (a) shows the spectral profile at various sideband (SB) powers and a fixed carrier power of 15 W. The dashed marker represents the position of the line center. Panel (b) illustrates the individual components of the double-dip spectra at a sideband power of 122 mW. The orange profile corresponds to the two coincident Lamb-dips, with a FWHM of 0.5 MHz, induced by the sideband fields. The blue profile of an ordinary sign, with a FWHM of 2.4 MHz, is generated by the carrier. The combination of the orange and blue profiles leads to the recorded signal, denoted with a green curve. Figure reproduced from Ref. [127]

waves. Since these have the largest intensity this Lamb dip is the strongest saturation feature in the spectrum, and for water lines with Einstein-A coefficients > 0.1 s^{-1} these resonance Lamb dip features exhibit significant power broadening. There is a second contribution to the signal at f_0, produced by the sideband-sideband coupling at f_0. Since both sidebands have opposite phases, the contribution of this phenomenon to the signal at f_0 is reversed. In Fig. 18 an example of such an interference between a power-broadened Lamb dip and a sideband-sideband generated reversed signal is illustrated for a water line. Note that the Lamb dip reversal sets in for increasing power in the sidebands; this was accomplished by increasing the modulation index for generating the sidebands of the NICE-OHMS triplet, while keeping the power of the carrier constant.

4.5 Application of 3*f* demodulation

Typically the $1f$ demodulation of the wavelength-modulation approach is adopted since the overtone demodulations yield lower signal-to-noise ratios. But as demonstrated in Fig. 14 the linewidths in higher demodulation become narrower, and in particular the $3f$ signal is useful, because it produces symmetric line shapes. Instead of the functional form for the $1f$ signal, as in Eq. (25), an equation form for the $3f$ signal for the NICE-OHMS absorption feature can be derived:

$$F_{3f}^{\mathrm{abs}}(f) = \frac{3072\, A\, \Gamma^2 (f - f_0)^2}{\left[\Gamma^2 + 4(f - f_0)^2\right]^4} - \frac{96\, A}{\left[\Gamma^2 + 4(f - f_0)^2\right]^2}$$

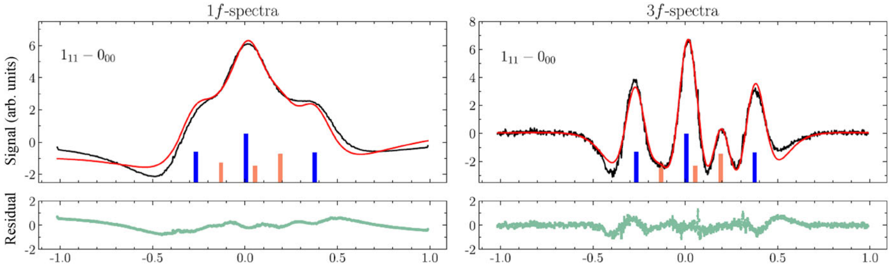

Fig. 19 Lamb-dip Spectra of the $1_{11} \leftarrow 0_{00}$ line in the (2-0) band of $H_2{}^{17}O$ molecule. Demodulation schemes for wavelength-modulated NICE-OHMS are compared with $1f$ on the left and $3f$ on the right. The tick marks, blue for generic hyperfine components and orange for cross-over resonances, indicate an expected hyperfine structure of the spectral line. This example clearly demonstrates the better resolving power of $3f$-demodulation, whereas the signal-to-noise ratio is decreased. Reproduced from Ref. [128]

indeed yielding a narrower and symmetric line profile. In Fig. 19 it is demonstrated how the improved resolving power of $3f$-demodulation can serve to better resolve the hyperfine structure in a vibrational transition of $H_2{}^{17}O$. Spectra of this kind helped deduce the hyperfine constants related to the ^{17}O nuclear spin ($I = 5/2$) and verifying *ab initio* computations thereof in the water molecule [128].

4.6 Experimental setup and locking schemes

In Fig. 20 an advanced setup for a NICE-OHMS experiment is displayed. The laser and calibration part consists of an external cavity diode laser (ECDL) and an optical frequency comb (OFC) laser which is referenced to an atomic Cs clock. Electronic schemes are in place to impose the long-term stability of the OFC to the optical cavity, while that cavity delivers short-term stability to the laser system. Frequency modulation is accomplished by an electro-optic modulator (EOM) to generate the sideband frequencies (f_{FSR} for the NICE-OHMS process, and at a lower frequency ($f_{\mathrm{PDH}} \approx 20$ MHz) for Pound–Drever–Hall locking of the laser to the cavity. The PDH scheme is extended to a DeVoe–Brewer scheme [130] whereby the absolute frequency of the laser is locked to a cavity mode, and simultaneously locked to the cavity-mode spacing, equalling FSR $= c/2L$, with a radio frequency produced in the EOM. Wavelength modulation (at typically $f_{\mathrm{dith}} \approx 400$ Hz) is imposed via a piezo-electric transducer on which one of the mirrors is mounted. Frequencies are calibrated by measuring beat notes between the ECDL-spectroscopy laser and the modes of the OFC. A high-fidelity lock-in amplifier (Zurich Instruments) is used for demodulating the signals and extracting the spectra.

4.7 Examples of NICE-OHMS experiments

A number of experiments dealing with the optical technology of NICE-OHMS and its application in spectroscopy have been performed, this less widespread application domain is probably related to the much more complex experimental configuration

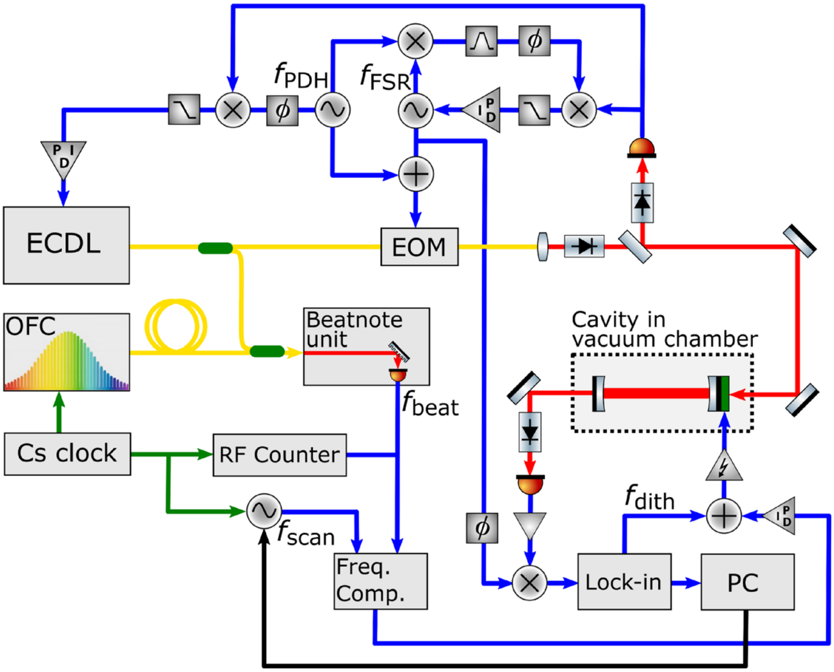

Fig. 20 Configuration of an advanced setup to perform NICE-OHMS experiments. For details see main text. Reprinted (Fig. 1) with permission from [129], Copyright (2018) by the American Physical Society

required for NICE-OHMS, with triple modulation/demodulation schemes and the multiple Lamb-dip signals observed. Moreover, NICE-OHMS does not allow for large tuning ranges covering full molecular absorption bands, due to the fact that the interrogated spectral interval should fall within the capture range of the locking loop that exactly matches the modulation frequency with the cavity FSR. For light molecules with rather broad Doppler profiles, and for large molecules with congested rotational bands this is a bottleneck.

Different laser systems, covering various wavelength ranges, have been combined with the NICE-OHMS technique. Originally, in the first demonstration, the non-tunable Nd:YAG laser was employed [24, 25], and later Titanium–Sapphire lasers [111], external-cavity diode lasers [23, 131], DFB diode lasers [132], quantum cascade lasers [133], fiber lasers [134, 135], difference-frequency [136] and optical parametric devices [137].

The optical detection technique of NICE-OHMS was further developed in several directions, in optimizing the modulation index [138], focusing on saturation effects on the line shapes in the application of Doppler-broadened NICE-OHMS [139], and investigating the effects of the cavity finesse on NICE-OHMS signals [140]. The development of NICE-OHMS in combination with optical frequency comb spectroscopy, leading to a sensitive technique for high-resolution broadband molecular detection is a highlight to be mentioned [141].

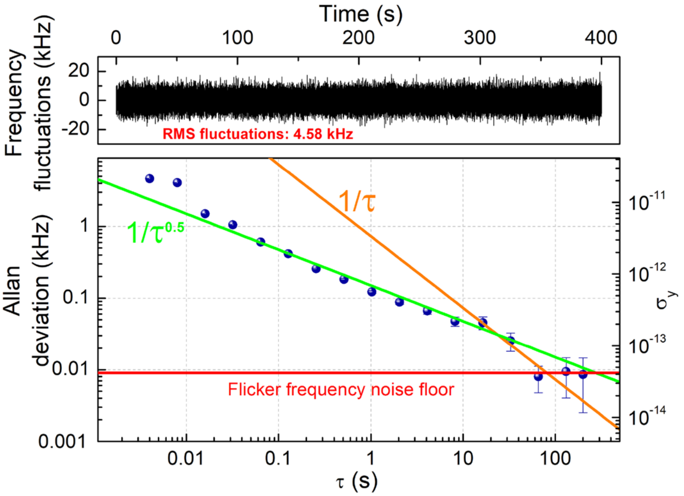

Fig. 21 Plot of measured the residual frequency fluctuations (top) and Allan deviation (bottom) of the external cavity diode laser at 1.39 µm for a locking scheme via a NICE-OHMS signal to a Lamb dip in $H_2^{18}O$. The in-loop relative stability (σ_y) is $\sim 5 \times 10^{-13}$ for an integration time of 1 s. Reprinted with permission from [149], Copyright (2014) Optical Society of America

The NICE-OHMS technique was applied in general spectroscopic studies focusing on breath analysis [142] and on quantitative trace gas detection [126]. Specific spectroscopic studies were carried out on a number of molecules, such as methane (CH_4) in the infrared at 3.4 µm [143], ammonia (NH_3) in the telecom range [144], the hydroperoxyl radical (HO_2) at 1.2 µm [145], nitrous oxide (N_2O) at 1.2 µm [146], and high-precision (sub-kHz) spectroscopy of N_2^+ ions [147]. In Sect. 5 the spectroscopic applications of various cavity-enhanced techniques on the benchmark molecules water (H_2O), acetylene (C_2H_2) and carbon dioxide (CO_2) will be highlighted.

4.8 NICE-OHMS operated as an optical clock

The sensitivity of the NICE-OHMS detection technique could be converted into a molecular clock on an R(14) transition in the 3ν vibrational band of $^{12}C^{16}O$ at 1563.618 nm. Stabilization of the cavity resonance could be achieved with an Allan deviation of 1.8×10^{-12} at 1 s, which was demonstrated to improve to 3.5×10^{-14} at 1000 s [148]. This transition in carbon monoxide, conveniently in the telecom wavelength range, and rather insensitive to magnetic fields, undergoes a pressure shift of only 1.6 kHz/Pa.

An approach, locking via a NICE-OHMS scheme to a Lamb-dip resonance at 1.39 µm to a line of $H_2^{18}O$, avoiding interference by atmospheric water signals outside the cavity [149], resulted in an absolute frequency stabilization with an Allan deviation of 5×10^{-13} at 1 s. For a graphical display see Fig. 21. At longer integration times a noise floor of 4×10^{-14} was reached after a minute. An advantage of the NICE-OHMS scheme for absolute frequency stabilization is that it is not sensitive to the exact setting of the phase in the demodulation process [149]. In other words, an incorrect setting of the phase would affect only the size of the signal without perturbing the symmetry of the dispersion-like profile. This important characteristic, which is maintained as long as the degree of saturation induced by the two sidebands is much smaller than the one induced by the carrier, reduces the risk of locking out of the line center. In addition, frequency fluctuations of the optical frequency standard at 1.39 μm could be measured by using the fringe-side transmission of a high finesse optical resonator. A careful analysis of the frequency-noise power spectral density yielded a linewidth (FWHM) of the optical frequency standard of about 7 kHz for an observation time of 1 ms, as shown in Ref. [150].

Improvement of operating conditions, such as lowering the temperature and enlarging beam diameters for reducing transit-time broadening effects, and exploring different molecular species should well lead to even higher stabilities. Even though stabilities currently reached by advanced Al^+ and Yb^+ ion clocks and Sr-lattice clocks lie outside the possible perspectives, the small and elegant technology of near-infrared molecular clocks reaching 10^{-16} stabilities would find widespread application in industry and society. An atmospheric lidar system with laser frequency stabilization based on a sub-Doppler NICE-OHMS signal has been discussed as a potential application [151].

5 Examples of cavity enhanced spectroscopic studies of molecules

5.1 Water

The water molecule qualifies as one of the most investigated gas phase species in spectroscopy. This is likely due to its major importance in atmospheric physics, astrophysics, chemistry, and combustion physics, while it is also regarded as the template for an asymmetric quantum mechanical rotor system. Hundreds of papers have been published on the line spectrum of rovibrational transitions in the electronic ground state of water, the resulting level structure, and the fitting of effective Hamiltonians describing its quantized motions.

Some of the information is condensed in the HITRAN database where it is considered as the number one molecule, and over 300,000 water lines are documented [153]. Over a time span of the past century 200,000 rovibrational lines of the main $H_2^{16}O$ isotopologue have been measured, connecting some 20,000 quantum levels. Most of the work has focused on measuring Doppler-broadened lines, where the technique of Fourier-transform spectroscopy is featured as the main tool (see e.g. Ref. [154]). Cavity-enhanced measurements performed under Doppler-broadened conditions also contributed to the large databases for water (see e.g. Ref. [155]). Very weak transitions in water, at line strengths of 10^{-29} cm/molecule, could be detected [156]. Beyond the wealth of data acquired through measurement of dipole transitions recently the detection sensitivity of CRDS was favorably applied to detect quadrupole lines in water [157].

The advances of the cavity-enhanced techniques opened the possibilities of measuring Doppler-free spectra of rovibrational transitions, pursued by several groups [79, 158, 159]. NICE-OHMS experiments were performed on water in combination with

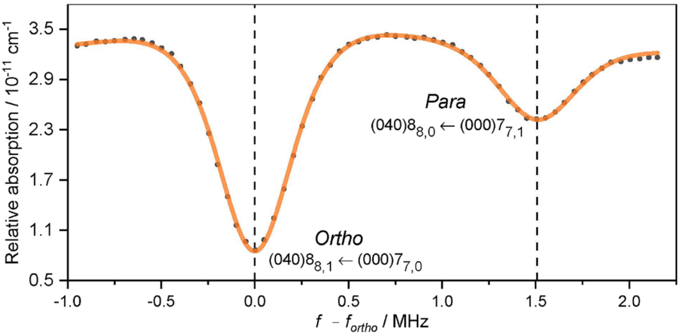

Fig. 22 NICE-OHMS spectrum of the (040)$8_{8,1/0}$ ← (000)$7_{7,0/1}$ doublet. The scanning frequency, f, is shifted with the line position of the *ortho* transition, $f_{ortho} = 218\,444\,703.636$ MHz (separated by 1.5 MHz from the *para* line). Figure reproduced from Ref. [152]

a spectroscopic network approach. These studies resulted in the measurement of sets of Lamb dips for $H_2{}^{16}O$ [127, 152] and $H_2^{18}O$ [160] at an accuracy well below 10 kHz. An example of an experimental result is shown in Fig. 22, where two close-lying lines ((040)$8_{8,0/1}$ and (040)$7_{7,0/1}$ pertaining to an *ortho-para* doublet are resolved as separate Lamb dips. The network approach, to be considered as a generalized Ritz principle, allows for verifying the internal consistency of the precision measurements by constructing cycles of multiple rovibrational transitions at a level that would not be possible by comparing to effective Hamiltonians. All quantum levels, for which the level energy has been verified and secured, can then be included in a network path even leading to high rotational quantum numbers. In Fig. 23 two of such paths are built, one for the *para*-species and one for the *ortho*-species of $H_2{}^{16}O$, ultimately leading to quantum levels $J_{K_a,K_c} = 7_{7,1}$ and $8_{8,0}$ on the *para*-side and $7_{7,0}$ and $8_{8,1}$ on the *ortho*-side. These measured paths involve rovibrational transitions, all originating in the $(v_1 v_2 v_3)$=(000) ground state and exciting various vibrational levels in the P4-polyad in water with levels: (040), (021), (200), (101) and (002) indicated with color code in Fig. 23. In the separate paths for the *para* and *ortho* species, that cannot be interconnected since no *para-ortho* transitions have been detected [161], some purely rotational transitions are included. These transitions, measured to high accuracy via microwave spectroscopy [162, 163] connect quantum states of positive and negative parity, that cannot be connected via rovibrational transitions.

The high-accuracy measurements on water lines, obtained with a comb-locked NICE-OHMS scheme and guided by the network approach, resulted in an accurate list of level energies. For the (000) vibrational ground state these levels can be fitted to an effective Hamiltonian, for which a 14-th order Watson-type Hamiltonian description is required to match the experimental accuracy. This treatment yields a value for the splitting of the energy between the lowest *ortho* and *para* levels. The same *ortho-para* splitting can also be determined form a calculation of the tiny splittings at the end of the paths indicated in Fig. 23. Splittings for (040)$8_{8,0/1}$ and (040)$7_{7,0/1}$ levels can be derived from nuclear-motion (GENIUSH) computations [164, 165], where the absolute uncertainties for the splittings are minute at the high J levels reached.

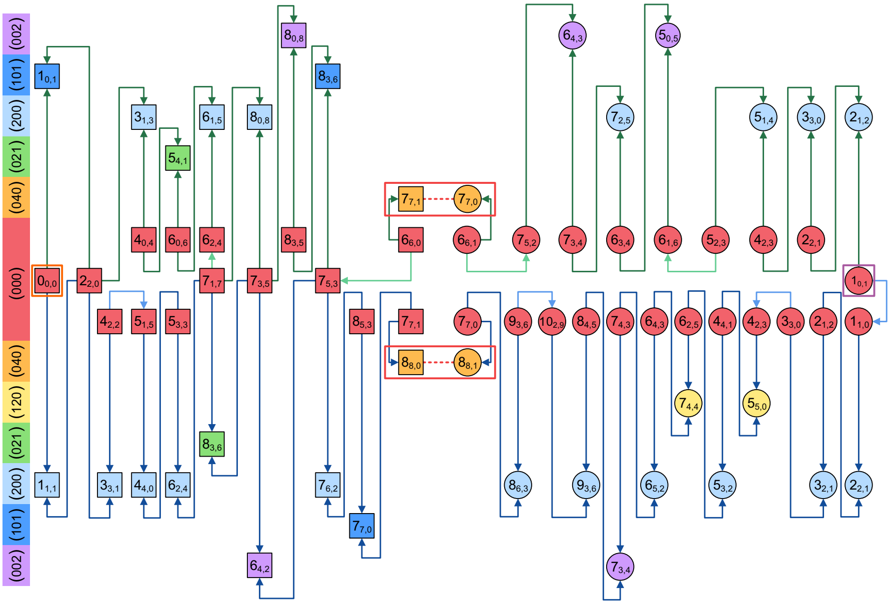

Fig. 23 The spectroscopic network was employed to determine an accurate value for the *para*-*ortho*-splitting in $H_2{}^{16}O$. The J_{K_a,K_c} rotational labels are indicated individually for each rovibrational state, while the $(v_1 v_2 v_3)$ vibrational assignments are marked in the left-side color legend. Squares refer to *para* energy levels, and circles to *ortho* levels. The paths in the *para* and *ortho* subsections end at high J levels (orange), where level separations between *para* and *ortho* become very small and can be accessed to kHz accuracy from ab initio calculations

The methods of an effective Hamiltonian for the (000) levels and the direct network approach yield a similar accuracy for the *ortho*-*para* splitting in the ground state at 23.794 361 22 (25) cm^{-1}. The latter result forms a great improvement with respect to previous determinations.

By adding two sets of accurately measured Lamb-dip lines in $H_2{}^{16}O$, all recorded in the wavenumber range 7000–7350 cm^{-1} (156 lines [152] plus 56 lines [127]), the complete J_{K_a,K_c} rotational manifold of the (200) vibrational level up to $J = 6$, could be determined to few-kHz accuracy. An advantage of the spectroscopic network approach is that based on a limited set of measurements, the high absolute accuracy can be extrapolated to other wavenumber ranges. In the case of $H_2{}^{16}O$ the measurements in the range 7000–7350 cm^{-1}, augmented with some rotational lines in the range 0–20 cm^{-1}, allow for predictions of large numbers of transitions for the ranges 0–1000 cm^{-1} and 6200–8100 cm^{-1}, as was demonstrated [127].

A similar study was performed for the $H_2^{18}O$ isotopologue [160]. An amount of 196 Lamb dips were measured with NICE-OHMS in the range 7000–7350 cm^{-1}, carefully selected for a spectroscopic network and verified for their accuracy and assignment through cycles in the network. This allowed for a determination of all J_{K_a,K_c} rotational levels up to $J = 8$, a determination of the *ortho*-*para* splitting at 23.754 904 61 (19) cm^{-1}, and the predictive computation of a high-accuracy linelist of over 1500 transitions in the ranges 0–1250 cm^{-1} and 5900-8380 cm^{-1}.

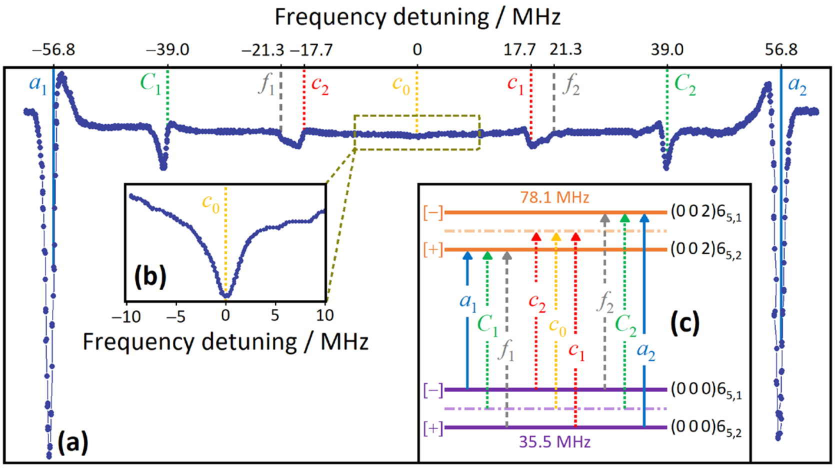

Fig. 24 Lamb-dip spectrum involving transitions between $(0\,0\,2)6_{5,2/1}$ and $(0\,0\,0)6_{5,1/2}$ levels in HDO. Panel (**a**) displays a recording of ±60 MHz with two strong dipole-allowed transitions, denoted with a, and several extra lines induced by parity-mixing, denoted with f, and lines due to crossover resonances, denoted with c. Panel (**b**) was measured at higher intracavity power. In panel (**c**) the origin of the extra lines in HDO is shown, based on cross-over resonances and parity-mixing. For further information, see the text. Reprinted with permission from [166], Copyright (2022) Optica Publishing Group

Similar highly accurate NICE-OHMS experiments were pursued for the $HD^{16}O$ isotopologue of water [166]. It was found that for quantum numbers $K_a > 3$ asymmetric line profiles were observed, and for even larger K_a values multiple spectroscopic components occurred. These effects were ascribed to the fact that for higher K_a-values the splittings between corresponding quantum levels with K_c-values differing by 1 become small. The latter is true for all water isotopologues, but the difference between HDO and the previously investigated $H_2^{16}O$ and $H_2^{18}O$ is that in the symmetric isotopologues levels with $\Delta K_c = 1$ exhibit opposing parity but fall in distinct *para-ortho* categories.

In HDO however, no *para-ortho* distinction exists, and the levels with $\Delta K_c = 1$ only have opposite parity. The intense intracavity light field couples such levels of opposite parity via an (AC)-Stark effect in particular when the level splitting between adjacent K_c levels is small. That parity mixing is at the origin of the observed perturbed structures and the occurrence of multiple lines. In addition to an allowed doublet of lines between (±) in the ground state and (∓) in the excited state, the laser-power induced parity-mixing effect then induces extra lines between (+) and (-) components. Such lines remain fully forbidden in $H_2^{16}O$ and $H_2^{18}O$ because the levels of opposite parity are also part of different *para-ortho* categories.

There is a second mechanism playing a role in producing extra resonances in the non-linear spectroscopy of HDO. If two nearby levels are optically connected to an excited level then cross-over resonances may occur, whereby the energy splitting is bridged by probing different velocity classes within the Doppler profile. In Fig. 24 an example of a complex multiline spectrum is displayed showing two allowed transitions between $(0\,0\,2)6_{5,2/1}$ and $(0\,0\,0)6_{5,1/2}$ levels in HDO. The location of all resonances, induced by parity-mixing and by crossovers can be quantitatively explained.

5.2 Acetylene

Acetylene (C_2H_2), a benchmark molecule for precision molecular studies, was investigated throughout the years with cavity ring-down spectroscopy [167], NICE-OHMS [111], interrogated by cavity-enhanced spectroscopy [168, 169], and again via frequency metrology NICE-OHMS and CRDS studies at 789 nm [170] and at 1.4 μm [171, 172]. C_2H_2 is a linear, centrosymmetric, nonpolar molecule whose infrared spectrum is of special interest in many research fields, including fundamental metrology [173, 174], combustion science [175], biomedicine [176], astrophysics and planetary science [177, 178]. It is useful to remind that, like for the water molecule, since the hydrogen nucleus is a fermion with a nuclear spin of 1/2, C_2H_2 has two nuclear-spin isomers, traditionally called *para* and *ortho*.

In 2018, Chubb et al. published a MARVEL (Measured Active Rotational-Vibrational Energy Levels) analysis of the experimentally measured and assigned rovibrational transitions of $^{12}C_2H_2$ available at that time [179]. MARVEL is an algorithm that inverts the information contained in a large number of transition frequencies, after a critical evaluation of their uncertainties [180]. Data inversion through a weighted least-squares-type procedure results in MARVEL energy levels and associated uncertainties. The MARVEL analysis of Ref. [179] produced 5200 *para* and 6013 *ortho* empirical rovibrational energy levels for $^{12}C_2H_2$, with associated uncertainties. This study has been recently enriched with new metrology-grade data resulting from CL-FS-CRDS and CL-CEAS experiments under the saturated absorption regime [169, 171, 172, 181, 182]. More specifically, twenty lines in the P, Q, and R branches of the weak $\nu_1 + \nu_3 + \nu_4^1$ combination band, in the spectral window around 1.4 μm, were carefully selected using the theory of spectroscopic networks, ensuring that a large number of transitions, measured previously by precision-spectroscopy investigations, could be connected to the *para* and *ortho* energy levels of the twenty $^{12}C_2H_2$ lines [172]. The absolute center frequencies of these lines were measured using an upgraded version of the CL-FS-CRDS apparatus of Fig. 9, expressly designed for extensive Lamb-dip investigations. The main elements of novelty with respect to the spectrometer of Ref. [82] were: (i) the operation of just one ECDL locked to a self-referenced OFCS; (ii) the extensive use of fiber optic components and devices to make the spectrometer more compact; (iii) the use of a fiber-coupled booster optical amplifier to increase the incident power and, consequently, the achievable signal-to-noise ratio. An example Lamb-dip spectrum is shown in Fig. 25, as recorded in the weak saturation regime, the saturation intensity being $\sim 10^8$ W/m^2. The experimental strategy involved a large number of spectral acquisitions as a function of the gas pressure, in the range of 0.5–3 Pa, followed by a linear extrapolation of the zero-pressure center frequency. The combined uncertainty of the measured line positions resulted to be ~15 kHz with a 2-σ confidence level.

After the application of the MARVEL procedure, 82 and 80 ultraprecise empirical rovibrational energy levels were determined in the *para* and *ortho* principal components of the spectroscopic network. Based on these energies, a rovibrational line list for $^{12}C_2H_2$ was generated. Called TenkHz, the line list contains 282 entries in the spectral range from 5898.97 to 7258.87 cm^{-1}, with a frequency accuracy better than

Fig. 25 Example of Lamb-dip $^{12}C_2H_2$ spectrum as recorded in Caserta using a comb-locked cavity ring-down spectrometer. The ring-down cavity is filled with a pure C_2H_2 sample at a pressure of 0.3 Pa. The line profile is well reproduced by a Lorentzian function

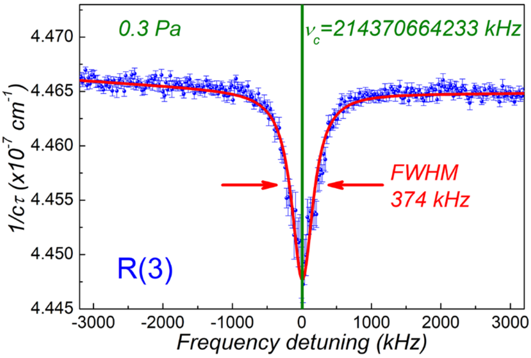

10 kHz [172]. A remarkable result of this study is that the new line list contains 35 lines that are missing from the HITRAN2020 database [153].

5.3 Carbon dioxide

The application of cavity-enhanced spectroscopy to carbon dioxide has yielded interesting results for both fundamental and applied physics. The experiments carried out in the last decade can be classified into five main categories: (i) line position studies and frequency metrology; (ii) temperature metrology; (iii) high-quality line intensity determinations; (iv) radiocarbon dating; (v) test of the symmetrization postulate of quantum mechanics. As for the first two points, we have already provided a few examples in Sect. 3 [77, 88, 91]. Here we focus on the latter ones.

Carbon dioxide is the most important anthropogenic greenhouse gas, whose growing concentration in the atmosphere is affecting the Earth's climate. Several satellite missions, such as the NASA OCO-2 and OCO-3 missions (OCO standing for Orbiting Carbon Observatory), as well as ground-based networks, like TCCON (Total Carbon Column Observing Network), are dedicated to measurements of the column-averaged CO_2 densities and mole fractions in the Earth's atmosphere, with a target precision in the range 0.3–0.5%. These sensing activities probe CO_2 vibration-rotation spectra in the near-infrared region. The accuracy of the retrieved data depends on the quality of spectroscopic parameters that are available, with special regard to line intensities, for a large number of components of the CO_2 vibrational bands near 1.6 and 2.0 μm. The data available until a few years ago did not meet the need for accuracy. A solution to the problem of CO_2 line intensities was found only recently by using ab initio quantum mechanical calculations tested against laboratory measurements at unprecedentedly high accuracy. Experimental values, as obtained by means of the FS-CRDS technique for 27 rovibrational transitions in the wavenumber region 6200–6258 cm^{-1} (near 1.6 μm), demonstrated that the theoretical model is capable of reproducing line intensities of $^{12}CO_2$ with a combined uncertainty of about 0.3% [183]. Similar results were obtained for a few CO_2 lines near 2 μm [184]. More recently, extensive data have been produced for a series of CO_2 bands at $\sim$1.6 μm using FS-CRDS and FARS-CRDS, achieving relative combined uncertainties less than 0.1% [185].

A striking example of high sensitivity achievable with CRDS techniques comes from the application to the measurement of radiocarbon abundance. Radioactive carbon (^{14}C or radiocarbon), with a half-life of 5700 years, represents an ideal natural tracer enabling to distinguish "old" fossil carbon from "young" carbon. It is well known that anthropogenic-related emissions alter the concentration of atmospheric greenhouse gases mostly through the combustion of fossil fuels. Since CO_2 derived from fossil sources is depleted of ^{14}C, the measurement of the atmospheric abundance of $^{14}CO_2$ represents a powerful tool to quantify fossil-fuel CO_2 emissions and separate them from the total biogenic and anthropogenic CO_2. Accelerator mass spectrometry is the technique of choice for high-precision measurements of radiocarbon, being characterized by a detection sensitivity at the level of parts-per-quadrillion (ppq, parts in 10^{-15}). Thanks to the impressive developments in CRDS techniques, laser spectroscopy has recently emerged as a relatively simple, robust, and cost-effective bench-top alternative. In 2011, saturated-absorption cavity ring-down (SCAR) spectroscopy enabled for optical detection of $^{14}CO_2$ in natural abundance gaseous samples, for the first time [186]. The spectrometer employed a comb-referenced high-power mid-infrared coherent radiation at 4.5 µm, as delivered by a difference-frequency-generation process inside a Ti:Sapphire laser cavity [187]. A few years later, the SCAR spectrometer was upgraded and greatly simplified by replacing the bulky laser source with a pair of quantum cascade lasers (QCLs), one of which being frequency stabilized against a sub-Doppler molecular line. As a result, the limit of detection was pushed to extreme levels, down to a few ppq, which corresponds to a minimum absorption coefficient of $\sim 10^{-11}$ cm^{-1} [42]. Such a value for $\alpha_{\min}$ is far from those of the best CRDS implementations in the near-infrared, due to the worse noise features of the detectors in the mid-infrared. This does not prevent the achievement of ultra-low limits of detection because of the much larger line intensities characterizing the CO_2 spectrum in the mid-infrared region. The difference between SCAR spectroscopy from conventional CRDS is that ring-down events are observed in the regime of saturated absorption. More specifically, the saturation effect for the molecular transition of interest induces a deviation of the ring-down signal from the perfectly exponential behavior, which is normally observed in the linear intracavity absorption regime. This is due to a time-dependent absorption coefficient given by [186]:

$$\alpha(t, \nu - \nu_0) = \frac{\alpha_0 g(\nu - \nu_0)}{1 + \frac{I_c(t)}{I_s} g(\nu - \nu_0)}, \tag{26}$$

where α_0 is the nonsaturated absorption coefficient at the resonance frequency, ν_0, $g(\nu - \nu_0)$ is the lineshape function normalized to 1 on the peak, $I_c(t)$ and I_s are the intracavity and saturation intensities, respectively. Taking into account the transient effects due to a decreasing saturation degree through the use of a proper theoretical model, it is possible to retrieve from a single decay event both the empty-cavity and the gas-induced losses [188]. After the pioneering work of 2011, many other experiments of optical detection of $^{14}CO_2$ have been performed using mid-infrared cavity ring-down spectroscopy in the linear absorption regime [189–191] and also by two-photon absorption spectroscopy [106, 107]. Currently, radiocarbon optical spectrometers are

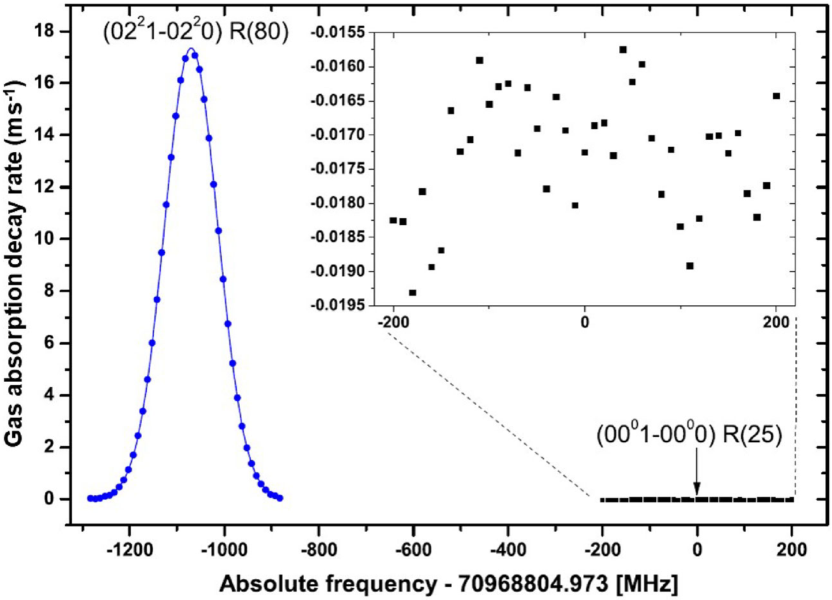

Fig. 26 Recording of the frequency interval, where a forbidden R(25) line is predicted next to the allowed R(80) transition. In the inset, the noise floor of the R(25) location is expanded, from which a constraint on the symmetrization principle is derived. Note that the two lines pertain to different vibrational bends exhibiting different strengths. Reprinted (Fig. 1) with permission from [193], Copyright (2015) by the American Physical Society

leaving the research laboratory stage and are being used for the first applications, such as the precise determination of ^{14}C in radioactive nuclear decommissioning wastes [192].

Finally, sensitive measurements employing cavity-enhanced spectroscopic techniques to the carbon dioxide molecule, have opened a testground for fundamental physics. The symmetrization postulate of quantum mechanics rules that a molecular wave function under permutation of two nuclei obeying Bose–Einstein statistics should be symmetric. As a consequence, quantum states with odd rotational angular momentum in the ground vibrational and electronic states of CO_2 cannot exist. Population in such forbidden quantum states can in principle be probed, as transitions originating in these states are not forbidden by selection rules. Moreover, the frequencies of those lines for which ground state population is forbidden are known at extreme accuracy, via the frequencies of the allowed lines. Tests of the symmetrization postulate and of the spin-statistics connection were carried out by measuring the noise floor of the R(25) line in the (00^01)–(00^00) vibrational band at 4.25 μm in comparison to a strong(er) absorption line (see Fig. 26). Via the technique of saturated absorption cavity ring-down spectroscopy an upper limit to a possible symmetry violation of 3.8×10^{-12} was established [193], which is currently the tightest constraint, superseding a previous measurement of absorption in a White cell configuration [194]. Less accurate studies were performed on tests of the symmetrization principle targeting the O_2 molecule, where quantum states of even rotational quantum numbers in the electronic ground state cannot be populated. Constraints were obtained via pulsed-CRDS [195] and via NICE-OHMS [23], in the near-infrared.

6 Testing QED with CEAS of molecular hydrogen

6.1 Rovibrational spectroscopy

The hydrogen molecule is the simplest neutral molecule consisting of two electrons and two nuclei. Since the work of Heitler and London a century ago [196], the calculation of the energy levels of the hydrogen molecule has been continuously improved. Pachucki and his colleagues used the nonadiabatic perturbation theory (NAPT) to calculate the rovibrational state energies of H_2 in the electronic ground state [197–202]. The energies were expanded in powers of the fine structure constant α [203],

$$E(\alpha) = \alpha^2 E^{(2)} + \alpha^4 E^{(4)} + \alpha^5 E^{(5)} + \alpha^6 E^{(6)} + \alpha^7 E^{(7)} + \cdots \tag{27}$$

where the non-relativistic energy $E^{(2)}$ has been calculated very accurately (10^{-8} cm^{-1}) [204]. The leading relativistic correction term $E^{(4)}$ has also been calculated to a precision below 10^{-6} cm^{-1} [201]. For higher order terms starting from $E^{(5)}$, known as the quantum electrodynamics corrections, currently uncertainties in the theoretical values are at the 10^{-4} cm^{-1} level [205, 206], but accuracy at the 10^{-6} cm^{-1} level is considered [207, 208] to be feasible in the near future. Therefore, precision spectroscopy of the hydrogen molecular isotopologues has become one of the ideal testing grounds of the QED theory of molecules, where the dissociation energy acts as a benchmark. Recent measurements of D_0 values are in agreement with theory at the accuracy level of 1 MHz for H_2 [209], D_2 [210] and HD [211]. The results of the advanced ab initio calculations of level energies and transition frequencies for the hydrogen molecular isotopologues have been made available through a program suite [212], where it should be realized that various levels and transitions are computed at differing levels of sophistication, and therewith accuracy. There is a perspective for determining values of fundamental physical constants from hydrogen spectroscopy [181, 208, 213] and for probing physics beyond the Standard Model [214, 215]. This forms a motivation for the continued efforts to improve accuracy.

The rovibrational manifolds in the electronic ground state of the hydrogen molecules form, in principle, a better target for testing theory, since those states are long-lived and transitions allow for extreme precision, in contrast to approaches where electronic transitions are probed. However, it is very challenging to detect rovibrational spectra of H_2 since in the homonuclear species no electric dipole transitions (E1) in the electronic ground state are allowed, but only extremely weak electric quadrupole moment transitions (E2). The strongest E2 transition of H_2 in the infrared region has an intensity below 1×10^{-26} cm/molecule, which is weaker than a strong water line in the fundamental band by almost eight orders of magnitude. Figure 27 shows the vibrational transitions of H_2, D_2, and HD below their dissociation limit as calculated from available spectroscopic information. Herzberg was the first to measure quadrupole transitions of H_2 near 0.8 μm in the laboratory [216] using a 22-m-long

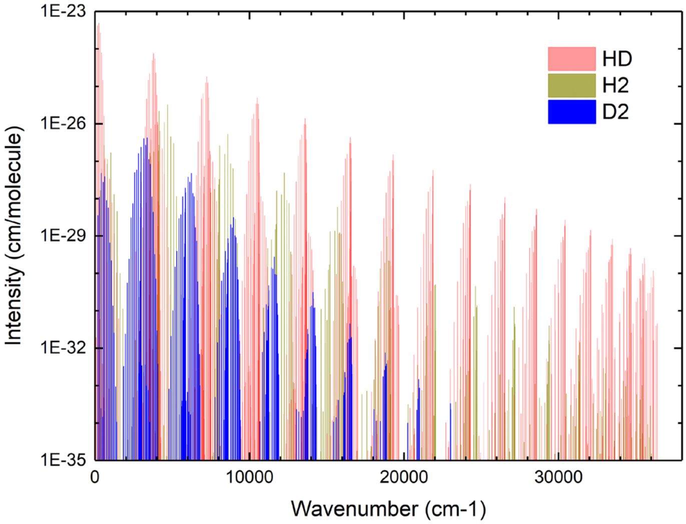

Fig. 27 Calculated rovibrational transitions of H_2, D_2 and HD below the dissociation limit. Reproduced from Refs. [220–222]

sample cell containing hydrogen gas with pressures as high as 10 atm. Extended experimental data of the infrared bands of the hydrogen molecule were obtained based on multi-pass cells [217–219]. Due to the weakness of the transitions, the accuracy of experimental data was worse than the theoretical results. This situation continued until the advent of cavity-based absorption spectroscopic techniques.

CRDS measurements of overtone quadrupole bands of H_2 were carried out by the Grenoble group [220], the NIST-Gaithersburg group [223], and the Hefei group [224, 225]. The S(3) ($v = 3 \leftarrow 0$) line position was determined [224] with an accuracy of 1.6 MHz, corresponding to a fractional uncertainty of 4×10^{-9}. Rovibrational transitions of the symmetric isotopologue, D_2, were also measured, including the fundamental ($v = 1 \leftarrow 0$) band [226, 227], and the first overtone $v = 2 \leftarrow 0$ band [221, 228, 229]. Frequencies of several D_2 lines were recently determined at sub-MHz accuracy [230]. Some very weak transitions of the hydrogen molecule have been measured by CRDS. The Hefei group measured the $S_3(5)$ ($v = 3 \leftarrow 0$, $J = 7 \leftarrow 5$) transition with a strength of 9.2×10^{-31} cm/molecule, and the Grenoble group reported the S(8) line in the $v = 2 \leftarrow 0$ band of D_2 with a strength of 1.9×10^{-31} cm/molecule. These are among the weakest transitions observed so far by absorption spectroscopy, where the implementation of cavity enhancement has been decisive.

The heteronuclear isotopologue of the hydrogen molecule, HD, has a small electric dipole moment due to the mass difference between the proton and the deuteron that causes inversion symmetry breaking in conjunction with the breakdown of the Born–Oppenheimer approximation [231]. As a result, the HD molecule exhibits weak electric dipole transitions among its vibration-rotation energy levels, with the selection rule of $\Delta J = \pm 1$, in addition to the electric quadrupole transitions of $\Delta J = 0, \pm 2$. The intensity of the strongest electric dipole line of HD in the fundamental band is about

100 times that of the quadrupole lines in the fundamental band of H_2. Herzberg and colleagues measured tens of dipole transitions of HD from the fundamental to overtone bands up to $v = 4$ since the 1950s using grating spectroscopy [232, 233]. McKellar and colleagues [234, 235] extended the measurements with Fourier-transform spectroscopy and reached the highest overtone of $v = 6$. A pure rotational transition of R(0) was also measured by Drouin et al. [236]. In the past decade, Doppler-broadened infrared HD lines have been extensively studied using CRDS techniques for the fundamental band [222] near 2.3 μm and the first overtone band [84, 237–239] near 1.4 μm.

Tritium-bearing isotopologues are of particular interest to test the calculation of molecular hydrogen for the large mass difference between tritium and hydrogen. However, the radioactivity of tritium ($t_{1/2} \simeq 12$ year) imposes considerable difficulties on the instrumentation and spectroscopic measurements. Coherent anti-Stokes Raman spectroscopy (CARS) of T_2, HT, and DT could be performed with sealed sample cells in a collaborative effort between the Tritium Laboratory Karlsruhe and the Amsterdam group [240–242]. These studies were limited by Doppler effects related to the difference frequencies of the laser beams used for CARS, yielding experimental uncertainties for the obtained transition frequencies of about 15 MHz.

Although the absorption spectra of molecular hydrogen can be measured by CRDS with very high sensitivity, the Doppler width at the 1 GHz level remains an obstacle to the determination of the line positions at a sub-MHz uncertainty. Figure 28(a) shows an example of the R(1) (2-0) line of HD near 1380 nm recorded by the Hefei group. The signal-to-noise ratio is several thousand, but the fitting residuals show obvious interference due to nearby water absorption lines. Another more serious problem originates from the line profile model. The hydrogen molecule has a relatively strong speed dependence on collisional shifting that results in a line asymmetry of Doppler-limited spectra recorded under finite pressures. Velocity-changing collisions (namely, Dicke narrowing effects) and speed dependence of collisional broadening and shifting must therefore be carefully considered in the line profile model [244], but still it is very challenging to fit the experimental spectrum correctly to an accuracy better than 1/10,000 of the linewidth.

The Caserta group proposed a solution adopting the so-called β-corrected Hartmann–Tran (βHT) profile [245]. This model, which represents an evolution of the well-known Hartmann–Tran (HT) profile [246], describes the various collisional perturbations to the lineshape, while being also capable of a more reliable representation of the Dicke narrowing effect in the case of light molecules like molecular hydrogen. In the refined spectral analysis of Ref. [238], line asymmetry due to the speed dependence of collisional shifting and to the unresolved hyperfine structure was carefully investigated, thus providing an improved determination of the absolute line center frequency for the weak R(1) (2-0) line of HD. In fact, for any HD rovibrational line, the absorption coefficient is due to a manifold of closely spaced hyperfine components, whose overlapping βHT profiles yield to absorption spectra similar to those reported in Fig. 29. In the fitting procedure, a global approach was implemented, while setting the hyperfine separations at the theoretical values of Ref. [247] and treating the centroid as a variable quantity. As a result, an updated determination of the R(1) frequency was provided, the combined uncertainty being reduced from 109 kHz of Ref.

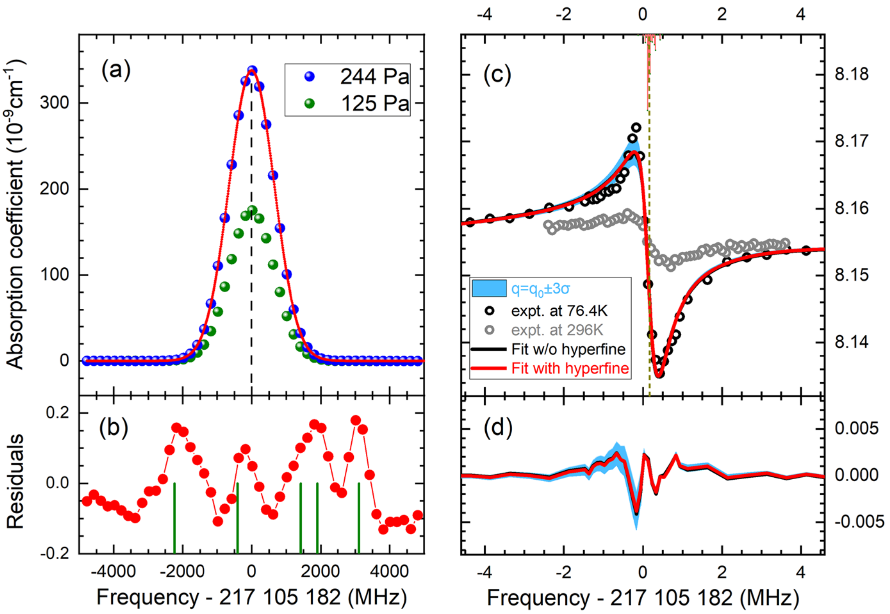

Fig. 28 (**a**) Doppler-broadened R(1) (2-0) line of HD recorded by CRDS with sample pressures of 244 Pa and 125 Pa. The dashed line indicates the center of the HD line. (**b**) Residuals of fitting the spectrum of 244 Pa with a Gaussian function. Green lines show the positions of water lines with intensity over 2×10^{-26} cm molecule^{-1} in this region given by the HITRAN database [153]. (**c**) Lamb-dip spectra of the R(1) (2-0) line recorded by CRDS at 76.4 K (gray circles) and 296 K (black circles). Solid lines are the simulated spectra using a Fano profile. The stick spectrum shows the calculated hyperfine components. The dashed line shows the gravity center of the transition. (**d**) Fitting residuals between the simulated and experimental spectra at 76.4 K. The HD molecular density was estimated to be 7×10^{14} molecules/cm^3. Panels (**c**) and (**d**) reprinted (Fig. 3) with permission from [243], Copyright (2022) by the American Physical Society

[84] to 76 kHz [238]. Obtained from collision-perturbed spectra at room temperature, this measurement is in perfect agreement with the one performed by the Grenoble group at the liquid nitrogen temperature and at HD pressures of 2 Pa [239].

Meanwhile, the relative simplicity of the hydrogen molecule allows for investigating collisional effects through ab initio quantum chemistry calculations. In this respect, Doppler-limited absorption spectroscopy of the hydrogen molecule is a perfect testing ground for collision-induced line-shape effects. The Torun group has undertaken a series of studies of the CRDS spectral profiles of H_2 in pure gas [244, 248], in mixtures with He [249–251], and with Ar [252, 253]. Agreement between experimental and theoretical line profiles has been achieved with fractional deviations at the level of 10^{-4}–10^{-3}.

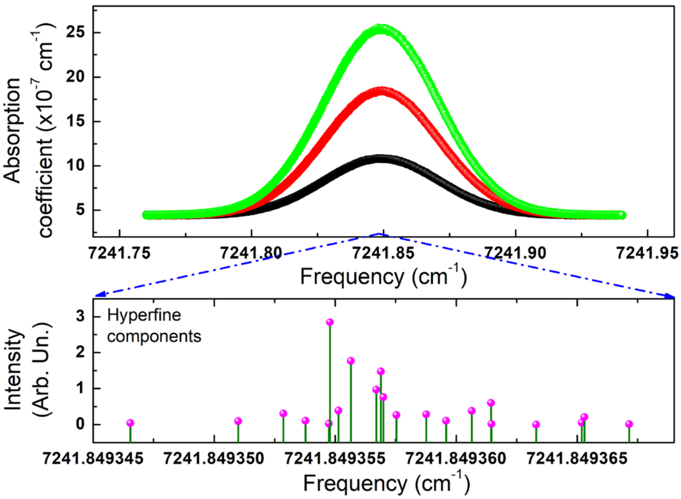

Fig. 29 Example spectra for the R(1) line as a function of the HD pressure (varying from ∼200 to ∼1200 Pa), as recorded by the Caserta group using CL-FS-CRDS at 1.38 µm. Bottom: Theoretical prediction of the underlying hyperfine structure. The experimental line shape is due to the sum of 21 non-Voigt profiles. Each of them is far from being a Gaussian function. Reprinted (Fig. 1) with permission from [238], Copyright (2021) by the American Physical Society

Table 1 Saturation intensity (I_s) of the transition, assuming that the transition width is 1 MHz

	ν, cm^{-1}	k, cm/molecule	A, s^{-1}	I_s, W/cm^2
H_2, Q(1) (1-0)	4155.254	2.174×10^{-26}	4.287×10^{-7}	2.8×10^{8}
H_2, Q(1) (2-0)	8075.307	2.602×10^{-27}	1.938×10^{-7}	4.5×10^{9}
HD, R(1) (1-0)	3798.452	1.469×10^{-24}	2.462×10^{-5}	3.7×10^{6}
HD, R(1) (2-0)	7241.849	3.526×10^{-25}	2.148×10^{-5}	2.9×10^{7}

Line positions (ν), strengths k, and the Einstein A-coefficients are given by Pachucki et al. [254], now also available in the HITRAN database [153]

6.2 Doppler-free spectroscopy

Doppler-free saturation spectroscopy is a favored approach to reduce the spectral linewidth and therewith determine accurate transition frequencies of molecular resonances. However, high laser powers are required to saturate vibrational transitions, in particular the weak resonances in HD and H_2. The saturation intensity of an infrared transition is related to its transition rate and linewidth through the Eq. [36]:

$$I_s = \frac{8\pi^3 hc}{3A} \frac{\Gamma^2}{\lambda^3}, \tag{28}$$

where A is the Einstein A-coefficient, Γ is the linewidth (FWHM), h is the Planck constant, c is the speed of light, and λ is the wavelength. In Table 1 the saturation laser powers for several transitions of H_2 and HD are presented. For simplicity, we take the width of the transition (full width at half maximum) at 1 MHz, which is usually dominated by transit-time broadening or collision broadening. With commercially available continuous-wave lasers these transitions can hardly be saturated, in single-path configurations. Here the power enhancement capability of intracavity absorption methods comes to a rescue: with currently available highly reflective mirrors (at $R = 99.999\%$) intracavity powers can be boosted by a factor of 10^5.

Besides the requirement of sufficient laser power for saturating a transition, also a good detection sensitivity is needed for probing a Lamb-dip signal. Note that a Lamb dip is located on top of a Doppler-broadened absorption profile, where the depth of the Lamb dip is proportional to the product of the line strength and the molecular number density. Therefore, it is much easier to detect a Lamb-dip signal for a strong line if the laser power is limited. Meanwhile, it is not very helpful to measure at a high sample pressure, since the pressure-induced broadening also increases with the pressure and the saturation power given in Eq. (28) is proportional to the square of the linewidth. Therefore, comparing the transition strengths and saturation powers of H_2 and HD, as shown in Table 1, E1 transitions of HD are preferable for Lamb-dip measurements. Since the first overtone of HD is located in the near-infrared region and mature narrow-linewidth diode lasers are available, it is natural that the first choice would be the R(1) line in the (2-0) band of HD as the target. Note that the R(0) line is close to strong water lines, prohibiting its study at room temperature.

Saturation spectroscopic measurements of the HD R(1) (2-0) line at 1380 nm were reported by the Hefei group [181] and the Amsterdam group [129] with different experimental methods. The Hefei group used the CRDS method based on a 1-m-long cavity with a finesse of about 1.2×10^5. The Amsterdam group used the NICE-OHMS method based on a half-meter-long cavity with a finesse of 1.5×10^5. The circulating laser power was about 100 W in both measurements. Both groups observed narrow spectral features and used optical combs to determine the frequencies of the line “centers”. However, the two frequencies have an astonishing difference of 0.9 MHz, which is almost 10 times the combined uncertainty of both measurements. Later, both the Hefei and Amsterdam groups re-measured the spectra with improved sensitivity and revealed that the saturation spectrum of the HD line has an unexpected asymmetric line profile [123, 255]. Instead of the conventional Lamb dip in the saturation absorption spectrum, a composite profile including both “peak” and “dip” was found for the R(1) line of HD. The Hefei group measured the spectrum with three different methods, CRDS, CEAS, and NICE-OHMS, on one instrument, and confirmed that all experimental results from different methods were in agreement with each other [123, 256]. Figure 28 shows the saturated CRDS spectrum, alongside the Doppler-broadened spectrum, recorded by the Hefei group. Since no frequency modulation was applied in the CRDS measurement, the experimental spectrum shows the original line profile of the saturated absorption sub-Doppler curve. We can see that the asymmetric line shape is more pronounced at the low temperature of 76 K.

Different mechanisms have been proposed to explain the very unusual asymmetry in the profile. One focus is the hyperfine structures due to the nuclear spin 1/2 for the proton and spin 1 for the deuteron. Coupling between the nuclear spin and rotational angular momentum splits the lower energy state of the R(1) (2-0) transition to 5 levels with total angular momentum quantum number F of $\frac{1}{2}$, $\frac{3}{2}$, and $\frac{5}{2}$, and the upper state

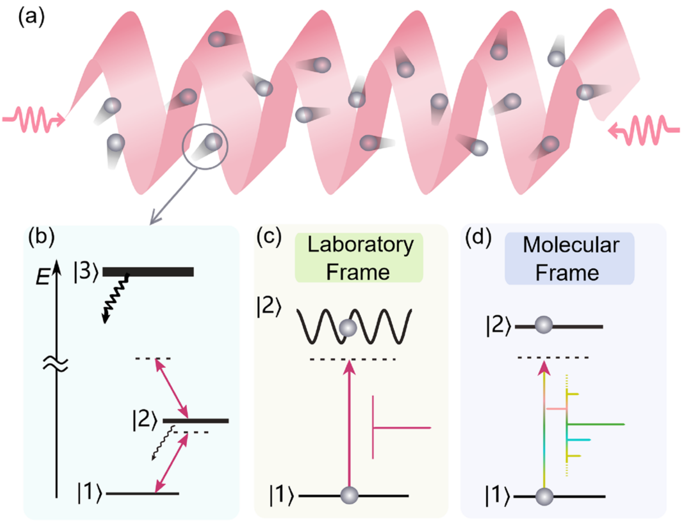

Fig. 30 Principle of the nonlinear Fano resonance in low-lying states of molecules. (**a**) The experimental arrangement for the absorption spectrum measurement of moving molecules, probed by a standing wave field with wavelength λ. (**b**) Energy level diagram. Simplified energy level diagram for a molecule with speed V in the laboratory frame (**c**) and in the molecular frame (**d**). Reprinted (Fig. 1) with permission from [257], Copyright (2022) by the American Physical Society

was split to 6 levels with F in the range of $\frac{1}{2} - \frac{7}{2}$. In total, 21 hyperfine components of the transition spread within a range of 0.6 MHz (see Fig. 29), and the separations were calculated with kHz precision by several groups [258–260]. The crossover between each pair of sub-transitions sharing the same upper or lower energy level can further complicate the spectrum. Diouf et al. considered different types of crossovers and proposed a model taking into account a hypothesis of population transferring among the sublevels due to collisions. In this way, their numerical calculations show a composite line shape that can explain the experimental spectrum, and the center frequency of the R(1) (2-0) line was determined to be 217 105 181 901(50) kHz [255].

The same model was also applied to model the spectrum of the P(1) line in the (2-0) of HD measured under saturation conditions. Surprisingly, the hyperfine-crossover model, which accounted for a dispersive profile in the case of R(1), predicted a Lamb peak structure for the P(1) line, as was experimentally observed [125]. All lines in the same vibrational band, other than P(1), were observed as a dispersive line shape, and the similarity of line profiles allowed for a determination of combination differences, and therewith rotational splittings in the HD molecule [261, 262].

The Hefei group investigated the interference between a near-resonant weak transition and distant strong transitions and found that the saturated absorption spectrum of the weak transition in a standing-wave field exhibits a Fano-like asymmetric line shape [257]. Figure 30 shows the diagram of the mechanism. A three-level system was considered for a molecule in a standing-wave field. The laser frequency is near-resonant with the weak transition between states $|1\rangle$ and $|2\rangle$ but very far detuned from the strong transition between $|2\rangle$ and $|3\rangle$. For such a model, the strong electronic transition in a molecule should be stronger than a weak rovibrational transition by over ten orders of magnitude, as is indeed the case when comparing the (2-0) vibrational band to the electronic Lyman and Werner bands in HD. Therefore, the AC Stark shift due to the presence of state $|3\rangle$ induces a considerable shift to the weak transition, and the shift is spatially modulated by the standing wave. As a result, in the molecular frame, the molecule will experience a laser field with sidebands. Interactions between the molecule and the laser field, including the carrier and the sidebands, will induce a composite line profile which is effectively reproduced by a Fano function [263]. Numerical calculations based on this model were carried out, agreeing well with the experimental results observed for the Lamb-dips of a few very weak transitions of CO_2 near 1.6 μm. Fano-like profiles, similar to that observed in the HD lines, were observed for these CO_2 lines with Einstein-A coefficients at the level of 10^{-5} s^{-1}, close to that of the R(1) line of HD. Note that this mechanism is effective for a single line without hyperfine structures, and hyperfine structures are absent or negligible for these CO_2 lines. The model was applied to fit the R(1) (2-0) Lamb-dip spectrum of HD measured at 76 K, which yields a line center of $217\,105\,182\,284(11)_{\text{stat}}(27)_{\text{sys}}$ kHz after taking into account the systematic correction [243]. Note that there is a deviation of 383(58) kHz from that given by Diouf et al. [255], indicating the requirement for further investigations.

The Amsterdam group, in collaboration with the Tritium Laboratory Karlsruhe, extended the NICE-OHMS studies to HT for which a dedicated setup with a getter was built. Specific SAES-St171 getters were used for evacuating the cell to low base pressure in between measurements, while heating up the getter materials provided a controlled method for releasing tritiated hydrogen molecules into the cell. This made it possible to carry out saturated absorption measurements on HT gas, similarly to HD [265]. The advantage of using HT is that its hyperfine structure in several transitions in the (2-0) band exhibits a single isolated hyperfine component. In the experiment, that component was observed as a single Lamb dip for the R(0) and R(1) lines, while the majority of hyperfine components produced a strong feature resembling the dispersive line profile as observed in HD. Frequency metrology on that single component, and a computed shift from the rovibrational center-of-gravity [266], yielded rather accurate values for the rovibrational transition frequencies. This allowed for deriving accurate transition frequencies for the R(0) and R(1) lines in HT. The P(1) line was also observed for HT, giving rise to a spectrum represented by Lamb peaks, similar as observed for HD [125]. The single isolated component in P(1) was also observed as a Lamb peak instead of a dip, while the strong feature composed of many other hyperfine components of P(1) remains unexplained.

The Amsterdam team further built a vibration-isolated cryo-cooled setup for performing NICE-OHMS studies. In this setup a measurement of the S(0) quadrupole line in the (2-0) overtone band in H_2 could be measured in saturation [264]. A spectral recording of the Lamb dip, measured at rather low circulating intracavity powers of 200 Watt, a wavelength of 1280 nm, and a pressure of 0.1 Pa is shown in Fig. 31. A remarkable feature of the spectrum, now observed as a single narrow Lamb dip, is that the line shape can by no means account for a recoil doublet with 140 kHz splitting (see illustration in the top panel of Fig. 31), as is expected for this transition [267]. It

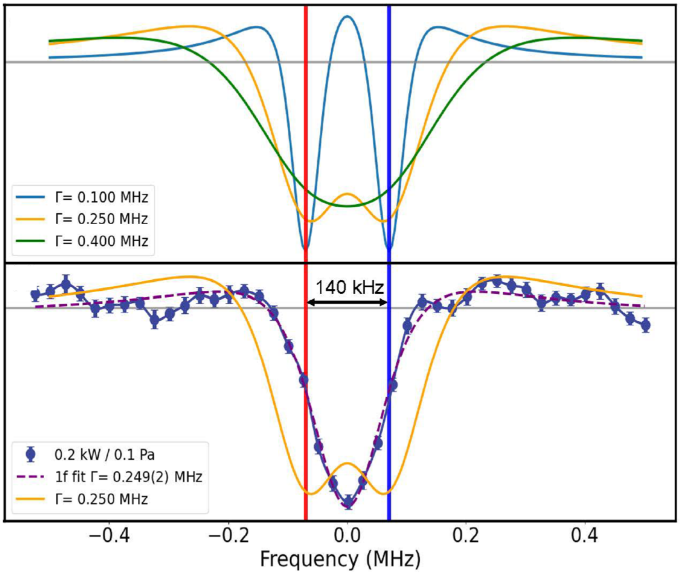

Fig. 31 Spectral recording and analysis of the H_2 S(0) (2-0) line measured via NICE-OHMS. In the top panel possible line shapes are computed based on a recoil splitting of 140 kHz. The lower panel shows that none of the suggested models can explain a recoil doublet. Reprinted (Fig. 4b) with permission from [264], Copyright (2023) by the American Physical Society

was concluded that under the measurement conditions, the red recoil component was suppressed. This is however an open issue for which further proof is required.

The studies on the quadrupole overtone transition in H_2 was extended with a measurement of the Q(1) line [122]. In this study, the hyperfine components were resolved for the first time in a rovibrational transition in the H_2 homonuclear molecule. Another achievement of that study was that a single absorption component at a line strength of 4.4×10^{-28} could be detected in saturation.

6.3 Comparing theoretical and experimental results

Table 2 lists all the line positions of molecular hydrogen with sub-MHz accuracy reported in the literature so far. Most of them are obtained from cavity-enhanced absorption spectroscopy and cavity ring-down spectroscopy in low-pressure gas cells, via either Doppler-broadened or saturation techniques. Splittings between rotational levels in the $v = 0$ ground state of HD were determined via measured combination differences, notwithstanding the dispersive line shapes [261, 262]. A single result was obtained via stimulated Raman spectroscopy [268]. In addition, laser spectroscopy of molecular hydrogen in molecular beams was carried out by Fast and Meek [269, 270] in Göttingen, who determined frequencies of the R(0) (1-0) line of HD and the S(1) (1-0) line of D_2 with a fractional uncertainty at the 10^{-10} level.

The calculated line positions, derived via the H2SPECTRE program [212], are also included in the table. The quantum electrodynamics correction to the rovibrational

Table 2 Some precise frequencies of molecular hydrogen with sub-MHz accuracy

$(v', N') \leftarrow (v, N)$	ν, calc, MHz	ν, exp, MHz	$\Delta\nu$, MHz	Method	References
H_2					
(1, 1) ← (0, 1)	124 571 373.89(78)	124 571 374.73(31)	0.8	Raman	[268]
(2, 2) ← (0, 0)	252 016 358.5(15)	252 016 361.16(6)	2.6	Doppler	[271]
		252 016 361.164(8)	2.6	Lamb dip	[264]
(2, 1) ← (0, 1)	242 091 627.7(15)	242 091 630.140(9)	2.4	Lamb dip	[122]
(2, 3) ← (0, 1)	257 947 882.1(15)	257 947 884.67(3)	2.6	Doppler	[271]
(2, 2) ← (0, 2)	241 392 519.3(15)	241 392 522.00(34)	2.7	Doppler	[271]
(2, 3) ← (0, 3)	240 349 104.6(15)	240 349 107.16(70)	2.6	Doppler	[271]
D_2					
(1, 3) ← (0, 1)	94 925 100.0(4)	94 925 100.487(17)	0.5	Beam	[270]
(2, 2) ← (0, 0)	180 914 269.04(72)	180 914 269.55(30)	0.5	Doppler	[230]
(2, 4) ← (0, 2)	187 104 298.90(63)	187 104 300.04(39)	1.1	Doppler	[229]

Table 2 continued

$(v', N') \leftarrow (v, N)$	ν, calc, MHz	ν, exp, MHz	$\Delta\nu$, MHz	Method	References
HD					
(0, 1) ← (0, 0)	2 674 986.073(18)	2 674 986.094(24)	0.0	Lamb dip	[236]
(0, 2) ← (0, 0)	8 006 533.126(66)	8 006 533.168(26)	0.0	Comb diff	[262]
(0, 3) ← (0, 1)	13 283 244.94(11)	13 283 245.098(30)	0.2	Comb diff	[261]
(1, 1) ← (0, 0)	111 448 814.5(6)	111 448 815.477(13)	1.0	Beam	[269]
(2, 1) ← (0, 0)	214 905 333.3(11)	214 905 335.185(20)	1.9	Doppler	[239]
(2, 2) ← (0, 1)	217 105 180.2(9)	217 105 181.581(109)	1.4	Doppler	[84]
		217 105 181.901(76)	1.7	Doppler	[272]
		217 105 181.901(50)	1.7	Lamb dip	[255]
		217 105 182.11(24)	1.9	Lamb dip	[123]
		217 105 182.285(27)	2.1	Lamb dip	[243]
		217 105 181.898(20)	1.7	Doppler	[239]
(2, 0) ← (0, 1)	209 784 240.1(10)	209 784 242.007(20)	1.9	Lamb dip	[125]
(2, 3) ← (0, 2)	219 042 854.9(9)	219 042 856.621(28)	1.7	Lamb dip	[129]
(2, 4) ← (0, 3)	220 704 303.2(9)	220 704 304.951(28)	1.8	Lamb dip	[129]
		220 704 305.23(24)	2.0	Lamb dip	[123]
HT					
(2, 0) ← (0, 1)	198 824 819.0(9)	198 824 820.600(100)	1.6	Lamb dip	[265]
(2, 1) ← (0, 0)	203 396 424.9(9)	203 396 426.692(21)	1.9	Lamb dip	[265]
(2, 2) ← (0, 1)	205 380 031.7(9)	205 380 033.644(22)	1.9	Lamb dip	[265]

energies of molecular hydrogen has been calculated with an estimated uncertainty of 1 MHz, which is currently lagging behind experimental progress. The major cause of uncertainty is in the $E^{(5)}$ energy term [273], while further investigation of the high-order nonadiabatic $E^{(7)}$, $E^{(8)}$ energy terms in Eq. (27) is yet to be calculated. A striking observation is that the calculated frequencies are all lower than the experimental ones by 1–2 MHz, about twice the calculation uncertainties. The deviation remains almost the same for different rotational lines in one vibrational band but increases with the vibrational quanta, implying a systematic vibrational shift in the calculation. Here it may be noted that the calculations of the dissociation energy D_0 are more accurate than those of the vibrational transitions, as a result of the most advanced computational framework used, beyond NAPT [199, 202].

Doppler-limited laser absorption spectroscopy of molecular hydrogen has the advantage of simplicity and the high signal-to-noise ratio allows for accuracies even below the 100 kHz level [238, 239, 271], but further improvement is limited by the broad linewidth and the collision-induced mixing and shifting yet to be investigated. Doppler-free saturated absorption spectroscopy requires state-of-the-art instruments to detect the very tiny saturation signal. Lamb "dips" of a few relatively strong dipole transitions of heteronuclear HD and HT molecules have been explored in the last few years, and the precision has reached a few tens of kilohertz. However, the unexpected asymmetric line profile prevents further improvement in the determination of the line centers. Further studies toward better accuracy require investigations into the hyperfine structures and complicated crossovers among these hyperfine components. The Doppler-free NICE-OHMS spectroscopy of overtone quadrupole transitions of H_2 places an obvious outlier of the conventional understanding of cavity-enhanced saturated absorption spectroscopy [122, 264]. Although in the case of H_2 a novel problem has arisen in interpreting signals, related to the non-observation of expected recoil doublets. Various effects in the spectroscopy of the simplest molecule, such as the collision effects and the interaction between a very narrow transition and the laser field, could be benchmarks for further investigations.

7 Conclusion and perspectives

This review shows that the field of cavity-based techniques have expanded tremendously over the past three decades. Numerous experiments are being performed, targeting fundamental spectroscopy of molecules to provide information on their quantum-level structure, pursuing applications of spectroscopy aimed at sensitive detection in a variety of environments, and testing fundamental physics in the realm of molecules. The Web of Science database provides information on the literature produced on the subject in this era. Figure 32 displays the numbers of publications as well as citations, the entries being cavity ring-down spectroscopy and cavity-enhanced spectroscopy (CES). This amounted to over 3500 papers for CRDS and over 4500 items for CES, respectively, for the years after 1989, assumed as the year after the CRDS invention [11]. The total number of citations to these papers is over 200,000. NICE-OHMS experiments contribute with about 80 entries in Web of Science, not a large number considering the fact that the invention is about 25 years old [24, 25].

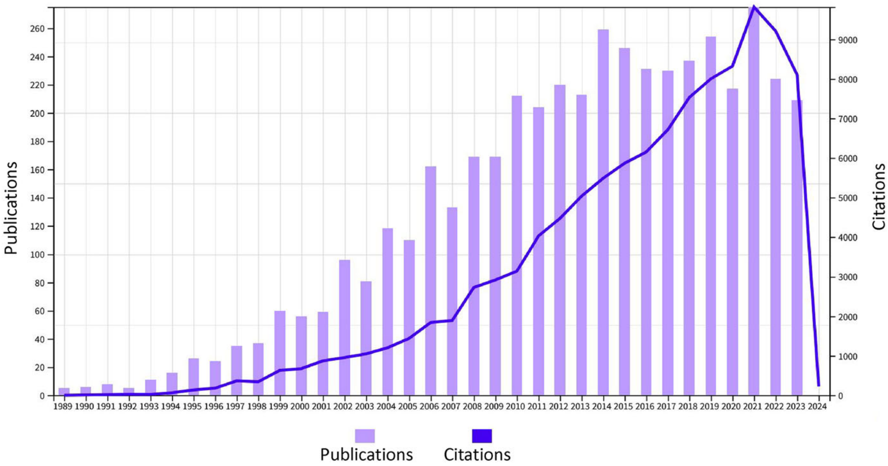

Fig. 32 Evolution of number of papers (> 7600) and number of citations (> 200,000) as documented in the Web of Science over the years 1989–2023 for a combined entry of "cavity ring-down spectroscopy" and "cavity-enhanced spectroscopy". Numbers downloaded on February 2024

The fact that this number is much lower than that for CRDS and CES techniques may be attributed to its more complex opto-electronic configurations. Also, as discussed, the NICE-OHMS technique does not lend itself to recording congested spectra and, in some cases of light molecules, not even Doppler-broadened spectra.

Cavity-enhanced optical techniques have revolutionized the field of laser spectroscopy in two-fold directions. The sensitivity for the detection of molecules has increased mainly by the extended absorption path lengths that can be attained inside high-finesse optical resonators. For Doppler-broadened transitions, the sensitivity can be pushed down to an $\alpha_{\min}$ of 5×10^{-13} cm^{-1}, which translates into a limit of detection (in terms of minimum detectable line intensity factor) of 10^{-31} cm/molecule. Also, the detection of very weak quadrupole transitions in the rovibrational manifold of water has been accomplished. Two-photon transitions could also be detected, although limited to excitations exhibiting a near-resonance at the one-photon level. The introduction of high-finesse cavities also gave a boost to power levels at which resonances can be probed, opening up wide opportunities to perform Lamb-dip spectroscopy on weak molecular vibrations. Combined with the use of frequency-comb lasers, another revolution in spectroscopy, this has pushed the accuracy of frequency measurements some three orders of magnitude (from the MHz to sub-kHz level of accuracy), compared to conventional Doppler-broadened spectroscopy. In this regard, a limiting factor is given by transit times of molecules passing through the intracavity laser beams, therewith leading to Heisenberg broadening of the sub-Doppler line. Further improvements in spectral resolution into the sub-kHz domain can be obtained using cryogenic conditions to lower the molecular velocities, thus increasing transit times [243, 264]. Another powerful approach combines the CRDS technique with buffer-gas cooling so that both the internal and translational temperatures of the probed molecular species are reduced down to a few Kelvin [274]. Ultimately, trapping of cold samples of molecules in the standing wave pattern in an optical cavity could help improve the resolution and accuracy of spectroscopic experiments as was recently suggested for the specific case of H_2 [275].

Cavity-enhanced and cavity ring-down saturated spectroscopic techniques have spurred the development of spectroscopic networks, as highlighted in this review for water (in Sect. 5.1) and for acetylene (in Sect. 5.2). These approaches supersede the description of the molecular structure in terms of effective Hamiltonians, in particular for molecules exhibiting a dense and multi-level quantum structure which is assessed at kHz precision. In such cases, effective Hamiltonians require many levels of centrifugal distortion parameters in cases where light hydrogen atoms are part of the molecular structure. Then the network approaches such as the Spectroscopic Network-Assisted Precision Spectroscopy (SNAPS) as applied for water [152, 160] and the Measured Active Rotational-Vibrational Energy Levels (MARVEL) approach as applied for acetylene [171, 172, 179] become viable alternatives. The information of networks can be condensed in deriving extremely accurate energies for quantum levels that connect large numbers of other levels in the molecules. The derivation and description of such HUBs, connecting many paths in the language of network theory, was recently demonstrated for water [276].

As discussed in the previous section, the hydrogen molecule and its isotopologues have become a benchmark for testing molecular quantum electrodynamics, and even probing physics beyond the Standard Model. The focus of measurement of the dissociation energies, based on electronic transitions, is now gradually shifting toward precision measurement of vibrational transitions. It should be realized that all molecular hydrogen isotopologues, of which there are 6 when tritium is included, have over 300 bound rovibrational levels with lifetimes of minutes to weeks, making the hydrogen molecule a well-suited test bench for testing QED. This may be compared to the hydrogen atom, which has only one reasonably long-lived excited state, the 2 S level, with a lifetime of 1 s.

Lamb-dip features could be probed in the HD and HT heteronuclear species, but there the analysis and frequency accuracy turned out to be limited by the observation of dispersive line shapes. Various models have been proposed to explain those lines shapes, but a full quantitative analysis is still lacking. If that task can be accomplished the absolute accuracy for rovibrational transitions may be improved to the kHz level. A subsequent breakthrough was accomplished in the measurement of a vibrational transition in the homonuclear H_2 species, where a single Lamb dip was indeed observed. A bottleneck in these studies is the observation of a single recoil component, which is contrary to prediction. Again, if these problems of interpretation can be resolved, a highly accurate value for the vibrational quantum energies in H_2 can be determined, allowing for a more stringent test of fundamental physics.

Acknowledgements We are grateful to the students, post-doctoral fellows and colleagues who worked in our respective laboratories, including Antonio Castrillo and Eugenio Fasci at University of Campania, Frank Cozijn, Meissa Diouf and Edcel Salumbides at VU Amsterdam, and Cun-Feng Cheng at University of Science and Technology of China (Hefei).

Author Contributions The authors contributed to the manuscript equally.

Funding Open access funding provided by Università degli Studi della Campania Luigi Vanvitelli within the CRUI-CARE Agreement. WU acknowledges financial support from the European Research Council (Grant Agreement No. 670168) and the Netherlands Organisation for Scientific Research (NWO) for the program "The mysterious size of the proton". SMH acknowledges the support from the National Natural Science Foundation of China (Grant No. 12393825). LG is grateful to EURAMET, the European Association of National Metrology Institutes, for supporting the CRDS activities within the EMPIR program.

Data availability This is a review article. However, data are available from the authors, if needed.

Declarations

Conflict of interest The authors have no relevant financial or non-financial interests to disclose.

References

1. R.N. Hall, G.E. Fenner, J.D. Kingsley, T.J. Soltys, R.O. Carlson, Coherent light emission from GaAs junctions. Phys. Rev. Lett. **9**, 366 (1962). https://doi.org/10.1103/PhysRevLett.9.366
2. G.C. Bjorklund, Frequency-modulation spectroscopy: a new method for measuring weak absorptions and dispersions. Opt. Lett. **5**, 15 (1980). https://doi.org/10.1364/OL.5.000015
3. J.U. White, Very long optical paths in air. J. Opt. Soc. Am. **66**, 411 (1976). https://doi.org/10.1364/JOSA.66.000411
4. D. Herriott, H. Kogelnik, R. Kompfner, Off-axis paths in spherical mirror interferometers. Appl. Opt. **3**, 523 (1964). https://doi.org/10.1364/AO.3.000523
5. J.B. McManus, P.L. Kebabian, M.S. Zahniser, Astigmatic mirror multipass absorption cells for long-path-length spectroscopy. Appl. Opt. **34**, 3336 (1995). https://doi.org/10.1364/AO.34.003336
6. D.A. Jackson, The spherical Fabry–Perot interferometer as an instrument of high resolving power for use with external or with internal atomic beams. Proc. R. Soc. Lond. Ser. A. Math. Phys. Sci. **263**, 289 (1961). https://doi.org/10.1098/rspa.1961.0161
7. A. Kastler, Atomes à l'intérieur d'un interféromètre Perot–Fabry. Appl. Opt. **1**, 17 (1962). https://doi.org/10.1364/AO.1.000017
8. A. Kastler, Transmission of light pulse through a Fabry–Perot interferometer. Nouv. Rev. Opt. **5**, 133 (1974). https://doi.org/10.1088/0335-7368/5/3/301
9. J.M. Herbelin, J.A. McKay, M.A. Kwok, R.H. Ueunten, D.S. Urevig, D.J. Spencer, D.J. Benard, Sensitive measurement of photon lifetime and true reflectances in an optical cavity by a phase-shift method. Appl. Opt. **19**, 144 (1980). https://doi.org/10.1364/AO.19.000144
10. D.Z. Anderson, J.C. Frisch, C.S. Masser, Mirror reflectometer based on optical cavity decay time. Appl. Opt. **23**, 1238 (1984). https://doi.org/10.1364/AO.23.001238
11. A. O'Keefe, D.A.G. Deacon, Cavity ring-down optical spectrometer for absorption measurements using pulsed laser sources. Rev. Sci. Instrum. **59**, 2544 (1988). https://doi.org/10.1063/1.1139895
12. H. Naus, W. Ubachs, Experimental verification of Rayleigh scattering cross sections. Opt. Lett. **25**, 347 (2000). https://doi.org/10.1364/OL.25.000347
13. M. Sneep, W. Ubachs, Cavity ring-down measurement of the O_2-O_2 collision-induced absorption resonance at 477 nm at sub-atmospheric pressures. J. Quant. Spectrosc. Radiat. Transf. **78**, 171 (2003). https://doi.org/10.1016/S0022-4073(02)00190-5
14. S. Xu, G. Sha, J. Xie, Cavity ring-down spectroscopy in the liquid phase. Rev. Sci. Instrum. **73**, 255 (2002). https://doi.org/10.1063/1.1430729

15. K.L. Snyder, R.N. Zare, Cavity ring-down spectroscopy as a detector for liquid chromatography. Anal. Chem. **75**, 3086 (2003). https://doi.org/10.1021/ac0340152
16. B. Bahnev, L. van der Sneppen, A.E. Wiskerke, F. Ariese, C. Gooijer, W. Ubachs, Miniaturized cavity ring-down detection in a liquid flow cell. Anal. Chem. **77**, 1188 (2005). https://doi.org/10.1021/ac048428u
17. L. van der Sneppen, A. Wiskerke, F. Ariese, C. Gooijer, W. Ubachs, Improving the sensitivity of HPLC absorption detection by cavity ring-down spectroscopy in a liquid-only cavity. Anal. Chim. Acta **558**, 2 (2006). https://doi.org/10.1016/j.aca.2005.11.022
18. D. Romanini, A. Kachanov, N. Sadeghi, F. Stoeckel, CW cavity ring down spectroscopy. Chem. Phys. Lett. **264**, 316 (1997). https://doi.org/10.1016/S0009-2614(96)01351-6
19. D. Romanini, A. Kachanov, F. Stoeckel, Diode laser cavity ring down spectroscopy. Chem. Phys. Lett. **270**, 538 (1997). https://doi.org/10.1016/S0009-2614(97)00406-5
20. B.A. Paldus, C.C. Harb, T.G. Spence, B. Wilke, J. Xie, J.S. Harris, R.N. Zare, Cavity-locked ring-down spectroscopy. J. Appl. Phys. **83**, 3991 (1998). https://doi.org/10.1063/1.367155
21. B.A. Paldus, A.A. Kachanov, An historical overview of cavity-enhanced methods. Can. J. Phys. **83**, 975 (2005). https://doi.org/10.1139/p05-054
22. K. Nakagawa, T. Katsuda, A. Shelkovnikov, M. de Labachelerie, M. Ohtsu, Highly sensitive detection of molecular absorption using a high finesse optical cavity. Opt. Commun. **107**, 369 (1994). https://doi.org/10.1016/0030-4018(94)90349-2
23. L. Gianfrani, R. Fox, L. Hollberg, Cavity-enhanced absorption spectroscopy of molecular oxygen. J. Opt. Soc. Am. B **16**, 2247 (1999). https://doi.org/10.1364/JOSAB.16.002247
24. J. Ye, L.-S. Ma, J. Hall, Sub-Doppler optical frequency reference at 1.064 μm by means of ultrasensitive cavity-enhanced frequency modulation spectroscopy of a C_2HD overtone transition,. Opt. Lett. **21**, 1000 (1996). https://doi.org/10.1364/OL.21.001000
25. J. Ye, L.-S. Ma, J. Hall, Ultrasensitive detections in atomic and molecular physics: demonstration in molecular-overtone spectroscopy. J. Opt. Soc. Am. B **15**, 6 (1998). https://doi.org/10.1364/JOSAB.15.000006
26. R. Engeln, G. Berden, R. Peeters, G. Meijer, Cavity enhanced absorption and cavity enhanced magnetic rotation spectroscopy. Rev. Sci. Instrum. **69**, 3763 (1998). https://doi.org/10.1063/1.1149176
27. A. O'Keefe, J.J. Scherer, J.B. Paul, CW integrated cavity output spectroscopy. Chem. Phys. Lett. **307**, 343 (1999). https://doi.org/10.1016/S0009-2614(99)00547-3
28. J.B. Paul, L. Lapson, J.G. Anderson, Ultrasensitive absorption spectroscopy with a high-finesse optical cavity and off-axis alignment. Appl. Opt. **40**, 4904 (2001). https://doi.org/10.1364/AO.40.004904
29. M.C.J. Morville, S. Kassi, D. Romanini, Fast, low-noise, mode-by-mode, cavity-enhanced absorption spectroscopy by diode-laser self-locking. Appl. Phys. B **80**, 1027 (2005). https://doi.org/10.1007/s00340-005-1828-z
30. R. Engeln, G. von Helden, G. Berden, G. Meijer, Phase shift cavity ring down absorption spectroscopy. Chem. Phys. Lett. **262**, 105 (1996). https://doi.org/10.1016/0009-2614(96)01048-2
31. R. Engeln, G. Berden, E. van den Berg, G. Meijer, Polarization dependent cavity ring down spectroscopy. J. Chem. Phys. **107**, 4458 (1997). https://doi.org/10.1063/1.474808
32. M.D. Levenson, B.A. Paldus, T.G. Spence, C.C. Harb, J.S. Harris Jr., R.N. Zare, Optical heterodyne detection in cavity ring-down spectroscopy. Chem. Phys. Lett. **290**, 335 (1998). https://doi.org/10.1016/S0009-2614(98)00500-4
33. Y. He, B.J. Orr, Ringdown and cavity-enhanced absorption spectroscopy using a continuous-wave tunable diode laser and a rapidly swept optical cavity. Chem. Phys. Lett. **319**, 131 (2000). https://doi.org/10.1016/S0009-2614(00)00107-X
34. B.J. Orr, Y. He, Rapidly swept continuous-wave cavity-ringdown spectroscopy. Chem. Phys. Lett. **512**, 1 (2011). https://doi.org/10.1016/j.cplett.2011.05.052
35. S.M. Ball, I.M. Povey, E.G. Norton, R.L. Jones, Broadband cavity ringdown spectroscopy of the NO_3 radical. Chem. Phys. Lett. **342**, 113 (2001). https://doi.org/10.1016/S0009-2614(01)00573-5
36. G. Giusfredi, S. Bartalini, S. Borri, P. Cancio, I. Galli, D. Mazzotti, P. De Natale, Saturated-absorption cavity ring-down spectroscopy. Phys. Rev. Lett. **104**, 110801 (2010). https://doi.org/10.1103/PhysRevLett.104.110801
37. A. Cygan, D. Lisak, P. Morzyński, M. Bober, M. Zawada, E. Pazderski, R. Ciuryło, Cavity mode-width spectroscopy with widely tunable ultra narrow laser. Opt. Express **21**, 29744 (2013). https://doi.org/10.1364/OE.21.029744

38. A. Cygan, P. Wcisło, S. Wójtewicz, P. Masłowski, J.T. Hodges, R. Ciuryło, D. Lisak, One-dimensional frequency-based spectroscopy. Opt. Express **23**, 14472 (2015). https://doi.org/10.1364/OE.23.014472
39. A. Cygan, P. Wcisło, S. Wójtewicz, G. Kowzan, M. Zaborowski, D. Charczun, K. Bielska, R.S. Trawiński, R. Ciuryło, P. Masłowski, D. Lisak, High-accuracy and wide dynamic range frequency-based dispersion spectroscopy in an optical cavity. Opt. Express **27**, 21810 (2019). https://doi.org/10.1364/OE.27.021810
40. B. Henderson, A. Khodabakhsh, M. Metsälä, I. Ventrillard, F.M. Schmidt, D. Romanini, G.A.D. Ritchie, S. te Lintel Hekkert, R. Briot, T. Risby, N. Marczin, F.J.M. Harren, S.M. Cristescu, Laser spectroscopy for breath analysis: towards clinical implementation. Appl. Phys. B (2018). https://doi.org/10.1007/s00340-018-7030-x
41. E. Kerstel, L. Gianfrani, Advances in laser-based isotope ratio measurements: selected applications. Appl. Phys. B **92**, 439 (2008). https://doi.org/10.1007/s00340-008-3128-x
42. I. Galli, S. Bartalini, R. Ballerini, M. Barucci, P. Cancio, M.D. Pas, G. Giusfredi, D. Mazzotti, N. Akikusa, P. De Natale, Spectroscopic detection of radiocarbon dioxide at parts-per-quadrillion sensitivity. Optica **3**, 385 (2016). https://doi.org/10.1364/OPTICA.3.000385
43. G. Berden, R. Peeters, G. Meijer, Cavity ring-down spectroscopy: experimental schemes and applications. Int. Rev. Phys. Chem. **19**, 565 (2000). https://doi.org/10.1080/014423500750040627
44. M. Mazurenka, A.J. Orr-Ewing, R. Peverall, G.A.D. Ritchie, Cavity ring-down and cavity enhanced spectroscopy using diode lasers. Annu. Rep. Prog. Chem. Sect. C Phys. Chem. **101**, 100 (2005). https://doi.org/10.1039/B408909J
45. A. Maity, S. Maithani, M. Pradhan, Cavity ring-down spectroscopy: recent technological advancements, techniques, and applications. Anal. Chem. **93**, 388 (2021). https://doi.org/10.1021/acs.analchem.0c04329
46. G. Berden, R. Engeln, Cavity Ring-Down Spectroscopy: Techniques and Applications (Wiley, Blackwell Publishing, 2009). https://doi.org/10.1002/9781444308259
47. H. Naus, I.H.M. van Stokkum, W. Hogervorst, W. Ubachs, Quantitative analysis of decay transients applied to a multimode pulsed cavity ringdown experiment. Appl. Opt. **40**, 4416 (2001). https://doi.org/10.1364/AO.40.004416
48. J.W. Hahn, Y.S. Yoo, J.Y. Lee, J.W. Kim, H.-W. Lee, Cavity ringdown spectroscopy with a continuous-wave laser: calculation of coupling efficiency and a new spectrometer design. Appl. Opt. **38**, 1859 (1999). https://doi.org/10.1364/AO.38.001859
49. R.W.P. Drever, J.L. Hall, F.V. Kowalski, J. Hough, G.M. Ford, A.J. Munley, H. Ward, Laser phase and frequency stabilization using an optical resonator. Appl. Phys. B **31**, 97 (1983). https://doi.org/10.1007/BF00702605
50. B. Dahmani, L. Hollberg, R. Drullinger, Frequency stabilization of semiconductor lasers by resonant optical feedback. Opt. Lett. **12**, 876 (1987). https://doi.org/10.1364/OL.12.000876
51. T.G. Spence, C.C. Harb, B.A. Paldus, R.N. Zare, B. Willke, R.L. Byer, A laser-locked cavity ring-down spectrometer employing an analog detection scheme. Rev. Sci. Instrum. **71**, 347 (2000). https://doi.org/10.1063/1.1150206
52. N.J. van Leeuwen, J.C. Diettrich, A.C. Wilson, Periodically locked continuous-wave cavity ringdown spectroscopy. Appl. Opt. **42**, 3670 (2003). https://doi.org/10.1364/AO.42.003670
53. R.Z. Martínez, M. Metsälä, O. Vaittinen, T. Lantta, L. Halonen, Laser-locked, high-repetition-rate cavity ringdown spectrometer. J. Opt. Soc. Am. B **23**, 727 (2006). https://doi.org/10.1364/JOSAB.23.000727
54. G.-W. Truong, K. Douglass, S. Maxwell, R. van Zee, D. Plusquellic, J. Hodges, D. Long, Frequency-agile, rapid scanning spectroscopy. Nat. Photonics **7**, 532 (2013). https://doi.org/10.1038/nphoton.2013.98
55. D. Long, G.-W. Truong, R. van Zee, D. Plusquellic, J. Hodges, Frequency-agile, rapid scanning spectroscopy: absorption sensitivity of 2×10^{-12} cm^{-1}Hz$^{-1/2}$ with a tunable diode laser. Appl. Phys. B **114**, 489 (2014). https://doi.org/10.1007/s00340-013-5548-5
56. H. Pan, C.-F. Cheng, Y.R. Sun, B. Gao, A.-W. Liu, S.-M. Hu, Laser-locked, continuously tunable high resolution cavity ring-down spectrometer. Rev. Sci. Instrum. **82**, 103110 (2011). https://doi.org/10.1063/1.3655445
57. J. Burkart, D. Romanini, S. Kassi, Optical feedback stabilized laser tuned by single-sideband modulation. Opt. Lett. **38**, 2062 (2013). https://doi.org/10.1364/OL.38.002062

58. J. Burkart, D. Romanini, S. Kassi, Optical feedback frequency stabilized cavity ring-down spectroscopy. Opt. Lett. **39**, 4695 (2014). https://doi.org/10.1364/OL.39.004695
59. V. Motto-Ros, J. Morville, P. Rairoux, Mode-by-mode optical feedback: cavity ringdown spectroscopy. Appl. Phys. B **87**, 531 (2007). https://doi.org/10.1007/s00340-007-2618-6
60. H. Huang, K.K. Lehmann, Sensitivity limits of continuous wave cavity ring-down spectroscopy. J. Phys. Chem. A **117**, 13399 (2013). https://doi.org/10.1021/jp406691e
61. J.T. Hodges, H.P. Layer, W.W. Miller, G.E. Scace, Frequency-stabilized single-mode cavity ring-down apparatus for high-resolution absorption spectroscopy. Rev. Sci. Instrum. **75**, 849 (2004). https://doi.org/10.1063/1.1666984
62. D. Long, A. Cygan, R. van Zee, M. Okumura, C. Miller, D. Lisak, J. Hodges, Frequency-stabilized cavity ring-down spectroscopy. Chem. Phys. Lett. **536**, 1 (2012). https://doi.org/10.1016/j.cplett.2012.03.035
63. A. Cygan, D. Lisak, P. Masowski, K. Bielska, S. Wójtewicz, J. Domysławska, R.S. Trawiński, R. Ciuryło, H. Abe, J.T. Hodges, Pound–Drever–Hall-locked, frequency-stabilized cavity ring-down spectrometer. Rev. Sci. Instrum. **82**, 063107 (2011). https://doi.org/10.1063/1.3595680
64. A. Cygan, D. Lisak, S. Wójtewicz, J. Domysławska, J.T. Hodges, R.S. Trawiński, R. Ciuryło, High-signal-to-noise-ratio laser technique for accurate measurements of spectral line parameters. Phys. Rev. A **85**, 022508 (2012). https://doi.org/10.1103/PhysRevA.85.022508
65. J.T. Hodges, D. Lisak, Frequency-stabilized cavity ring-down spectrometer for high-sensitivity measurements of water vapor concentration. Appl. Phys. B **85**, 375 (2006). https://doi.org/10.1007/s00340-006-2411-y
66. D. Lisak, J.T. Hodges, R. Ciuryło, Comparison of semiclassical line-shape models to rovibrational H_2O spectra measured by frequency-stabilized cavity ring-down spectroscopy. Phys. Rev. A **73**, 012507 (2006). https://doi.org/10.1103/PhysRevA.73.012507
67. D.A. Long, K. Bielska, D. Lisak, D.K. Havey, M. Okumura, C.E. Miller, J.T. Hodges, The air-broadened, near-infrared CO_2 line shape in the spectrally isolated regime: evidence of simultaneous Dicke narrowing and speed dependence. J. Chem. Phys. **135**, 064308 (2011). https://doi.org/10.1063/1.3624527
68. D. Lisak, D.K. Havey, J.T. Hodges, Spectroscopic line parameters of water vapor for rotation-vibration transitions near 7180 cm^{-1}. Phys. Rev. A **79**, 052507 (2009). https://doi.org/10.1103/PhysRevA.79.052507
69. T.W. Hänsch, Nobel lecture: passion for precision. Rev. Mod. Phys. **78**, 1297 (2006). https://doi.org/10.1103/RevModPhys.78.1297
70. J.L. Hall, Nobel lecture: defining and measuring optical frequencies. Rev. Mod. Phys. **78**, 1279 (2006). https://doi.org/10.1103/RevModPhys.78.1279
71. J. Domysławska, S. Wójtewicz, D. Lisak, A. Cygan, F. Ozimek, K. Stec, C. Radzewicz, R.S. Trawiński, R. Ciuryło, Cavity ring-down spectroscopy of the oxygen B-band with absolute frequency reference to the optical frequency comb. J. Chem. Phys. **136**, 024201 (2012). https://doi.org/10.1063/1.3675903
72. G.-W. Truong, D.A. Long, A. Cygan, D. Lisak, R.D. van Zee, J.T. Hodges, Comb-linked, cavity ring-down spectroscopy for measurements of molecular transition frequencies at the kHz-level. J. Chem. Phys. **138**, 094201 (2013). https://doi.org/10.1063/1.4792372
73. D. Gatti, T. Sala, R. Gotti, L. Cocola, L. Poletto, M. Prevedelli, P. Laporta, M. Marangoni, Comb-locked cavity ring-down spectrometer. J. Chem. Phys. **142**, 074201 (2015). https://doi.org/10.1063/1.4907939
74. J. Wang, Y.R. Sun, L.-G. Tao, A.-W. Liu, S.-M. Hu, Communication: molecular near-infrared transitions determined with sub-kHz accuracy. J. Chem. Phys. **147**, 091103 (2017). https://doi.org/10.1063/1.4998763
75. C.-F. Cheng, J. Wang, Y.R. Sun, Y. Tan, P. Kang, S.-M. Hu, Doppler broadening thermometry based on cavity ring-down spectroscopy. Metrologia **52**, S385 (2015). https://doi.org/10.1088/0026-1394/52/5/S385
76. L. Gianfrani, Linking the thermodynamic temperature to an optical frequency: recent advances in Doppler broadening thermometry. Philos. Trans. R. Soc. A Math. Phys. Eng. Sci. **374**, 20150047 (2016). https://doi.org/10.1098/rsta.2015.0047
77. R. Gotti, L. Moretti, D. Gatti, A. Castrillo, G. Galzerano, P. Laporta, L. Gianfrani, M. Marangoni, Cavity-ring-down doppler-broadening primary thermometry. Phys. Rev. A **97**, 012512 (2018). https://doi.org/10.1103/PhysRevA.97.012512

78. G. Casa, A. Castrillo, G. Galzerano, R. Wehr, A. Merlone, D. Di Serafino, P. Laporta, L. Gianfrani, Primary gas thermometry by means of laser-absorption spectroscopy: determination of the Boltzmann constant. Phys. Rev. Lett. **100**, 200801 (2008). https://doi.org/10.1103/PhysRevLett.100.200801
79. S. Kassi, T. Stoltmann, M. Casado, M. Daëron, A. Campargue, Lamb dip CRDS of highly saturated transitions of water near 1.4 μm. J. Chem. Phys. **148**, 054201 (2018). https://doi.org/10.1063/1.5010957
80. O.L. Polyansky, A.A. Kyuberis, N.F. Zobov, J. Tennyson, S.N. Yurchenko, L. Lodi, ExoMol molecular line lists XXX: a complete high-accuracy line list for water. Mon. Not. R. Astron. Soc. **480**, 2597 (2018). https://doi.org/10.1093/mnras/sty1877
81. F. Riehle, P. Gill, F. Arias, L. Robertsson, The CIPM list of recommended frequency standard values: guidelines and procedures. Metrologia **55**, 188 (2018). https://doi.org/10.1088/1681-7575/aaa302
82. E. Fasci, H. Dinesan, L. Moretti, A. Merlone, A. Castrillo, L. Gianfrani, Dual-laser frequency-stabilized cavity ring-down spectroscopy for water vapor density measurements. Metrologia **55**, 662 (2018). https://doi.org/10.1088/1681-7575/aad15e
83. E. Fasci, M.A. Khan, V. D'Agostino, S. Gravina, V. Fernicola, L. Gianfrani, A. Castrillo, Water vapor concentration measurements in high purity gases by means of comb assisted cavity ring down spectroscopy. Sens. Actuators A **362**, 114632 (2023). https://doi.org/10.1016/j.sna.2023.114632
84. E. Fasci, A. Castrillo, H. Dinesan, S. Gravina, L. Moretti, L. Gianfrani, Precision spectroscopy of HD at 1.38 μm. Phys. Rev. A **98**, 22516 (2018). https://doi.org/10.1103/PhysRevA.98.022516
85. E. Fasci, T.A. Odintsova, A. Castrillo, M.D. De Vizia, A. Merlone, F. Bertiglia, L. Moretti, L. Gianfrani, Dual-laser absorption spectroscopy of C_2H_2 at 1.4μm. Phys. Rev. A **93**, 042513 (2016). https://doi.org/10.1103/PhysRevA.93.042513
86. A. Castrillo, E. Fasci, G. Galzerano, G. Casa, P. Laporta, L. Gianfrani, Offset-frequency locking of extended-cavity diode lasers for precision spectroscopy of water at 1.38 μm. Opt. Express **18**, 21851 (2010). https://doi.org/10.1364/OE.18.021851
87. O. Votava, M. Mašát, A.E. Parker, C. Jain, C. Fittschen, Microcontroller based resonance tracking unit for time resolved continuous wave cavity-ringdown spectroscopy measurements. Rev. Sci. Instrum. **83**, 043110 (2012). https://doi.org/10.1063/1.3698061
88. Z.D. Reed, D.A. Long, H. Fleurbaey, J.T. Hodges, SI-traceable molecular transition frequency measurements at the 10^{-12} relative uncertainty level. Optica **7**, 1209 (2020). https://doi.org/10.1364/OPTICA.395943
89. R. Gotti, M. Prevedelli, S. Kassi, M. Marangoni, D. Romanini, Feed-forward coherent link from a comb to a diode laser: application to widely tunable cavity ring-down spectroscopy. J. Chem. Phys. **148**, 054202 (2018). https://doi.org/10.1063/1.5018611
90. O. Votava, S. Kassi, A. Campargue, D. Romanini, Comb coherence-transfer and cavity ring-down saturation spectroscopy around 1.65 μm: kHz-accurate frequencies of transitions in the $2\nu_3$ band of $^{12}CH_4$. Phys. Chem. Chem. Phys. **24**, 4157 (2022). https://doi.org/10.1039/D1CP04989E
91. H. Fleurbaey, P. Čermák, A. Campargue, S. Kassi, D. Romanini, O. Votava, D. Mondelain, $^{12}CO_2$ transition frequencies with kHz-accuracy by saturation spectroscopy in the 1.99–2.09 μm region. Phys. Chem. Chem. Phys. **25**, 16319 (2023). https://doi.org/10.1039/D3CP01603J
92. H.R. Gray, R.M. Whitley, C.R. Stroud, Coherent trapping of atomic populations. Opt. Lett. **3**, 218 (1978). https://doi.org/10.1364/OL.3.000218
93. M. Fleischhauer, A. Imamoglu, J.P. Marangos, Electromagnetically induced transparency: optics in coherent media. Rev. Mod. Phys. **77**, 633 (2005). https://doi.org/10.1103/RevModPhys.77.633
94. T. Hänsch, R. Keil, A. Schabert, C. Schmelzer, P. Toschek, Interaction of laser light waves by dynamic stark splitting. Zeitschrift für Phys. A Hadron. Nucl. **226**, 293 (1969). https://doi.org/10.1007/BF01392091
95. M.E. Kaminsky, R.T. Hawkins, F.V. Kowalski, A.L. Schawlow, Identification of absorption lines by modulated lower-level population: spectrum of Na_2. Phys. Rev. Lett. **36**, 671 (1976). https://doi.org/10.1103/PhysRevLett.36.671
96. A. Callegari, H.K. Srivastava, U. Merker, K.K. Lehmann, G. Scoles, M.J. Davis, Eigenstate resolved infrared-infrared double-resonance study of intramolecular vibrational relaxation in benzene: first overtone of the CH stretch. J. Chem. Phys. **106**, 432 (1997). https://doi.org/10.1063/1.473205
97. M. Siltanen, M. Metsälä, M. Vainio, L. Halonen, Experimental observation and analysis of the $3\nu_1\,(\Sigma_g)$ stretching vibrational state of acetylene using continuous-wave infrared stimulated emission. J. Chem. Phys. **139**, 054201 (2013). https://doi.org/10.1063/1.4816524

98. W. Demtröder, *Laser Spectroscopy*, 4th edn. (Springer, Berlin, 2008). https://doi.org/10.1007/978-3-540-73418-5
99. C.-L. Hu, J. Wang, T.-P. Hua, A.-W. Liu, Y.R. Sun, S.-M. Hu, Comb-locked cavity-assisted double-resonance molecular spectroscopy based on diode lasers. Rev. Sci. Instrum **92**, 073003 (2021). https://pubs.aip.org/aip/rsi/article/1030704
100. J. Karhu, J. Nauta, M. Vainio, M. Metsälä, S. Hoekstra, L. Halonen, Double resonant absorption measurement of acetylene symmetric vibrational states probed with cavity ring down spectroscopy. J. Chem. Phys. **144**, 244201 (2016). https://doi.org/10.1063/1.4954159
101. J. Karhu, K. Lehmann, M. Vainio, M. Metsälä, L. Halonen, Step-modulated decay cavity ring-down detection for double resonance spectroscopy. Opt. Express **26**, 29086 (2018). https://doi.org/10.1364/OE.26.029086
102. A. Foltynowicz, L. Rutkowski, I. Silander, A.C. Johansson, V. Silva de Oliveira, O. Axner, G. Soboń, T. Martynkien, P. Mergo, K.K. Lehmann, Sub-Doppler double-resonance spectroscopy of methane using a frequency comb probe. Phys. Rev. Lett. **126**, 063001 (2021). https://doi.org/10.1103/PhysRevLett.126.063001
103. Y.-D. Tan, C.-F. Cheng, Y. Tan, S.-M. Hu, Mid-infrared-near-infrared double-resonance spectroscopy of molecules with kilohertz accuracy. Opt. Lett **49**, 1109 (2024). https://opg.optica.org/ol/abstract.cfm?URI=ol-49-5-1109
104. C.-L. Hu, V.I. Perevalov, C.-F. Cheng, T.-P. Hua, S.-M. Hu, Optical-optical double-resonance absorption spectroscopy of molecules with kHz accuracy. J. Phys. Chem. Lett. **11**, 8973 (2020). https://doi.org/10.1021/acs.jpclett.0c02136
105. W.E. Perreault, H. Zhou, N. Mukherjee, R.N. Zare, Harnessing the power of adiabatic curve crossing to populate the highly vibrationally excited H_2 ($v = 7$, $j = 0$) level. Phys. Rev. Lett. **124**, 163202 (2020). https://doi.org/10.1103/PhysRevLett.124.163202
106. Y.D. Tan, C.F. Cheng, D. Sheng, S.M. Hu, Detection of radiocarbon dioxide with double-resonance absorption spectroscopy. Chin. J. Chem. Phys. **34**, 373 (2021). https://doi.org/10.1063/1674-0068/cjcp2103045
107. A.D. McCartt, J. Jiang, Room-temperature optical detection of $^{14}CO_2$ below the natural abundance with two-color cavity ring-down spectroscopy. ACS Sens. **7**, 3258 (2022). https://doi.org/10.1021/acssensors.2c01253
108. M.-Y. Yu, Q.-H. Liu, C.-F. Cheng, S.-M. Hu, Cavity-enhanced double resonance spectroscopy of HD. Mol. Phys. **121**, e2127382 (2023). https://doi.org/10.1080/00268976.2022.2127382
109. M.S. Safronova, D. Budker, D. DeMille, D.F.J. Kimball, A. Derevianko, C.W. Clark, Search for new physics with atoms and molecules. Rev. Mod. Phys. **90**, 025008 (2018). https://doi.org/10.1103/RevModPhys.90.025008
110. G. Zhao, D.M. Bailey, A.J. Fleisher, J.T. Hodges, K.K. Lehmann, Doppler-free two-photon cavity ring-down spectroscopy of a nitrous oxide (N_2O) vibrational overtone transition. Phys. Rev. A **101**, 062509 (2020). https://doi.org/10.1103/PhysRevA.101.062509
111. L.-S. Ma, J. Ye, P. Dubé, J. Hall, Ultrasensitive frequency-modulation spectroscopy enhanced by a high-finesse optical cavity: theory and application to overtone transitions of C_2H_2 and C_2HD. J. Opt. Soc. Am. B **16**, 2255 (1999). https://doi.org/10.1364/JOSAB.16.002255
112. O. Axner, W. Ma, A. Foltynowicz, Sub-Doppler dispersion and noise-immune cavity-enhanced optical heterodyne molecular spectroscopy revised. J. Opt. Soc. Am. B **25**, 1166 (2008). https://doi.org/10.1364/JOSAB.25.001166
113. A. Foltynowicz, W. Ma, F. Schmidt, O. Axner, Doppler-broadened noise-immune cavity-enhanced optical heterodyne molecular spectrometry signals from optically saturated transitions under low pressure conditions. J. Opt. Soc. Am. B **25**, 1156 (2008). https://doi.org/10.1364/JOSAB.25.001156
114. A. Foltynowicz, F. Schmidt, W. Ma, O. Axner, Noise-immune cavity-enhanced optical heterodyne molecular spectroscopy: current status and future potential. Appl. Phys. B **92**, 313 (2008). https://doi.org/10.1007/s00340-008-3126-z
115. P. Ehlers, I. Silander, J. Wang, O. Axner, Fiber-laser-based noise-immune cavity-enhanced optical heterodyne molecular spectrometry instrumentation for Doppler-broadened detection in the 10^{-12} cm^{-1} $Hz^{-1/2}$ region. J. Opt. Soc. Am. B **29**, 1305 (2012). https://doi.org/10.1364/JOSAB.29.001305
116. O. Axner, P. Ehlers, A. Foltynowicz, I. Silander, J. Wang, NICE-OHMS-frequency modulation cavity-enhanced spectroscopy-principles and performance, in *Cavity-Enhanced Spectroscopy and Sensing,*

Springer Series in Optical Sciences, Chap. 6 (Springer, 2014), pp. 211–251. https://doi.org/10.1007/978-3-642-40003-2_6
117. M. Diouf, Saturated ultra-precision spectroscopy of water and HD with NICE-OHMS. Ph.D. thesis, Vrije Universiteit, Amsterdam (2023). https://research.vu.nl/en/publications/saturated-ultra-precision-spectroscopy-of-water-and-hd-with-nice-
118. N. van Leeuwen, A. Wilson, Measurement of pressure-broadened, ultraweak transitions with noise-immune cavity-enhanced optical heterodyne molecular spectroscopy. J. Opt. Soc. Am. B **21**, 1713 (2004). https://doi.org/10.1364/JOSAB.21.001713
119. A. Foltynowicz, W. Ma, F. Schmidt, O. Axner, Wavelength-modulated noise-immune cavity-enhanced optical heterodyne molecular spectroscopy signal line shapes in the Doppler limit. J. Opt. Soc. Am. B **26**, 1384 (2009). https://doi.org/10.1364/JOSAB.26.001384
120. A. Foltynowicz, I. Silander, O. Axner, Reduction of background signals in fiber-based NICE-OHMS. J. Opt. Soc. Am. B **28**, 2797 (2011). https://doi.org/10.1364/JOSAB.28.002797
121. P. Ehlers, A.C. Johansson, I. Silander, A. Foltynowicz, O. Axner, Use of etalon-immune distances to reduce the influence of background signals in frequency-modulation spectroscopy and noise-immune cavity-enhanced optical heterodyne molecular spectroscopy. J. Opt. Soc. Am. B **31**, 2938 (2014). https://doi.org/10.1364/JOSAB.31.002938
122. M.L. Diouf, F.M.J. Cozijn, W. Ubachs, Hyperfine structure in a vibrational quadrupole transition of ortho-H_2. Mol. Phys. (2024). https://doi.org/10.1080/00268976.2024.2304101
123. T.-P. Hua, Y.R. Sun, S.-M. Hu, Dispersion-like lineshape observed in cavity-enhanced saturation spectroscopy of HD at 1.4 μm. Opt. Lett. **45**, 4863 (2020). https://doi.org/10.1364/OL.401879
124. G. Zhao, T. Hausmaninger, W. Ma, O. Axner, Shot-noise-limited doppler-broadened noise-immune cavity-enhanced optical heterodyne molecular spectrometry. Opt. Lett. **43**, 715 (2018). https://doi.org/10.1364/OL.43.000715
125. M.L. Diouf, F.M.J. Cozijn, K.-F. Lai, E.J. Salumbides, W. Ubachs, Lamb-peak spectrum of the HD (2–0) P(1) line. Phys. Rev. Res. **2**, 023209 (2020). https://doi.org/10.1103/PhysRevResearch.2.023209
126. A. Foltynowicz, W. Ma, O. Axner, Characterization of fiber-laser-based sub-Doppler NICE-OHMS for quantitative trace gas detection. Opt. Express **16**, 14689 (2008). https://doi.org/10.1364/OE.16.014689
127. M.L. Diouf, R. Tóbiás, T.S. van der Schaaf, F.M.J. Cozijn, E.J. Salumbides, A.G. Császár, W. Ubachs, Ultraprecise relative energies in the (2 0 0) vibrational band of $H_2^{16}O$. Mol. Phys. **120**, e2050430 (2022). https://doi.org/10.1080/00268976.2022.2050430
128. M. Melosso, M.L. Diouf, L. Bizzocchi, M.E. Harding, F.M.J. Cozijn, C. Puzzarini, W. Ubachs, Hyperfine-resolved near-infrared spectra of $H_2^{17}O$. J. Phys. Chem. A **125**, 7884 (2021). https://doi.org/10.1021/acs.jpca.1c05681
129. F.M.J. Cozijn, P. Dupré, E.J. Salumbides, K.S.E. Eikema, W. Ubachs, Sub-Doppler frequency metrology in HD for tests of fundamental physics. Phys. Rev. Lett. **120**, 153002 (2018). https://doi.org/10.1103/PhysRevLett.120.153002
130. R.G. DeVoe, R.G. Brewer, Laser-frequency division and stabilization. Phys. Rev. A **30**, 2827 (1984). https://doi.org/10.1103/PhysRevA.30.2827
131. C. Ishibashi, H. Sasada, Highly sensitive cavity-enhanced sub-Doppler spectroscopy of a molecular overtone band with a 1.66 μm tunable diode laser. Jpn. J. Appl. Phys. **38**, 920 (1999). https://doi.org/10.1143/JJAP.38.920
132. A. Foltynowicz, J. Wang, P. Ehlers, O. Axner, Distributed-feedback-laser-based NICE-OHMS in the pressure-broadened regime. Opt. Express **18**, 18580 (2010). https://doi.org/10.1364/OE.18.018580
133. M. Taubman, T. Myers, B. Cannon, R. Williams, Stabilization, injection and control of quantum cascade lasers, and their application to chemical sensing in the infrared. Spectrochim. Acta A **60**, 3457 (2004). https://doi.org/10.1016/j.saa.2003.12.057
134. F. Schmidt, A. Foltynowicz, W. Ma, T. Lock, O. Axner, Doppler-broadened fiber-laser-based NICE-OHMS—improved detectability. Opt. Express **15**, 10822 (2007). https://doi.org/10.1364/OE.15.010822
135. F. Schmidt, A. Foltynowicz, W. Ma, T. Lock, O. Axner, Fiber-laser-based noise-immune cavity-enhanced optical heterodyne molecular spectrometry for Doppler-broadened detection of C_2H_2 in the parts per trillion range. J. Opt. Soc. Am. B **24**, 1392 (2007). https://doi.org/10.1364/JOSAB.24.001392

136. M. Porambo, B. Siller, J. Pearson, B. McCall, Broadly tunable mid-infrared noise-immune cavity-enhanced optical heterodyne molecular spectrometer. Opt. Lett. **37**, 4422 (2012). https://doi.org/10.1364/OL.37.004422
137. I. Silander, T. Hausmaninger, W. Ma, F. Harren, O. Axner, Doppler-broadened mid-infrared noise-immune cavity-enhanced optical heterodyne molecular spectrometry based on an optical parametric oscillator for trace gas detection. Opt. Lett. **40**, 439 (2015). https://doi.org/10.1364/OL.40.000439
138. P. Ehlers, J. Junyang, I. Silander, O. Axner, Doppler broadened NICE-OHMS beyond the triplet formalism: assessment of optimum modulation index. J. Opt. Soc. Am. B **31**, 1499 (2014). https://doi.org/10.1364/JOSAB.31.001499
139. W. Ma, A. Foltynowicz, O. Axner, Theoretical description of Doppler-broadened noise-immune cavity-enhanced optical heterodyne molecular spectroscopy under optically saturated conditions. J. Opt. Soc. Am. B **25**, 1144 (2007). https://doi.org/10.1364/JOSAB.25.001144
140. I. Silander, T. Hausmaninger, W. Ma, P. Ehlers, O. Axner, Doppler-broadened noise-immune cavity-enhanced optical heterodyne molecular spectrometry down to 4×10^{-13} cm^{-1} $\mathrm{Hz}^{-1/2}$: implementation of a 50,000 finesse cavity. Opt. Lett. **40**, 2004 (2015). https://doi.org/10.1364/OL.40.002004
141. A. Khodabakhsh, A.C. Johansson, A. Foltynowicz, Noise-immune cavity-enhanced optical frequency comb spectroscopy: a sensitive technique for high-resolution broadband molecular detection. Appl. Phys. B **119**, 87–96 (2015). https://doi.org/10.1007/s00340-015-6010-7
142. G. Zhao, T. Hausmaninger, F.M. Schmidt, W. Ma, O. Axner, High-resolution trace gas detection by sub-Doppler noise-immune cavity-enhanced optical heterodyne molecular spectrometry: application to detection of acetylene in human breath. Opt. Express **27**, 17940 (2019). https://doi.org/10.1364/OE.27.017940
143. T. Hausmaninger, G. Zhao, W. Ma, O. Axner, Depletion of the vibrational ground state of CH_4 in absorption spectroscopy at 3.4 μm in N_2 and air in the 1–100 Torr range. J. Quant. Spectrosc. Radiat. Transf. **205**, 59 (2018)
144. E.A. Curtis, G.P. Barwood, G. Huang, C.S. Edwards, B. Gieseking, P.J. Brewer, Ultra-high-finesse NICE-OHMS spectroscopy at 1532 nm for calibrated online ammonia detection. J. Opt. Soc. Am. B **34**, 950 (2017). https://doi.org/10.1364/JOSAB.34.000950
145. C. Bell, J.-P. van Helden, T.P.J. Blaikie, G. Hancock, N. van Leeuwen, R. Peverall, G. Ritchie, Noise-immune cavity-enhanced optical heterodyne detection of HO_2 in the near-infrared range. J. Phys. Chem. A **116**, 5090 (2012). https://doi.org/10.1021/jp301038r
146. T.L. Chen, Y.W. Liu, Noise-immune cavity-enhanced optical heterodyne molecular spectrometry on N_2O 1.283 μm transition based on a quantum-dot external-cavity diode laser. Opt. Lett. **40**, 4352 (2015). https://doi.org/10.1364/OL.40.004352
147. B. Siller, M. Porambo, A. Mills, B. McCall, Noise immune cavity enhanced optical heterodyne velocity modulation spectroscopy. Opt. Express **19**, 24822 (2011). https://doi.org/10.1364/OE.19.024822
148. S. Saraf, P. Berceau, A. Stochino, R. Byer, J. Lipa, Ultrastable frequency reference at 1.56 μm using a $^{12}C^{16}O$ molecular overtone transition with the noise-immune cavity-enhanced optical heterodyne molecular spectroscopy method. Opt. Lett. **41**, 2189 (2016). https://doi.org/10.1364/OL.41.002189
149. H. Dinesan, E. Fasci, A. Castrillo, L. Gianfrani, Absolute frequency stabilization of an extended-cavity diode laser by means of noise-immune cavity-enhanced optical heterodyne molecular spectroscopy. Opt. Lett. **39**, 2198 (2014). https://doi.org/10.1364/OL.39.002198
150. H. Dinesan, E. Fasci, A. d'Addio, A. Castrillo, L. Gianfrani, Characterization of the frequency stability of an optical frequency standard at 1.39 μm based upon noise-immune cavity-enhanced optical heterodyne molecular spectroscopy. Opt. Express **23**, 1757 (2015). https://doi.org/10.1364/OE.23.001757
151. Y. Zhou, J. Liu, S. Guo, G. Zhao, W. Ma, Z. Cao, L. Dong, L. Zhang, W. Yin, Y. Wu, L. Xiao, O. Axner, S. Jia, Laser frequency stabilization based on a universal sub-Doppler NICE-OHMS instrumentation for the potential application in atmospheric lidar. Atmos. Meas. Tech. **12**, 1807 (2019. https://amt.copernicus.org/articles/12/1807/2019/
152. R. Tobias, T. Furtenbacher, I. Semko, A.G. Csazar, M.L. Diouf, F.M.J. Cozijn, J.M. Staa, E.J. Salumbides, W. Ubachs, Spectroscopic-network-assisted precision spectroscopy and its application to water. Nat. Commun. **11**, 1709 (2020). https://doi.org/10.1038/s41467-020-15430-6
153. I.E. Gordon, L.S. Rothman, R.J. Hargreaves, R. Hashemi, E.V. Karlovets, F.M. Skinner, E.K. Conway, C. Hill, R.V. Kochanov, Y. Tan, P. Wcisło, A.A. Finenko, K. Nelson, P.F. Bernath, M. Birk, V. Boudon,

A. Campargue, K.V. Chance, A. Coustenis, B.J. Drouin, J.M. Flaud, R.R. Gamache, J.T. Hodges, D. Jacquemart, E.J. Mlawer, A.V. Nikitin, V.I. Perevalov, M. Rotger, J. Tennyson, G.C. Toon, H. Tran, V.G. Tyuterev, E.M. Adkins, A. Baker, A. Barbe, E. Canè, A.G. Császár, A. Dudaryonok, O. Egorov, A.J. Fleisher, H. Fleurbaey, A. Foltynowicz, T. Furtenbacher, J.J. Harrison, J.M. Hartmann, V.M. Horneman, X. Huang, T. Karman, J. Karns, S. Kassi, I. Kleiner, V. Kofman, F. Kwabia-Tchana, N.N. Lavrentieva, T.J. Lee, D.A. Long, A.A. Lukashevskaya, O.M. Lyulin, V.Y. Makhnev, W. Matt, S.T. Massie, M. Melosso, S.N. Mikhailenko, D. Mondelain, H.S.P. Müller, O. V. Naumenko, A. Perrin, O.L. Polyansky, E. Raddaoui, P.L. Raston, Z.D. Reed, M. Rey, C. Richard, R. Tóbiás, I. Sadiek, D.W. Schwenke, E. Starikova, K. Sung, F. Tamassia, S.A. Tashkun, J. Vander Auwera, I.A. Vasilenko, A.A. Vigasin, G.L. Villanueva, B. Vispoel, G. Wagner, A. Yachmenev, S.N. Yurchenko, The HITRAN2020 molecular spectroscopic database. J. Quant. Spectrosc. Radiat. Transf. **277**, 107949 (2022). https://doi.org/10.1016/j.jqsrt.2021.107949

154. R.A. Toth, Measurements of positions, strengths and self-broadened widths of $H_2{}^{16}O$ from 2900 to 8000 cm^{-1}: line strength analysis of the 2nd triad bands. J. Quant. Spectrosc. Radiat. Transf. **94**, 51 (2005). https://doi.org/10.1016/j.jqsrt.2004.08.042
155. O. Leshchishina, S. Mikhailenko, D. Mondelain, S. Kassi, A. Campargue, CRDS of water vapor at 0.1 Torr between 6886 and 7406 cm^{-1}. J. Quant. Spectrosc. Radiat. Transf. **113**, 2155 (2012). https://doi.org/10.1016/j.jqsrt.2012.06.026
156. A. Campargue, S. Mikhailenko, B.G. Lohan, E. Karlovets, D. Mondelain, S. Kassi, The absorption spectrum of water vapor in the 1.25 μm atmospheric window (7911–8337 cm^{-1}). J. Quant. Spectrosc. Radiat. Transf. **157**, 135 (2015). https://doi.org/10.1016/j.jqsrt.2015.02.011
157. A. Campargue, S. Kassi, A. Yachmenev, A.A. Kyuberis, J. Küpper, S.N. Yurchenko, Observation of electric-quadrupole infrared transitions in water vapor. Phys. Rev. Res. **2**, 023091 (2020). https://doi.org/10.1103/PhysRevResearch.2.023091
158. A. Gambetta, E. Fasci, A. Castrillo, M. Marangoni, G. Galzerano, G. Casa, P. Laporta, L. Gianfrani, Frequency metrology in the near-infrared spectrum of $H_2{}^{17}O$ and $H_2{}^{18}O$ molecules: testing a new inversion method for retrieval of energy levels. New J. Phys. **12**, 103006 (2010). https://doi.org/10.1088/1367-2630/12/10/103006
159. J. Chen, T.-P. Hua, L.-G. Tao, Y.R. Sun, A.-W. Liu, S.-M. Hu, Absolute frequencies of water lines near 790 nm with 10^{-11} accuracy. J. Quant. Spectrosc. Radiat. Transf. **205**, 91 (2018). https://doi.org/10.1016/j.jqsrt.2017.10.009
160. M.L. Diouf, R. Tóbiás, I. Simkó, F.M.J. Cozijn, E.J. Salumbides, W. Ubachs, A.G. Császár, Network-based design of near-infrared Lamb-dip experiments and the determination of pure rotational energies of $H_2^{18}O$ at kHz accuracy. J. Phys. Chem. Ref. Data **50**, 023106 (2021). https://doi.org/10.1063/5.0052744
161. A. Miani, J. Tennyson, Can ortho-para transitions for water be observed? J. Chem. Phys. **120**, 2732 (2004). https://doi.org/10.1063/1.1633261
162. S.G. Kukolich, Measurement of the molecular g values in H_2O and D_2O and hyperfine structure in H_2O. J. Chem. Phys. **50**, 3751 (1969). https://doi.org/10.1063/1.1671623
163. G.Y. Golubiatnikov, V.N. Markov, A. Guarnieri, R. Knochel, Hyperfine structure of $H_2{}^{16}O$ and $H_2{}^{18}O$ measured by Lamb-dip technique in the 180–560 GHz frequency range. J. Mol. Spectrosc. **240**, 191 (2006). https://doi.org/10.1016/j.jms.2006.09.012
164. E. Mátyus, G. Czakó, A.G. Császár, Toward black-box-type full- and reduced-dimensional variational (ro)vibrational computations. J. Chem. Phys. **130**, 134112 (2009). https://doi.org/10.1063/1.3076742
165. C. Fábri, E. Mátyus, A.G. Császár, Rotating full- and reduced-dimensional quantum chemical models of molecules. J. Chem. Phys. **134**, 074105 (2011). https://doi.org/10.1063/1.3533950
166. M.L. Diouf, R. Tóbiás, F.M.J. Cozijn, E.J. Salumbides, C. Fábri, C. Puzzarini, A.G. Császár, W. Ubachs, Parity-pair-mixing effects in nonlinear spectroscopy of HDO. Opt. Express **30**, 46040 (2022). https://doi.org/10.1364/OE.474525
167. M. Metsälä, S. Yang, O. Vaittinen, D. Permogorov, L. Halonen, High-resolution cavity ring-down study of acetylene between 12260 and 12380 cm^{-1}. Chem. Phys. Lett **346**, 373 (2001). https://doi.org/10.1016/S0009-2614(01)00945-9
168. S. Twagirayezu, M.J. Cich, T.J. Sears, C.P. McRaven, G.E. Hall, Frequency-comb referenced spectroscopy of ν_4- and ν_5-excited hot bands in the 1.5 μm spectrum of C_2H_2. J. Mol. Spectrosc. **316**, 64 (2015). https://doi.org/10.1016/j.jms.2015.06.010

169. S. Twagirayezu, G.E. Hall, T.J. Sears, Frequency measurements and self-broadening of sub-Doppler transitions in the $\nu_1 + \nu_3$ band of C_2H_2. J. Chem. Phys. **149**, 154308 (2018). https://doi.org/10.1063/1.5047410
170. T.P. Hua, Y.R. Sun, J. Wang, A.W. Liu, S.M. Hu, Frequency metrology of molecules in the near-infrared by NICE-OHMS. Opt. Express **27**, 6106 (2019). https://doi.org/10.1364/OE.27.006106
171. E. Fasci, S. Gravina, G. Porzio, A. Castrillo, L. Gianfrani, Lamb-dip cavity ring-down spectroscopy of acetylene at 1.4 μm. New J. Phys. **23**, 123023 (2021). https://doi.org/10.1088/1367-2630/ac3b6e
172. A. Castrillo, E. Fasci, T. Furtenbacher, V. D'Agostino, M.A. Khan, S. Gravina, L. Gianfrani, A.G. Császár, On the $^{12}C_2H_2$ near-infrared spectrum: absolute transition frequencies and an improved spectroscopic network at the kHz accuracy level. Phys. Chem. Chem. Phys. **25**, 23614 (2023). https://doi.org/10.1039/D3CP01835K
173. A.A. Madej, A.J. Alcock, A. Czajkowski, J.E. Bernard, S. Chepurov, Accurate absolute reference frequencies from 1511 to 1545 nm of the ν_1+ν_3 band of $^{12}C_2H_2$ determined with laser frequency comb interval measurements. J. Opt. Soc. Am. B **23**, 2200 (2006). https://doi.org/10.1364/JOSAB.23.002200
174. A. Castrillo, E. Fasci, H. Dinesan, S. Gravina, L. Moretti, L. Gianfrani, Optical determination of thermodynamic temperatures from a C_2H_2 line-doublet in the near infrared. Phys. Rev. Appl. **11**, 064060 (2019). https://doi.org/10.1103/PhysRevApplied.11.064060
175. S. Wagner, M. Klein, T. Kathrotia, U. Riedel, T. Kissel, A. Dreizler, V. Ebert, In situ TDLAS measurement of absolute acetylene concentration profiles in a non-premixed laminar counter-flow flame. Appl. Phys. B **107**, 585 (2012). https://doi.org/10.1007/s00340-012-4953-5
176. M. Metsälä, F.M. Schmidt, M. Skyttä, O. Vaittinen, L. Halonen, Acetylene in breath: background levels and real-time elimination kinetics after smoking. J. Breath Res. **4**, 046003 (2010). https://doi.org/10.1088/1752-7155/4/4/046003
177. P.B. Rimmer, M. Ferus, I.P. Waldmann, A. Knížek, D. Kalvaitis, O. Ivanek, P. Kubelík, S.N. Yurchenko, T. Burian, J. Dostál, L. Juha, R. Dudžák, M. Krůs, J. Tennyson, S. Civiš, A.T. Archibald, A. Granville-Willett, Identifiable acetylene features predicted for young earth-like exoplanets with reducing atmospheres undergoing heavy bombardment. Astrophys. J. **888**, 21 (2019). https://doi.org/10.3847/1538-4357/ab55e8
178. D. Gasman, M. Min, K.L. Chubb, Investigating the detectability of hydrocarbons in exoplanet atmospheres with JWST. Astron. Astrophys. **659**, A114 (2022). https://doi.org/10.1051/0004-6361/202141468
179. K.L. Chubb, M. Joseph, J. Franklin, N. Choudhury, T. Furtenbacher, A.G. Császár, G. Gaspard, P. Oguoko, A. Kelly, S.N. Yurchenko, J. Tennyson, C. Sousa-Silva, MARVEL analysis of the measured high-resolution rovibrational spectra of C_2H_2. J. Quant. Spectrosc. Radiat. Transf. **204**, 42 (2018). https://doi.org/10.1016/j.jqsrt.2017.08.018
180. T. Furtenbacher, A.G. Császár, J. Tennyson, MARVEL: measured active rotational-vibrational energy levels. J. Mol. Spectrosc. **245**, 115 (2007). https://doi.org/10.1016/j.jms.2007.07.005
181. L.-G. Tao, A.-W. Liu, K. Pachucki, J. Komasa, Y.R. Sun, J. Wang, S.-M. Hu, Toward a determination of the proton-electron mass ratio from the lamb-dip measurement of HD. Phys. Rev. Lett. **120**, 153001 (2018). https://doi.org/10.1103/PhysRevLett.120.153001
182. R. Aiello, V.D. Sarno, M.G.D. Santi, M.D. Rosa, I. Ricciardi, P.D. Natale, L. Santamaria, G. Giusfredi, P. Maddaloni, Absolute frequency metrology of buffer-gas-cooled molecular spectra at 1 kHz accuracy level. Nat. Commun. **13**, 7016 (2022). https://doi.org/10.1038/s41467-022-34758-9
183. O.L. Polyansky, K. Bielska, M. Ghysels, L. Lodi, N.F. Zobov, J.T. Hodges, J. Tennyson, High-accuracy CO_2 line intensities determined from theory and experiment. Phys. Rev. Lett. **114**, 243001 (2015). https://doi.org/10.1103/PhysRevLett.114.243001
184. T.A. Odintsova, E. Fasci, L. Moretti, E.J. Zak, O.L. Polyansky, J. Tennyson, L. Gianfrani, A. Castrillo, Highly accurate intensity factors of pure CO_2 lines near 2 μm. J. Chem. Phys. **146**, 244309 (2017). https://doi.org/10.1063/1.4989925
185. D.A. Long, Z.D. Reed, A.J. Fleisher, J. Mendonca, S. Roche, J.T. Hodges, High-accuracy near-infrared carbon dioxide intensity measurements to support remote sensing. Geophys. Res. Lett. **47**, e2019GL086344 (2020). https://doi.org/10.1029/2019GL086344
186. I. Galli, S. Bartalini, S. Borri, P. Cancio, D. Mazzotti, P. De Natale, G. Giusfredi, Molecular gas sensing below parts per trillion: radiocarbon-dioxide optical detection. Phys. Rev. Lett. **107**, 270802 (2011). https://doi.org/10.1103/PhysRevLett.107.270802

187. I. Galli, S. Bartalini, S. Borri, P. Cancio, G. Giusfredi, D. Mazzotti, P.D. Natale, Ti:sapphire laser intracavity difference-frequency generation of 30 mw cw radiation around 4.5μm. Opt. Lett. **35**, 3616 (2010). https://doi.org/10.1364/OL.35.003616
188. G. Giusfredi, I. Galli, D. Mazzotti, P. Cancio, P. De Natale, Theory of saturated-absorption cavity ring-down: radiocarbon dioxide detection, a case study. J. Opt. Soc. Am. B **32**, 2223 (2015). https://doi.org/10.1364/JOSAB.32.002223
189. A.J. Fleisher, D.A. Long, Q. Liu, L. Gameson, J.T. Hodges, Optical measurement of radiocarbon below unity fraction modern by linear absorption spectroscopy. J. Phys. Chem. Lett. **8**, 4550 (2017). https://doi.org/10.1021/acs.jpclett.7b02105
190. V. Sonnenschein, R. Terabayashi, H. Tomita, S. Kato, N. Hayashi, S. Takeda, L. Jin, M. Yamanaka, N. Nishizawa, A. Sato, K. Yoshida, T. Iguchi, A cavity ring-down spectrometer for study of biomedical radiocarbon-labeled samples. J. Appl. Phys. **124**, 033101 (2018). https://doi.org/10.1063/1.5041015
191. G. Genoud, J. Lehmuskoski, S. Bell, V. Palonen, M. Oinonen, M.-L. Koskinen-Soivi, M. Reinikainen, Laser spectroscopy for monitoring of radiocarbon in atmospheric samples. Anal. Chem. **91**, 12315 (2019). https://doi.org/10.1021/acs.analchem.9b02496
192. M.G.D. Santi, G. Insero, S. Bartalini, P. Cancio, F. Carcione, I. Galli, G. Giusfredi, D. Mazzotti, A. Bulgheroni, A.I.M. Ferri, R. Alvarez-Sarandes, L.A. de Las Heras, V. Rondinella, P. De Natale, Precise radiocarbon determination in radioactive waste by a laser-based spectroscopic technique. PNAS **119**, e2122122119 (2022). https://doi.org/10.1073/pnas.2122122119
193. P. Cancio Pastor, I. Galli, G. Giusfredi, D. Mazzotti, P. De Natale, Testing the validity of Bose–Einstein statistics in molecules. Phys. Rev. A **92**, 063820 (2015). https://doi.org/10.1103/PhysRevA.92.063820
194. D. Mazzotti, P. Cancio, G. Giusfredi, M. Inguscio, P. De Natale, Search for exchange-antisymmetric states for spin-0 particles at the 10^{-11} level. Phys. Rev. Lett. **86**, 1919 (2001). https://doi.org/10.1103/PhysRevLett.86.1919
195. H. Naus, A. de Lange, W. Ubachs, $b^1\Sigma_g^+ - X^3\Sigma_g^-$ (0,0) band of oxygen isotopomers in relation to tests of the symmetrization postulate in $^{16}O_2$. Phys. Rev. A **56**, 4755 (1997). https://doi.org/10.1103/PhysRevA.56.4755
196. W. Heitler, F. London, Wechselwirkung neutraler atome und homöopolare bindung nach der quantenmechanik. Z. Angew. Phys. **44**, 455 (1927). https://doi.org/10.1007/BF01397394
197. K. Pachucki, J. Komasa, Leading order nonadiabatic corrections to rovibrational levels of H_2, D_2, and T_2. J. Chem. Phys. **143**, 034111 (2015). https://doi.org/10.1063/1.4927079
198. K. Pachucki, J. Komasa, Nonadiabatic rotational states of the hydrogen molecule. Phys. Chem. Chem. Phys. **20**, 247 (2018). https://doi.org/10.1039/C7CP06516G
199. M. Puchalski, J. Komasa, P. Czachorowski, K. Pachucki, Nonadiabatic QED correction to the dissociation energy of the hydrogen molecule. Phys. Rev. Lett. **122**, 103003 (2019). https://doi.org/10.1103/PhysRevLett.122.103003
200. K. Pachucki, J. Komasa, Nonrelativistic energy levels of D_2. Phys. Chem. Chem. Phys. **21**, 10272 (2019). https://doi.org/10.1039/C9CP01308C
201. M. Puchalski, A. Spyszkiewicz, J. Komasa, K. Pachucki, Nonadiabatic relativistic correction to the dissociation energy of H_2, D_2, and HD. Phys. Rev. Lett. **121**, 073001 (2018). https://doi.org/10.1103/PhysRevLett.121.073001
202. M. Puchalski, J. Komasa, A. Spyszkiewicz, K. Pachucki, Dissociation energy of molecular hydrogen isotopologues. Phys. Rev. A **100**, 020503 (2019). https://doi.org/10.1103/PhysRevA.100.020503
203. K. Piszczatowski, G. Łach, M. Przybytek, J. Komasa, K. Pachucki, B. Jeziorski, Theoretical determination of the dissociation energy of molecular hydrogen. J. Chem. Theory Comput. **5**, 3039 (2009). https://doi.org/10.1021/ct900391p
204. K. Pachucki, Born–Oppenheimer potential for H_2. Phys. Rev. A **82**, 032509 (2010). https://doi.org/10.1103/PhysRevA.82.032509
205. M. Siłkowski, M. Zientkiewicz, K. Pachucki, Accurate Born–Oppenheimer potentials for excited Σ^+ states of the hydrogen molecule. Adv. Quant. Chem. **83**, 255 (2021). https://doi.org/10.1016/bs.aiq.2021.05.012
206. M. Siłkowski, K. Pachucki, Born-Oppenheimer potentials for Π, Δ, and Φ states of the hydrogen molecule. Mol. Phys. **120**, e2062471 (2022). https://doi.org/10.1080/00268976.2022.2062471
207. K. Pachucki, J. Komasa, Schrödinger equation solved for the hydrogen molecule with unprecedented accuracy. J. Chem. Phys **144**, 164306 (2016). http://scitation.aip.org/content/aip/journal/jcp/144/16/10.1063/1.4948309

208. M. Puchalski, J. Komasa, P. Czachorowski, K. Pachucki, Complete $\alpha^6 m$ corrections to the ground state of H_2. Phys. Rev. Lett. **117**, 263002 (2016). https://doi.org/10.1103/PhysRevLett.117.263002
209. N. Hölsch, M. Beyer, E.J. Salumbides, K.S.E. Eikema, W. Ubachs, Ch. Jungen, F. Merkt, Benchmarking theory with an improved measurement of the ionization and dissociation energies of H_2. Phys. Rev. Lett. **122**, 103002 (2019). https://doi.org/10.1103/PhysRevLett.122.103002
210. J. Hussels, N. Hölsch, C.-F. Cheng, E.J. Salumbides, H.L. Bethlem, K.S.E. Eikema, Ch. Jungen, M. Beyer, F. Merkt, W. Ubachs, Improved ionization and dissociation energies of the deuterium molecule. Phys. Rev. A **105**, 022820 (2022). https://doi.org/10.1103/PhysRevA.105.022820
211. N. Hölsch, I. Doran, F. Merkt, J. Hussels, C.-F. Cheng, E.J. Salumbides, H.L. Bethlem, K.S.E. Eikema, M. Beyer, W. Ubachs, C. Jungen, Ionization and dissociation energies of HD and dipole-induced g/u-symmetry breaking. Phys. Rev. A **108**, 022811 (2023). https://doi.org/10.1103/PhysRevA.108.022811
212. H2SPECTRE version 7.4 Fortran source code. University of Warsaw, Poland (2022). https://www.qcg.home.amu.edu.pl/qcg/public_html/H2Spectre.html
213. M. Puchalski, J. Komasa, K. Pachucki, Relativistic corrections for the ground electronic state of molecular hydrogen. Phys. Rev. A **95**, 052506 (2017). https://doi.org/10.1103/PhysRevA.95.052506
214. W. Ubachs, J.C.J. Koelemeij, K.S.E. Eikema, E.J. Salumbides, Physics beyond the Standard Model from hydrogen spectroscopy. J. Mol. Spectrosc. **320**, 1 (2016). https://doi.org/10.1016/j.jms.2015.12.003
215. E.J. Salumbides, J.C.J. Koelemeij, J. Komasa, K. Pachucki, K.S.E. Eikema, W. Ubachs, Bounds on fifth forces from precision measurements on molecules. Phys. Rev. D **87**, 112008 (2013). https://doi.org/10.1103/PhysRevD.87.112008
216. G. Herzberg, Quadrupole rotation-vibration spectrum of the hydrogen molecule. Nature **163**, 170 (1949). https://www.nature.com/articles/163170a0
217. S.L. Bragg, W.H. Smith, J.W. Brault, Line positions and strengths in the H_2 quadrupole spectrum. Astrophys. J **263**, 999 (1982). https://ui.adsabs.harvard.edu/abs/1982ApJ...263..999B
218. D.E. Jennings, J.W. Brault, The ground state of molecular hydrogen. J. Mol. Spectrosc. **102**, 265 (1983). https://doi.org/10.1016/0022-2852(83)90039-5
219. D.W. Ferguson, K.N. Rao, M.E. Mickelson, L.E. Larson, An experimental-study of the 4-0 and 5-0 quadrupole vibration-rotation bands of H_2 in the visible. J. Mol. Spectrosc. **160**, 315 (1993). https://doi.org/10.1006/jmsp.1993.1178
220. A. Campargue, S. Kassi, K. Pachucki, J. Komasa, The absorption spectrum of H_2: CRDS measurements of the (2–0) band, review of the literature data and accurate ab initio line list up to 35 000 cm^{-1}. Phys. Chem. Chem. Phys. **14**, 802 (2012). https://doi.org/10.1039/C1CP22912E
221. S. Kassi, A. Campargue, K. Pachucki, J. Komasa, The absorption spectrum of D_2: Ultrasensitive cavity ring down spectroscopy of the (2-0) band near 1.7 μm and accurate ab initio line list up to 24000 cm^{-1}. J. Chem. Phys. **136**, 184309 (2012). http://scitation.aip.org/content/aip/journal/jcp/136/18/10.1063/1.4707708
222. S. Vasilchenko, D. Mondelain, S. Kassi, P. Cermák, B. Chomet, A. Garnache, S. Denet, V. Lecocq, and A. Campargue, The HD spectrum near 2.3 μm by CRDS-VECSEL: electric quadrupole transition and collision-induced absorption. J. Mol. Spectrosc. **326**, 9 (2016). https://doi.org/10.1016/j.jms.2016.04.002
223. D.C. Robie, J.T. Hodges, Line positions and line strengths for the 3 ← 0 electric quadrupole band of $H_2\ ^1\Sigma_g^+$. J. Chem. Phys. **124**, 024307 (2006). https://doi.org/10.1063/1.2145925
224. C.-F. Cheng, Y.R. Sun, H. Pan, J. Wang, A.-W. Liu, A. Campargue, S.-M. Hu, Electric-quadrupole transition of H_2 determined to 10^{-9} precision. Phys. Rev. A **85**, 024501 (2012). https://doi.org/10.1103/PhysRevA.85.024501
225. Y. Tan, J. Wang, C.-F. Cheng, X.-Q. Zhao, A.-W. Liu, S.-M. Hu, Cavity ring-down spectroscopy of the electric quadrupole transitions of H_2 in the 784–852 nm region. J. Mol. Spectrosc. **300**, 60 (2014). https://doi.org/10.1016/j.jms.2014.03.010
226. A.R.W. McKellar, T. Oka, Study of electric quadrupole fundamental band of D_2 using an infrared difference frequency laser system. Can. J. Phys. **56**, 1315 (1978). https://doi.org/10.1139/p78-172
227. P. Maddaloni, P. Malara, E. De Tommasi, M. De Rosa, I. Ricciardi, G. Gagliardi, F. Tamassia, G. Di Lonardo, P. De Natale, Absolute measurement of the S(0) and S(1) lines in the electric quadrupole fundamental band of D_2 around 3 μm. J. Chem. Phys. **133**, 154317 (2010). https://doi.org/10.1063/1.3493393

228. D. Mondelain, S. Kassi, T. Sala, D. Romanini, D. Gatti, A. Campargue, Sub-MHz accuracy measurement of the S(2) 2–0 transition frequency of D_2 by comb-assisted cavity ring down spectroscopy. J. Mol. Spectrosc. **326**, 5 (2016). https://doi.org/10.1016/j.jms.2016.02.008
229. P. Wcisło, F. Thibault, M. Zaborowski, S. Wojtewicz, A. Cygan, G. Kowzan, P. Maslowski, J. Komasa, M. Puchalski, K. Pachucki, R. Ciuryło, D. Lisak, Accurate deuterium spectroscopy for fundamental studies. J. Quant. Spectrosc. Radiat. Transf. **213**, 41 (2018). https://doi.org/10.1016/j.jqsrt.2018.04.011
230. D. Mondelain, S. Kassi, A. Campargue, Transition frequencies in the (2–0) band of D_2 with MHz accuracy. J. Quant. Spectrosc. Radiat. Transf. **253**, 107020 (2020). https://doi.org/10.1016/j.jqsrt.2020.107020
231. A. de Lange, E. Reinhold, W. Ubachs, Phenomena of g-u symmetry-breakdown in HD. Int. Rev. Phys. Chem. **21**, 257 (2002). https://doi.org/10.1080/01442350210124515
232. G. Herzberg, Rotation-vibration spectrum of the HD molecule. Nature **166**, 563 (1950). https://www.nature.com/articles/166563a0
233. R.A. Durie, G. Herzberg, Forbidden transitions in diatomic molecules: V. The rotation-vibration spectrum of the hydrogen-deuteride (HD) molecule. Can. J. Phys. **38**, 806 (1960). https://doi.org/10.1139/p60-086
234. A.R.W. McKellar, Intensities of dipole and quadrupole rotation-vibration spectra of HD. Can. J. Phys. **52**, 1144 (1974). https://doi.org/10.1139/p74-152
235. A.R.W. McKellar, W. Goetz, D.A. Ramsay, Rotation-vibration spectrum of HD - wavelength and intensity measurements of 3-0, 4-0, 5-0, and 6-0 electric-dipole bands. Astrophys. J. **207**, 663 (1976). https://adsabs.harvard.edu/full/1976ApJ...207..663M
236. B.J. Drouin, S. Yu, J.C. Pearson, H. Gupta, Terahertz spectroscopy for space applications: 2.5–2.7 THz spectra of HD, H_2O and NH_3. J. Mol. Struct. **1006**, 2 (2011). https://doi.org/10.1016/j.molstruc.2011.05.062
237. S. Kassi, A. Campargue, Electric quadrupole and dipole transitions of the first overtone band of HD by CRDS between 1.45 and 1.33 μm. J. Mol. Spectrosc. **267**, 36 (2011). https://doi.org/10.1016/j.jms.2011.02.001
238. A. Castrillo, E. Fasci, L. Gianfrani, Doppler-limited precision spectroscopy of HD at 1.4 μm: an improved determination of the R(1) center frequency. Phys. Rev. A **103**, 22828 (2021). https://doi.org/10.1103/PhysRevA.103.022828
239. S. Kassi, C. Lauzin, J. Chaillot, A. Campargue, The (2–0) R(0) and R(1) transition frequencies of HD determined to a 10^{-10} relative accuracy by Doppler spectroscopy at 80 K. Phys. Chem. Chem. Phys. **24**, 23164 (2022). https://doi.org/10.1039/D2CP02151J
240. T.M. Trivikram, M. Schlösser, W. Ubachs, E.J. Salumbides, Relativistic and QED effects in the fundamental vibration of T_2. Phys. Rev. Lett. **120**, 163002 (2018). https://doi.org/10.1103/PhysRevLett.120.163002
241. K.-F. Lai, P. Czachorowski, M. Schlösser, M. Puchalski, J. Komasa, K. Pachucki, W. Ubachs, E.J. Salumbides, Precision tests of nonadiabatic perturbation theory with measurements on the DT molecule. Phys. Rev. Res. **1**, 033124 (2019). https://doi.org/10.1103/PhysRevResearch.1.033124
242. K.-F. Lai, V. Hermann, T.M. Trivikram, M. Diouf, M. Schlösser, W. Ubachs, E.J. Salumbides, Precision measurement of the fundamental vibrational frequencies of tritium-bearing hydrogen molecules: T_2, DT, HT. Phys. Chem. Chem. Phys. **22**, 8973 (2020). https://doi.org/10.1039/D0CP00596G
243. Q.-H. Liu, Y.-N. Lv, C.-L. Zou, C.-F. Cheng, S.-M. Hu, Saturated absorption spectroscopy of HD at 76 K. Phys. Rev. A **106**, 062805 (2022). https://doi.org/10.1103/PhysRevA.106.062805
244. P. Wcisło, I.E. Gordon, C.-F. Cheng, S.-M. Hu, R. Ciuryło, Collision-induced line-shape effects limiting the accuracy in Doppler-limited spectroscopy of H_2. Phys. Rev. A **93**, 022501 (2016). https://doi.org/10.1103/PhysRevA.93.022501
245. M. Konefał, M. Słowiński, M. Zaborowski, R. Ciuryło, D. Lisak, P. Wcisło, Analytical-function correction to the Hartmann-Tran profile for more reliable representation of the Dicke-narrowed molecular spectra. J. Quant. Spectrosc. Radiat. Transf. **242**, 106784 (2020). https://doi.org/10.1016/j.jqsrt.2019.106784
246. N. Ngo, D. Lisak, H. Tran, J.-M. Hartmann, An isolated line-shape model to go beyond the Voigt profile in spectroscopic databases and radiative transfer codes. J. Quant. Spectrosc. Radiat. Transf. **129**, 89 (2013). https://doi.org/10.1016/j.jqsrt.2013.05.034
247. J. Komasa, M. Puchalski, K. Pachucki, Hyperfine structure in the HD molecule. Phys. Rev. A **102**, 012814 (2020). https://doi.org/10.1103/PhysRevA.102.012814

248. P. Wcisło, I.E. Gordon, H. Tran, Y. Tan, S.-M. Hu, A. Campargue, S. Kassi, D. Romanini, C. Hill, R.V. Kochanov, L.S. Rothman, The implementation of non-Voigt line profiles in the HITRAN database: H_2 case study. J. Quant. Spectrosc. Radiat. Transf. **177**, 75 (2016). https://doi.org/10.1016/j.jqsrt.2016.01.024
249. M. Słowiński, F. Thibault, Y. Tan, J. Wang, A.-W. Liu, S.-M. Hu, S. Kassi, A. Campargue, M. Konefał, H. Jóźwiak, K. Patkowski, P. Żuchowski, R. Ciuryło, D. Lisak, P. Wcisło, H_2-He collisions: ab initio theory meets cavity-enhanced spectra. Phys. Rev. A **101**, 052705 (2020). https://doi.org/10.1103/PhysRevA.101.052705
250. P. Wcisło, F. Thibault, N. Stolarczyk, H. Jóźwiak, M. Słowiński, M. Gancewski, K. Stankiewicz, M. Konefał, S. Kassi, A. Campargue, Y. Tan, J. Wang, K. Patkowski, R. Ciuryło, D. Lisak, R. Kochanov, L. Rothman, I. Gordon, The first comprehensive dataset of beyond-Voigt line-shape parameters from ab initio quantum scattering calculations for the HITRAN database: He-perturbed H_2 case study. J. Quant. Spectrosc. Radiat. Transf. **260**, 107477 (2021). https://doi.org/10.1016/j.jqsrt.2020.107477
251. M. Słowiński, H. Jóźwiak, M. Gancewski, K. Stankiewicz, N. Stolarczyk, Y. Tan, J. Wang, A.-W. Liu, S.-M. Hu, S. Kassi, A. Campargue, K. Patkowski, P.S. Żuchowski, R. Ciuryło, F. Thibault, P. Wcisło, Collisional line-shape effects in accurate He-perturbed H_2 spectra. J. Quant. Spectrosc. Radiat. Transf. **277**, 107951 (2022). https://doi.org/10.1016/j.jqsrt.2021.107951
252. P. Wcisło, H. Tran, S. Kassi, A. Campargue, F. Thibault, R. Ciuryło, Velocity-changing collisions in pure H_2 and H_2-Ar mixture. J. Chem. Phys **141**, 074301 (2014). https://doi.org/10.1063/1.4892414
253. N. Stolarczyk, G. Kowzan, F. Thibault, H. Cybulski, M. Słowiński, Y. Tan, J. Wang, A.-W. Liu, S.-M. Hu, P. Wcisło, High-precision cavity-enhanced spectroscopy for studying the H_2 -Ar collisions and interactions. J. Chem. Phys **158**, 094303 (2023). https://pubs.aip.org/aip/jcp/article/2881292
254. K. Pachucki, J. Komasa, Nonadiabatic corrections to rovibrational levels of H_2. J. Chem. Phys. **130**, 164113 (2009). https://doi.org/10.1063/1.3114680
255. M.L. Diouf, F.M.J. Cozijn, B. Darquié, E.J. Salumbides, W. Ubachs, Lamb-dips and Lamb-peaks in the saturation spectrum of HD. Opt. Lett. **44**, 4733 (2019). https://doi.org/10.1364/OL.44.004733
256. T.-P. Hua, Y.R. Sun, J. Wang, C.-L. Hu, L.-G. Tao, A.-W. Liu, S.-M. Hu, Cavity-enhanced saturation spectroscopy of molecules with sub-kHz accuracy. Chin. J. Chem. Phys. **32**, 107 (2019). https://doi.org/10.1063/1674-0068/cjcp1812272
257. Y.-N. Lv, A.-W. Liu, Y. Tan, C.-L. Hu, T.-P. Hua, X.-B. Zou, Y.R. Sun, C.-L. Zou, G.-C. Guo, S.-M. Hu, Fano-like resonance due to interference with distant transitions. Phys. Rev. Lett. **129**, 163201 (2022). https://doi.org/10.1103/PhysRevLett.129.163201
258. P. Dupré, Hyperfine transitions in the first overtone mode of hydrogen deuteride. Phys. Rev. A **101**, 022504 (2020). https://doi.org/10.1103/PhysRevA.101.022504
259. M. Puchalski, J. Komasa, K. Pachucki, Hyperfine structure of the first rotational level inH_2, D_2 and HD molecules and the deuteron quadrupole moment. Phys. Rev. Lett. **125**, 253001 (2020). https://doi.org/10.1103/PhysRevLett.125.253001
260. H. Jóźwiak, H. Cybulski, P. Wcisło, Positions and intensities of hyperfine components of all rovibrational dipole lines in the HD molecule. J. Quant. Spectrosc. Radiat. Transf. **253**, 107171 (2020). https://doi.org/10.1016/j.jqsrt.2020.107171
261. F.M.J. Cozijn, M.L. Diouf, V. Hermann, E.J. Salumbides, M. Schlösser, W. Ubachs, Rotational level spacings in HD from vibrational saturation spectroscopy. Phys. Rev. A **105**, 062823 (2022). https://doi.org/10.1103/PhysRevA.105.062823
262. F.M.J. Cozijn, M.L. Diouf, W. Ubachs, Saturation spectroscopy of R(0), R(2) and P(2) lines in the (2–0) band of HD. Eur. J. Phys. D **76**, 220 (2022). https://doi.org/10.1140/epjd/s10053-022-00552-x
263. U. Fano, Effects of configuration interaction on intensities and phase shifts. Phys. Rev. **124**, 1866 (1961). https://doi.org/10.1103/PhysRev.124.1866
264. F.M.J. Cozijn, M.L. Diouf, W. Ubachs, Lamb dip of a quadrupole transition in H_2. Phys. Rev. Lett. **131**, 073001 (2023). https://doi.org/10.1103/PhysRevLett.131.073001
265. F.M.J. Cozijn, M.L. Diouf, W. Ubachs, Precision measurement of vibrational quanta in tritium hydride. Phys. Rev. Lett. **132**, 113002 (2024). https://doi.org/10.1103/PhysRevLett.132.113002
266. H. Jóźwiak, H. Cybulski, P. Wcisło, Hyperfine components of rovibrational dipole transitions in HT and DT. J. Quant. Spectrosc. Radiat. Transf. **270**, 107662 (2021). https://doi.org/10.1016/j.jqsrt.2021.107662
267. J.L. Hall, C.J. Bordé, K. Uehara, Direct optical resolution of the recoil effect using saturated absorption spectroscopy. Phys. Rev. Lett. **37**, 1339 (1976). https://doi.org/10.1103/PhysRevLett.37.1339

268. M. Lamperti, L. Rutkowski, D. Ronchetti, D. Gatti, R. Gotti, G. Cerullo, F. Thibault, H. Jóźwiak, S. Wójtewicz, P. Masłowski, P. Wcislo, D. Polli, M. Marangoni, Stimulated Raman scattering metrology of molecular hydrogen. Commun. Phys. **6**, 67 (2023). https://doi.org/10.1038/s42005-023-01187-z
269. A. Fast, S.A. Meek, Sub-ppb measurement of a fundamental band rovibrational transition in HD. Phys. Rev. Lett. **125**, 023001 (2020). https://doi.org/10.1103/PhysRevLett.125.023001
270. A. Fast, S.A. Meek, Precise measurement of the D_2 $S_1(0)$ vibrational transition frequency. Mol. Phys. **120**, e1999520 (2022). https://doi.org/10.1080/00268976.2021.1999520
271. H. Fleurbaey, A.O. Koroleva, S. Kassi, A. Campargue, The high-accuracy spectroscopy of H_2 rovibrational transitions in the (2-0) band near 1.2 μm. Phys. Chem. Chem. Phys. **25**, 14749 (2023). https://doi.org/10.1039/D3CP01136D
272. A. Castrillo, E. Fasci, L. Gianfrani, Erratum: Doppler-limited precision spectroscopy of HD at 1.4 μm: An improved determination of the R(1) center frequency [Phys. Rev. A 103, 022828 (2021)]. Phys. Rev. A **103**, 069902 (2021). https://doi.org/10.1103/PhysRevA.103.069902
273. M. Siłkowski, K. Pachucki, J. Komasa, M. Puchalski, Leading-order QED effects in the ground electronic state of molecular hydrogen. Phys. Rev. A **107**, 032807 (2023). https://doi.org/10.1103/PhysRevA.107.032807
274. R. Aiello, V.D. Sarno, M.G.D. Santi, M.D. Rosa, I. Ricciardi, G. Giusfredi, P.D. Natale, L. Santamaria, P. Maddaloni, Lamb-dip saturated-absorption cavity ring-down rovibrational molecular spectroscopy in the near-infrared. Photon. Res. **10**, 1803 (2022). https://doi.org/10.1364/PRJ.456515
275. H. Jóźwiak, P. Wcisło, Magic wavelength for a rovibrational transition in molecular hydrogen. Sci. Rep. **12**, 14529 (2022). https://doi.org/10.1038/s41598-022-18159-y
276. R. Tóbiás, M.L. Diouf, F.M.J. Cozijn, W. Ubachs, A.G. Császár, All paths lead to hubs in the spectroscopic networks of water isotopologues $H_2{}^{16}O$ and $H_2{}^{18}O$. Commun. Chem. **7**, 34 (2024). https://doi.org/10.1038/s42004-024-01103-8